Quantum dynamics of H + LiH/LiH^+ collisions at thermal and ultracold conditions

A Thesis

Submitted for the Degree of

Doctor of Philosophy

By

Tanmoy Kumar Roy

SCHOOL OF CHEMISTRY

UNIVERSITY OF HYDERABAD

HYDERABAD 500 046

INDIA

February **2015**

Dedicated

To
My Parents

STATEMENT

I hereby declare that the matter embodied in this thesis is the result of investigations carried out by me in the School of Chemistry, University of Hyderabad, Hyderabad, under the supervision of **Prof. Susanta Mahapatra**.

In keeping with the general practice of reporting scientific observations, due acknowledgment has been made wherever the work described is based on the findings of other investigators.

January 2015 (**Tanmoy Kumar Roy**)

Hyderabad - 500 046

School Of Chemistry
University Of Hyderabad
Hyderabad 500 046
India

CERTIFICATE

Certified that the work contained in this thesis entitled "Quantum dynamics of H + LiH/LiH^+ collisions at thermal and ultracold conditions " has been carried out by Mr. **Tanmoy Kumar Roy** under my supervision and the same has not been submitted elsewhere for a degree.

(**Prof. Susanta Mahapatra**)
Thesis Supervisor

Dean
School of Chemistry
University of Hyderabad
Hyderabad 500 046
India.

Acknowledgement

Throughout the vogue of my Ph.D, which spans over six and half years, I came in contact with some people without whose help it could be near to impossible for me to carry out my research work. I do thank to all these people who assisted me in various time in various form.

At the first place it is noteworthy to thank my Ph.D supervisor Prof. Susanta Mahapatra who not only supervise my research work but fuelled the motivation and encouragement. His way of analysing a scientific problem and the art of scientific writing influenced me and I learned a lot from him. I do believe that the experience I got through his suggestions, comments and criticisms will help me in near future to understand a dynamical problem.

I do extend my thanks to Prof. M. Durga Prasad for his excellent teachings and some fruitful discussions on quantum mechanics and mathematical problems.

I am thankful to all my present and former lab-mates with whom I had the opportunity to work, discuss and do some gossip. The sweet memories I do have with my lab-mates are really hard to forget. I am highly benefited from the scientific knowledge and programing skill of Dr. T. Rajagopala Rao who virtually taught me and helped me to understand the dynamical problems in my early days. I am fortunate to have him as a co-author in one paper. I thank to Dr. S. Rajagopala Reddy and Mr. Nagaprasad Reddy for the fruitful and collective discussions. Going beyond the academics, the memory of the travel to Kanpur to attain the theoretically chemistry symposium in December 2010 with TRR and SRR is still fresh in my mind. Specially when I recall the event of chasing the train after missing it at Secunderabad and eventually being able

to catch it at Warangal after travelling a distance of about 150 km by car, I become nostalgic. The strongman and the enthusiastic Rudraditya, diplomatic Sugata and the curious baby Arpita do deserve acknowledgement. The bonding with these people is not only concentrated within academics but goes beyond to personal levels. I do thank to my other colleague viz. Dr. Sivaranjan Reddy, Dr. T. Mandal, Dr. S. Ghanta, Krishna, Arun, Subbu and Suranjan for maintaining a cheerful atmosphere. I am also grateful to Dr. B. Saritha, Sridhar and Dinesh for their assistances on various occasions.

I am thankful to Dr. S. Ghoshal and P. Honvoult for helping me to understand the 'ABC reactive scattering program'. Today, I don't want to miss the opportunity to thank present and former Dean, School of chemistry and Mr. Durgesh Singfor the assistances in official work.

At this point of time, being at the verge of my Ph.d carrier, 'when on my couch I lie in vacant or in pensive mood' the story of the passed days 'flash upon in my inward eyes' and the canvas of the life becomes live. I do realize that the people with whom I came across had influenced me a lot. I do have a coherent understanding with my former roommate Monojit (Mona). 'I cannot remember to forget' the way Mona took care of me when I got injured in my leg. It would also be quite unjustified if I dont thank Dr. Tapta K. Roy, Dr. V. Sarkar, Dr. Tulika Ghosh, Dr. S. Banik, Dr. S. Banerjee, Debparna, Maity da, Nayan, Rishi da, Pati da, Anup, Meheboob, Raja, Satya, Olivia, Koushik, Navendu, Suman Ghosh, Suman Dana, Suman Sen, Kollol, Sudipto, Sritoma, Paromita, Dinu da, Raju, Santanu da, Arup, Azahar, Saheli, Shibu, Deepan, Rajiv, Sritam, Kishore and Sasi. At the same time it is my pleasure to thank all of my other collogues at school of chemistry for having a strong (chemical) bonding among us.

I do thank to Mrs. Mahapatra, Popoi and Diya for providing a homely atmosphere and for their delightful company on various occasions.

I am indebted to the **Council of Scientific and Industrial Research (CSIR)** for the doctoral fellowship.

I feel lucky to thank my parents and my brother for their unconditional support and encouragement. And at the end I do thank you for having a look at my thesis.

Tanmoy Kumar Roy

List of Abbreviations

CBR	The origin of cosmic background radiation
CM	Classical Mechanics
QM	Quantum Mechanics
CT	Classical Trajectory
QCT	Quasi-Classical Trajectory
WP	Wave packet
BEC	Bose-Einstein condensates
PES	Potential energy surface
CCSD(T)	Coupled-cluster singles doubles triples
DMJ	Dunne, Murrel, and Jemmer
CI	Configuration interaction
CASSCF	Complete active space self consistent field
MRCI	Multi-reference configuration interaction
cc-pVQZ	Correlation consistent polarized valence quadrupole zeta
CID	Collision induced dissociation
TDQM	Time dependent quantum mechanics
TIQM	Time independent quantum mechanics
CS	Centrifugal sudden
TDWP	Time dependent wave packet
TDSE	Time dependent Schrödinger equation
GWP	Gaussian Wave Packet
SO	Split operator
FFT	Fast Fourier transformation
DVR	Discrete Variable Representation
FBR	Finite basis representation
BF	Body fixed

Contents

Chapter 1

Introduction

According to the standard Big Bang nucleosynthesis framework [1, 2] the LiH molecule and its radical cation are considered among few molecules to play an important role in the chemistry of early universe. It was proposed that the recombination of Li took place just after helium and hydrogen. In this recombination epoch the lithium chemistry started with the radiative association processes leading to the formation of LiH and LiH^+ [3–6].

$$\begin{aligned} Li^+ + e^- &\rightarrow Li + \nu \\ Li^+ + H^- &\rightarrow Li + H \\ Li + H &\rightarrow LiH + \nu \\ Li^+ + H &\rightarrow LiH^+ + \nu \\ Li + H^+ &\rightarrow LiH^+ + \nu \end{aligned} \tag{1.1}$$

These molecules, after formation get destroyed or retained by collision with atomic hydrogen, proton etc. and the resulting products undergo ro-vibrational

relaxations,

$$
\begin{aligned}
&LiH + H \rightarrow Li + H_2 + \nu \\
&LiH + H^+ + \nu \rightarrow Li^+ + H_2 \\
&LiH + H^+ \rightarrow Li + {H_2}^+ + \nu \\
&LiH + H^+ + \nu \rightarrow LiH^+ + H \\
&LiH + \nu \rightarrow Li + H \\
&LiH^+ + H \rightarrow Li^+ + H_2 + \nu \\
&LiH^+ + H + \nu \rightarrow Li^+ + H + H \\
&LiH^+ + H + \nu \rightarrow LiH + H^+ \\
&LiH^+ + H + \nu \rightarrow Li + {H_2}^+,
\end{aligned}
\tag{1.2}
$$

and thus reduces the abundance of LiH and LiH^+ species in the cosmic environment. Large abundance of H atoms in the exotic interstellar medium naturally qualifies it as a most important partner for the three-body H + LiH/LiH^+ collision process. The abundance of LiH^+ in cosmic environment is expected to be relatively more than the neutral species because of the low ionization potential of LiH molecule [5]. The formation and depletion of LiH/LiH^+ species apparently play crucial role in stellar evolution and galactic lithium production. Because of high dipole moment, low excitation threshold and closely spaced rotational and vibrational energy levels, these molecules can radiate excess energy during the gravitational collapse process and because of this property they are considered to be more likely molecules in the formation of condensed structure in early universe. Low excitation threshold and fast radiative decay of LiH/LiH^+ are the additional qualifications favouring their role as coolants as they can absorb en-

ergies, undergo ro-vibrational excitations then emit lower frequency radiation by undergoing rotational/ vibrational relaxation and thus can work as an effective heat pump [7] . The origin of cosmic background radiation (CBR) and anomalous microwave emission along the line of sight of young stars was proposed [8–13] to have contribution from this molecule and its radical cation, LiH^+. But the very low abundance of these species (LiH/LiH^+) in the cosmic environment raised several doubts on the claim of it's importance in the colling process and background radiations [14–18]. Nevertheless, the formation and depletion of LiH/ LiH^+ seems to be among some of the basic chemical reactions in the primordial gas cloud [4]. In order to have a better understanding on Li-chemistry it is important to have a detail knowledge about the collisional dynamics of LiH and LiH^+ with H.

1.1 Molecular Collision: At thermal and ultracold conditions

In molecular reaction dynamics, a single chemical event is treated as a collision in which the reactants change their chemical identity through breakage and formation of atomic connectivity (bonds). In other word, in reaction dynamics, the microscopic details in molecular level during the collisional event are studied and thereby, the reactivity and mechanism of the reaction can be predicted correctly. An insight into an assemble of collisional events give an impression that each of these processes has their own unique mechanism embodied in the relative orientation, angular distribution, relative kinetic energy, rotational and vibrational motion of the reactants and so on [19, 20].

Temperature of the collisional system, in other word the relative kinetic energy of the colliding particle affects the dynamical processes by changing the condition of the collisions. Based on the reaction temperature (relative collision energy) the collisions are classified as ultracold, cold and thermal collisions. If the collisional temperature is more than 1 K then it is considered as thermal collision whereas ultracold collision has temperature less then 10^{-3} K [20].

With the availability of advance technology, the study of molecular dynamics becomes possible both experimentally and theoretically. The major problem in the experimental study is of detecting the collisional outcomes before they get lost through a secondary collision. The bottleneck of making such type of '*isolated conditions*' or '*single-collision conditions*' has been overcome with the development of cross molecular beam experiment and various type of laser pump-probe techniques like femtosecond laser spectroscopy etc. [20]. Theoretically, the molecular reaction dynamics, at thermal conditions, is studied by either classical mechanics (CM) or by quantum mechanics (QM), and also by a combination of these two (quassi classical mechanics). In classical mechanics the Lagrangian and/or Hamiltonian equations are solved for a given initial position and momentum of the reactant. After calculating a large number of trajectories, the total reaction probability is determined by the fractions of trajectories leads to the products [20, 21].

In classical mechanics the energy is continuous, quantization of the energy levels do not arise in this calculations. To get some quantum feature in the classical trajectory (CT) calculations some short of binning are done by sampling the trajectories to a certain rotational and vibrational quantum levels of the reactants and products and is known as 'quasi-classical trajectory' (QCT) calculation. This

QCT calculation is found to be very effective as it drastically reduces the computational cost compared to exact quantum mechanical calculations. But this QCT methods still have some shortcomings e.g. *i.* it can not describe the pure quantum mechanical phenomena like tunneling, *ii.* zero poing energy is also not conserved properly and it can be converted into translational energy. [19, 20]

A quantum mechanical (QM) calculation, on the other hand, gives the best description of the dynamics study. In QM calculations the Schrödinger equation can be solved both in time-dependent as well as time-independent way. Both the methods have some advantages and limitations. In a time-dependent method, the movement of the wavepacket with time can be visualized by recording the wave packet (WP) snapshots and hence the mechanistic details of the dynamics can be understood. But the time-independent methods become more effective for collisional systems which support fairly long-lived resonances. Because in such cases the WP has to propagate for sufficiently long time in time-dependent method and hence it needs a lot of computational overheads. The time-independent methods also works better for the ultracold dynamics where the de Broglie wave length of the reagents are sufficiently large.

In the recent past achievement of creating Bose-Einstein condensates (BECs) [22–24] and Fermi degeneracy [25] by cooling, trapping and manipulating the ensembles of atoms and molecules in some sub Kelvin temperature had opened up the interesting field of study *i.e.* chemistry at cold and ultracold temperature. The molecular dynamics processes take place in such exotic condition of ultracold temperature are someway different with that in thermal conditions. The extremely low collision energy of the interacting particles make the de Broglie wavelength very large and even larger than the molecules themselves. Hence,

in such cases, molecular reaction cannot be considered as the collision of two 'hard spheres' but as an interaction between two waves. In the cold temperature conditions the internal energy of the reactants is primarily responsible for the reactant to product transformation. In such conditions the long-range part of the interaction potential plays the key role in the dynamics. Slow reagent approach and the large de Broglie wavelength of the collision partners makes the quantum effects predominant. In such conditions the external electric/magnetic fields also sometime controls the scattering processes. The external fields may open up new channels or may close some channels compared to field free environment. It is also known that in such conditions the quasi bound states of van der waals potentials, which may not be in the vicinity of transition state may undergo prereaction and change the nature of the dynamical outcomes [26].

Consequently a theoretical study of the ultracold dynamics is not possible by CT or QCT calculations but by quantum mechanical calculations only. A time-dependent wave packet propagation approach that is robust at thermal conditions, in principle can be used but is ill-suited for the description of collision dynamics at ultracold temperature conditions because of technical reasons. As the collision energy becomes vanishingly small in the latter situation, large de Broglie wavelength of the collision partners and the long-range part of the interaction potential becomes crucially important. Understandably, a grid based time-dependent wave packet approach is not a method of choice in such conditions as the wave packet would lack adequate translational kinetic energy to move on the discrete coordinate grid. One needs a very large spatial grid to avoid wave packet reflections and wraparound at the grid boundaries. In addition, the slowly moving wave packet needs to be propagated for a very long time. A time-

independent quantum mechanical treatment on the other hand, has been quite successful in such circumstances and also to capture the dominant quantum effects such as tunnelling. Time-independent quantum mechanical calculations are therefore commonly performed to calculate the dynamical properties at the ultracold temperature conditions. In the present thesis the collisional dynamics at the ultracold conditions is studied by using a time-independent quantum mechanical method and the collisions at thermal conditions are treated in a time-dependent quantum mechanical framework.

1.2 Potential Energy Surface

The very first step for an understanding of the molecular dynamics is to understand the potential energy surfaces(s) (PES(s)) of the colliding system. Basically it describes the potential energy which is an electrostatic interaction between nuclei and electrons involved in the reaction as a function of nuclear coordinate. The one asymptote of the PES describes the reactants and the other asymptote to products. The gradient at any point on the PES describes the force felt by the atom and/or molecule in that point during chemical transformation from reactants to products.

The understanding of PES starts with the famous Born-Oppenheimer approximation [27] by decoupling the electronic motion from the nuclear motion. The nuclei are assumed to be stationary during the electronic movements. The PES, thus generated, if remains well separated from the PESs of other electronic states, is an adiabatic PES. But when two PESs of two different electronic state are close enough (separated in one quantum of nuclear energy) or overlaps at some point, the coupling between electronic and nuclear motion (termed as nonadiabatic cou-

pling) become considerably large and cannot be neglected.

If the electronic state under investigation does not interact with other electronic state then only one adiabatic PES is sufficient to understand the reaction dynamics. But when they interact a nonadiabatic dynamical calculation considering all the PES of the interacting electronic states are mandatory to describe the correct nature of the dynamics.

1.2.1 PES for H + LiH reaction

The LiH_2 is the simplest alkali metal-dihydrogen partner having only five electrons. Among these five electrons two are core electrons. Due to the ostensible astrophysical importance and computational easiness, the dynamics of H with LiH and LiH^+ got an unprecedented attention from various research group [16–18, 28–54]. Several PESs for the electronic ground state of the H + LiH collisional system have been developed by leading experts in this field in the past decades [28–36]. Each of these PESs were calculated with improved electronic structure methods and they differ in terms of crucial stationary points that are important for the mechanistic details of the dynamics. The PES developed by Clarke *et al.* [28] for the collinear H + LiH configurations using the spin-coupled valence bond *ab initio* method predicted the existence of an early barrier of $\sim$ 0.036 eV. Subsequent to this work, two new PESs appeared in the literature in 2001 [29, 30] . The one developed by Bodo *et al.* [29] employing the coupled-cluster singles doubles triples (CCSD(T)) method, to study nonreactive dynamics, predicted the barrier leading to H_2 formation may be small or non-existent. The other one developed by Dunne, Murrel and Jemmer (DMJ) by flitting many body potential to the electronic energies calculated by *ab initio* configuration in-

teraction (CI) method also disagreed to the presence of any early barrier [30]. A nonreactive PES was also developed in an attempt to calculate state-to-state rotational cross section of astrophysical interest [33, 34]. This PES was found to be in excellent agreement with the one developed in Ref. [29].

The DMJ PES [30] was the first full three dimensional surface constructed for this reactive system. This PES is semi-empirical in the sense that, the available spectroscopic data were utilized to fit the two-body terms in it. The rest of the surface was fit to the calculated *ab initio* potential energies. As stated above, this surface did not yield any early barrier in the H + LiH reagent valley. Presence of a large energy minimum in the Li + H_2 product valley on this PES appeared to be an artifact in relation to subsequent developments. Wernli *et al.* [35] carried out large scale complete active space self consistent field (CASSCF)-multireference configuration interaction (MRCI) calculations employing correlation consistent polarized valence quadruple zeta (cc-pVQZ) basis set for the electronic ground state of the H + LiH collisional system. The calculated energy data were subsequently fitted by them to develop a global three-dimensional PES in an analytic form. A reaction exothermicity of ~ 2.258 eV [35] as compared to 2.23 eV [30] on the DMJ PES was obtained for the LiH depletion path on this PES. The barrier to the reaction was also found to be absent on the PES of Wernli *et al.* [35]. The van der Waals well found in the Li + H_2 product valley on the DMJ PES was found to be absent on the new PES by Wernli *et al.* [35].

Lee *et al.* [36] have carried out CI calculations for various nuclear arrangements of H + LiH collisional system and have pointed out the importance of electronic surface coupling on the reactivity of this system. From a topographical analysis these authors found that, Li($3s$) + $H_2 \longrightarrow$ LiH + H, reaction is highly improbable

in accordance with the failure in detecting any LiH in a recent experiment [37,38]. It is established also by Wernli *et al.* [35] that the highly exoergic, H + LiH $\longrightarrow$ Li + H_2, reaction can produce the Li atom either in its ground 2s or excited 2p electronic state. These two electronic states were shown to undergo avoided crossing around 1.6 Å and 0.9Å, respectively, along the LiH and H_2 bond distances and at $\sim 100^0$ along the H-Li-H bond angle [35]. A detailed comparative account of the topographical features of the low-lying electronic states of the H + LiH system with the findings of Lee *et al.* [36] was given by Wernli *et al.* [35].

Prudente *et al.* [31] also developed a new PES for the H + LiH reaction and performed quantum wave packet (WP) calculations on it. This PES was generated by *ab initio* full CI calculation of electronic energies followed by fitting them to a modified version of the analytic functions of DMJ [30]. It was shown that the DMJ PES contains unphysical wells at the H-LiH and Li-H_2 valleys which are not found on the new surface of Prudente *et al.* [31] and the latter surface appears to be smoother than the DMJ PES. Although these authors did not find any barrier on the surface, employing this PES existence of a small barrier ($\sim$ 2.14 kcal/ mole) at the collinear arrangements was found by Liu *et al.* [39] in a subsequent quasi classical trajectory (QCT) study. Kim *et al.* [32] have developed yet another PES of H + LiH collisional system by performing CASSCF-MRCI calculations of electronic energies followed by a Shepard interpolation. This PES also confirmed the absence of any barrier along the reaction path.

It is clear from the discussion presented above that the early PESs developed on this important reactive system suffer from several shortcomings. The recent PESs developed from high level *ab initio* calculations seem to be more accurate. Considering the fact that the crucial stationary points of a given PES (*viz.*, the

barriers and wells) govern the microscopic mechanism of a reaction, it is desirable to examine the detailed dynamics of this reactive chemical process on the recent and more accurate PESs in order to add to the understanding of the H + LiH collision processes in relation to astrophysical speculations.

The state-of-the art PES of Wernli *et al.* [35] is employed for the present H + LiH dynamical calculations. On the ground electronic PES the H + LiH collision proceeds as follows:

$H + LiH \longrightarrow H_2 + Li\ (2s)$ (R1)

$H + LiH \longrightarrow LiH + H$ (R2)

$H + LiH \longrightarrow H + LiH$ (NR)

The LiH depletion process through the R1 path is highly exoergic (~ 2.258 eV). The minimum energy path on this PES for the LiH depletion and H-exchange channel in collinear configuration are shown in figure 1.1 and 1.2 along with the same on the DMJ PES.

1.2.2 PES for H + LiH^+ reaction

Like neutral LiH_2 species, the ionic complex, LiH_2^+, got the attention of the researcher. A number of attempts were made to develop its PES. The first three dimensional PES for the electronic ground state was proposed by Searles *et al.* [40] employing moderate size gaussian atomic basis set and including energy correction. Subsequent to this Martinazzo *et al.* [41] developed a three dimensional reactive PES for the ground and first excited electronic states of the $LiH_2{}^+$ system using MRCI approach. The *ab initio* points, thus calculated were then fitted to a functional form to get the global 3D PES of the reactive system. The quadrupole-charge and polarizability-charge interactions of the H_2-Li^+ are in-

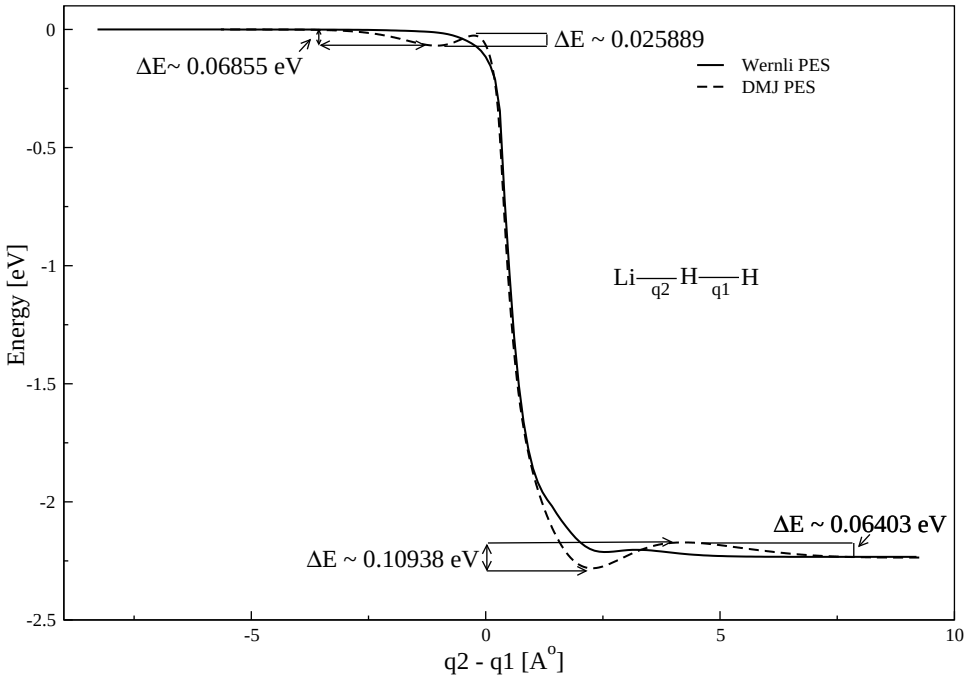

Figure 1.1: Minimum energy path for the H + HLi $\longrightarrow$ H_2 + Li reaction on Wernli PES and DMJ PES are presented by solid and dashed line, respectively.

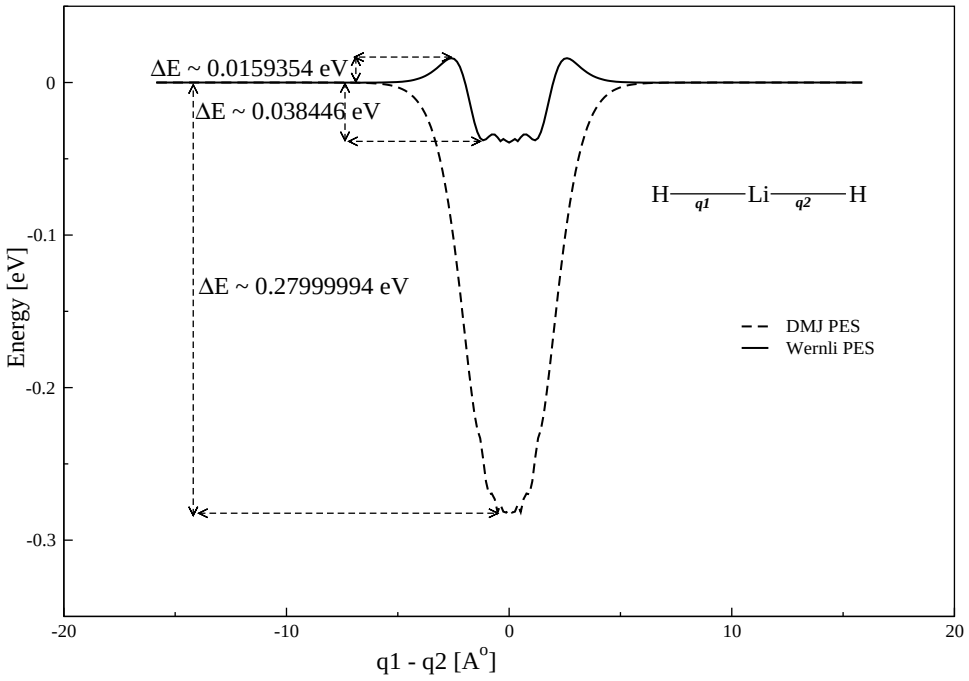

Figure 1.2: Minimum energy path for the H-exchange processes on Wernli PES and DMJ PES are shown by solid and dashed line, respectively.

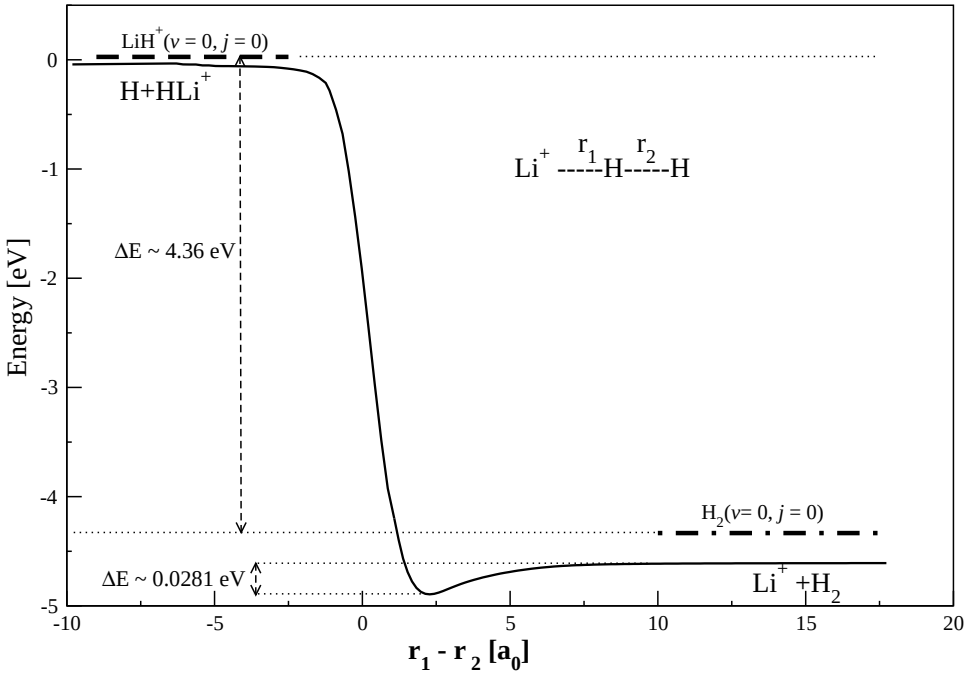

Figure 1.3: Minimum energy path (occuring at collinear geometry) for the H + HLi^+ $\longrightarrow$ H_2 + Li^+ reaction.The reaction exothermicity is $\sim$ 4.36 eV.

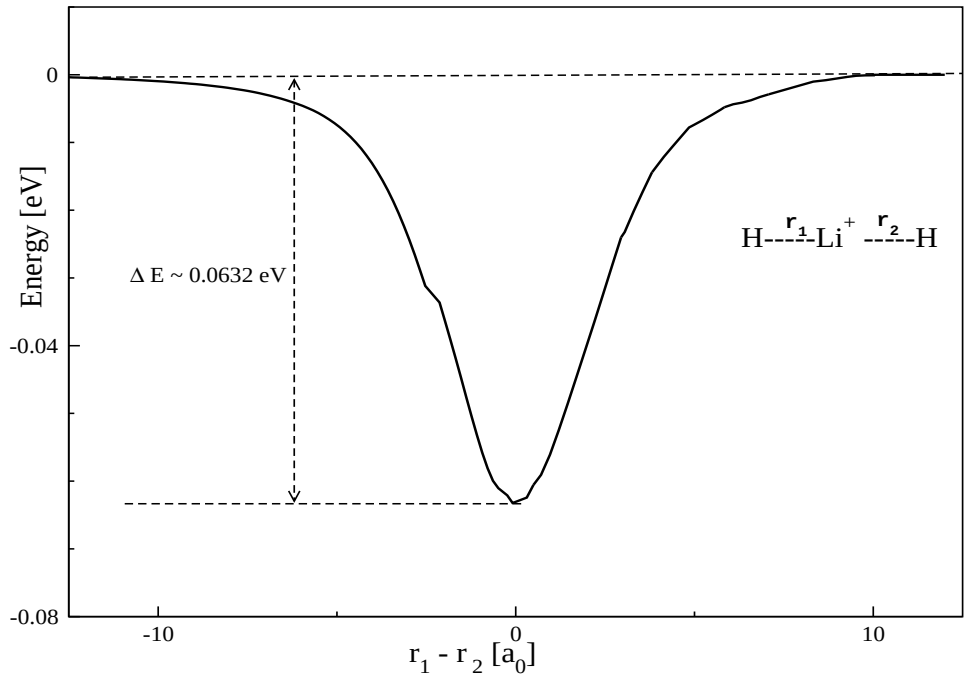

Figure 1.4: The minimum energy path for the H-exchange process (H + HLi^+ $\longrightarrow$ LiH^+ + H).

cluded in the long-range part of this PES. The root mean square deviation of the analytic fit of the long range part from the computed *ab initio* points is reported to be ~ 7.0 cm^{-1}. The energetic separation between the ground and first excited electronic state is found to be quite large [42]. Therefore, the nuclear dynamics on the electronic ground state can be treated adiabatically. This PES seems to be reasonably accurate till date despite the fact that its fittings were globally optimized in the configuration space and the *ab initio* calculations lack the basis set superposition error corrections. More recent theoretical study, on this system, both in CASSCF - MRCI [43] and Full-CI [44] levels essentially agree with the result of the Martinazzo *et al.* [41].

In the present calculations the ground state PES of the Martinazzo *et al.* [41] are employed to study the nuclear dynamics. In contrast to LiH_2, the topography of LiH_2^+ PESs seems to be more complex [45–47]. The H + LiH^+ scattering on its electronic ground state may proceed through the following paths.

(*i*) H + $LiH^+ \longrightarrow H_2 + Li^+$ (depletion, R1),

(*ii*) H + $LiH^+ \longrightarrow LiH^+ + H$ (exchange, R2),

(*iii*)H + $LiH^+ \longrightarrow H + LiH^+$ (non-reactive, NR),

(*iv*) H + $LiH^+ \longrightarrow H + H + Li^+$ (collision-induced-dissociation, CID),

(*v*) H + $LiH^+ \longrightarrow Li + H_2^+$ (charge-exchange depletion, CED) and

(*vi*) H + $LiH^+ \longrightarrow LiH + H^+$ (charge transfer, CT).

Among these the first two are reactive channels. While the channel R1 is highly exoergic (by ~ 4.4 eV) and follow a steep downhill path, the channel R2 follow a potential well of ~ 0.063 eV. The minimum energy paths of these reactive channels are shown in figures 1.3 and 1.4, respectively. It can be seen that both the reactive processes proceed via barrierless paths. The channel NR is nonreactive and the

channel CID is the collision induced dissociation channel. Due to low binding energy of the LiH^+ molecular ion ($D_0 \approx 0.112$ eV) the CID channel seems to make the primary contribution in the H + LiH^+ dynamics on the ground electronic state at the thermal conditions where the available energy is sufficient for the molecular dissociation. The contribution of this channel (*iv*) is insignificant at cold temperature conditions as the available energy is much below the dissociation energy. The (*v*) and (*vi*) channels are sufficiently endothermic [41, 46] (by $\sim$ 5.48 eV and 5.77 eV, respectively) and the absence of any nonadiabatic coupling between the two low-lying singlet electronic PESs of LiH_2^+ have suggested the charge exchange processes forbidden [42]. The steep downhill path (cf. figure 1.3) on the ground state arises from the large binding energy difference of LiH^+ and H_2 molecule. This PES has a shallow well ($\sim$ 0.286 eV below the Li^+ + H_2 asymptote) at the C_{2v} configuration.

1.3 Dynamics of H + LiH/LiH$^+$ collision : Early attempts and motivations

The dynamics of H + LiH collisions was examined on some of the developed PESs by the QCT and quantum dynamical methods [16, 18, 30–32, 39, 48–54]. In the recent past, Padmanaban *et al.* utilized the DMJ PES [30] and examined the dynamics of this reaction in detail [48–52]. The study revealed that the H exchange reaction leading to LiH formation dominates over the LiH depletion reaction leading to Li + H_2 products on this surface [48, 49]. Similar findings were also reported by Defazio *et al.* [53] by performing dynamical studies employing the same PES. In addition to the reactive dynamics study, Padmanaban *et al.* examined the resonances found on the DMJ PES [50] and the effect of

coriolis coupling [51, 52] on the reaction dynamics. It was found that the resonances can survive as long as ∼250 fs, which gives rise to an indirect mechanism to the reactive dynamics. Inclusion of coriolis interactions was found to cause a broadening of the resonances [51, 52].

As mentioned earlier this DMJ PES [30] is found to have some artifact in the subsequent studies. Existence of a barrier along the reaction path in the H + LiH reagent valley and a well in the Li + H_2 product valley at the collinear geometry is not found on the new *ab initio* PESs. The PES of Wernli *et al.* [35] has been developed with the aid of fairly high level *ab initio* electronic structure calculations. This PES, neither supports a barrier nor a well as mentioned above. It appears that this is the most accurate PES available till date for the H + LiH collisional system. As the accuracy of a theoretical calculation depends largly on the detailed topography of the PES and crucial stationary points on them, it would therefore be worthwhile and interesting to compare the results of quantum dynamics study on the Wernli *et al.* [35] PES with those obtained on the DMJ PES [48–52]. This motivated us to investigate the H + LiH reaction dynamics on the PES developed by Wernli *et al.* [35].

The collisional dynamics of H + LiH$^+$ reaction on its electronic ground state has been studied by Bodo *et al.* at collinear geometries [47]. The findings show that the CID is the major competing channel. A quasi classical trajectory calculation for this collision was also done by Pino *et al.* [54]. Using a quasi-classical capture model the author found that both the rotational and vibrational excitation of the reagent (LiH$^+$) increases the reactivity of the H-exchange channel (R2) but decreases the LiH$^+$ depletion processes (R1). They found that CID probability increases with rotational and vibrational excitation of the reagent. This author

claim that the effect of reagent rotational excitation is more prominent than vibrational excitation in promoting the CID process.

As no three dimensional quantum mechanical calculation was available in literature for this dynamics processes, we tempted to examine the collisional dynamics for this astrophysically important collisional system.

1.4 Overview of the Thesis

In chapter 2 we discuss the theoretical methods used to study the quantum dynamics. As stated earlier we did a time-dependent quantum mechanical (TDQM) calculation to study the dynamics at thermal conditions and a time-independent quantum mechanical (TIQM) methodology is used to calculate the dynamics at ultracold conditions.

In chapter 3, the initial state selected reaction dynamics of the H + LiH collision within the collision energy range $\sim$ 0.012 eV to $\sim$ 1.0 eV has been discussed on its ground electronic PES developed by Wernli *et al.* [35]. The effect of reagent rotational and vibrational excitation is discussed. The kinematic effects due to deuterium atom substitution on the reaction dynamics are also discussed. Finally the results obtained here are compared with the available literature data.

In chapter 4, we present the TDQM results of the H + LiH^+ collision proceeding through LiH^+ depletion (R1) and H-exchange (R2) path, within the collision energy range $\sim$ 0.02 eV to $\sim$ 1.0 eV. Three dimensional quantum dynamical study is carried out within the centrifugal sudden (or coupled states) (CS) approximation. Efforts have been made to minimize the contribution of dissociative

flux into the reactive ones. The channel specific integral reaction cross-section and thermal rate constants are reported.

The collisional dynamics at the ultracold and cold temperature conditions for the H + LiH and H + LiH^+ reactions are discussed in chapter 5 and 6, respectively. In these chapters, the collisional dynamics within the collisional energy range 10^{-9} eV to 0.01 eV are discussed. Time-independent quantum mechanical calculations are carried out by employing the coupled-channel hyperspherical coordinate method as implemented by Skouteris *et al.* [55] in the reactive scattering programme 'ABC'. The wave function of the atom-diatom arrangement channels are simultaneously expanded in Delves hyperspherical coordinates [56–58] in this implementation and it allows to calculate state-to-state scattering matrix elements.

The main findings are summarized in chapter 7 along with some outlook.

Chapter 2

Theoretical and computational methods

2.1 Introduction

The theoretical methods employed to study the collision dynamics on a single adiabatic PES is discussed in this chapter. Within a quantum mechanical framework both time dependent and time independent calculations can be done. Due to the inherent and technical advantages an wave packet (WP) based time-dependent quantum mechanical (TDQM) method known as time-dependent wave packet (TDWP) method is used to solve the dynamics at thermal conditions whereas time-independent quantum mechanical (TIQM) approach is used to deal with the dynamics at cold and ultracold conditions.

2.2 Time dependent wave packet approach to reactive scattering dynamics

In the TDWP approach the time dependent Schrödinger equation (TDSE), $i\hbar\frac{\partial\Psi(t)}{\partial t} = \hat{H}\Psi(t)$ is solved numerically by constructing a grid in the mass scaled Jacobi coordinate space. For the A + BC type of reaction, R (A to centre of mass of BC distance), r (BC internuclear distance) and γ (the angle between $\vec{R}$ and $\vec{r}$) refer to the Jacobi coordinates in the body fixed (BF) frame of the reagent channel. A schematic diagram of the reagent Jacobi coordinates is shown in figure 2.1 To solve the nuclear dynamics we prepare an initial wave packet (WP), which resembles the reagent and put this WP in the reagent asymptote. Then the WP is allowed to move over the potential energy surface (PES). After reaching the interaction region a part of the WP is found to go to the product channel. The amount of product formed is then measured by keeping an analysis line along a dividing surface in the product channel. In figure 2.2 we present a pictorial diagram of the position of initial WP, analysis line, damping region etc. with a reference PES of H + LiH^+ collisional system.

Study of nuclear dynamics consists of the following steps.

1. Construction of the Hamiltonian,
2. Preparation of a Spatial Grid,
3. Preparation of the initial WP in the reagent asymptote,
4. Evolution of the WP,
5. Analysis of the final WP in the product asymptote to calculate the dynamical observables.

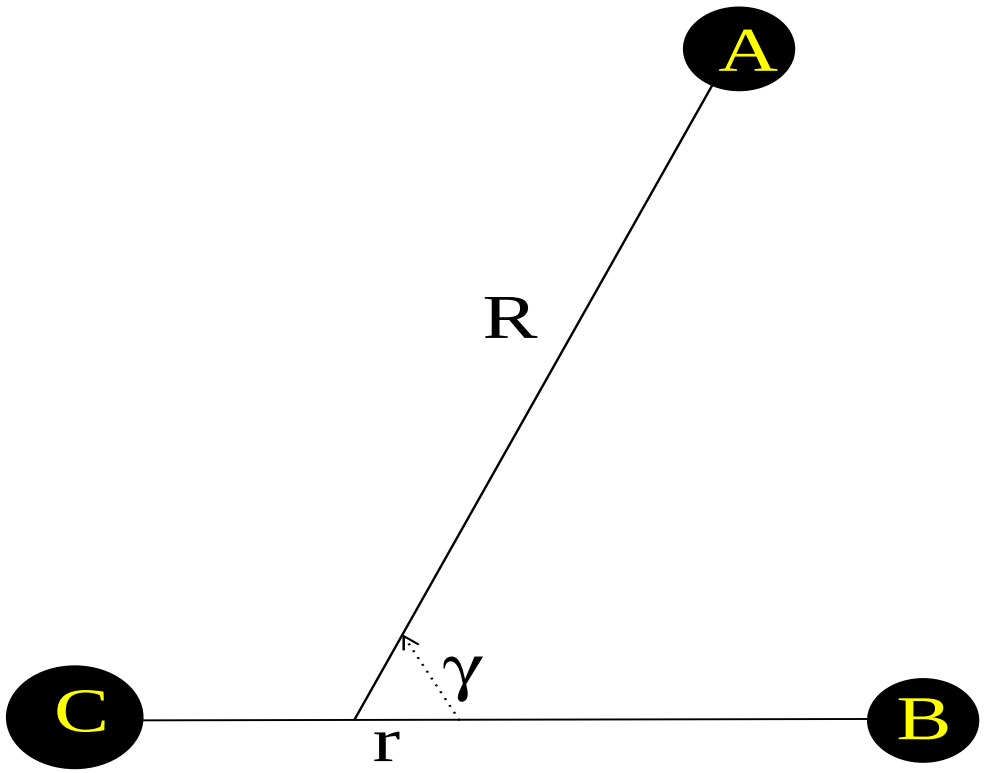

Figure 2.1: Schematic diagram of the reagent Jacobi coordinate. At R $\rightarrow \infty$, A is well separated from BC molecule. Hence this condition represent reagents. Similarly r $\rightarrow \infty$ represent products.

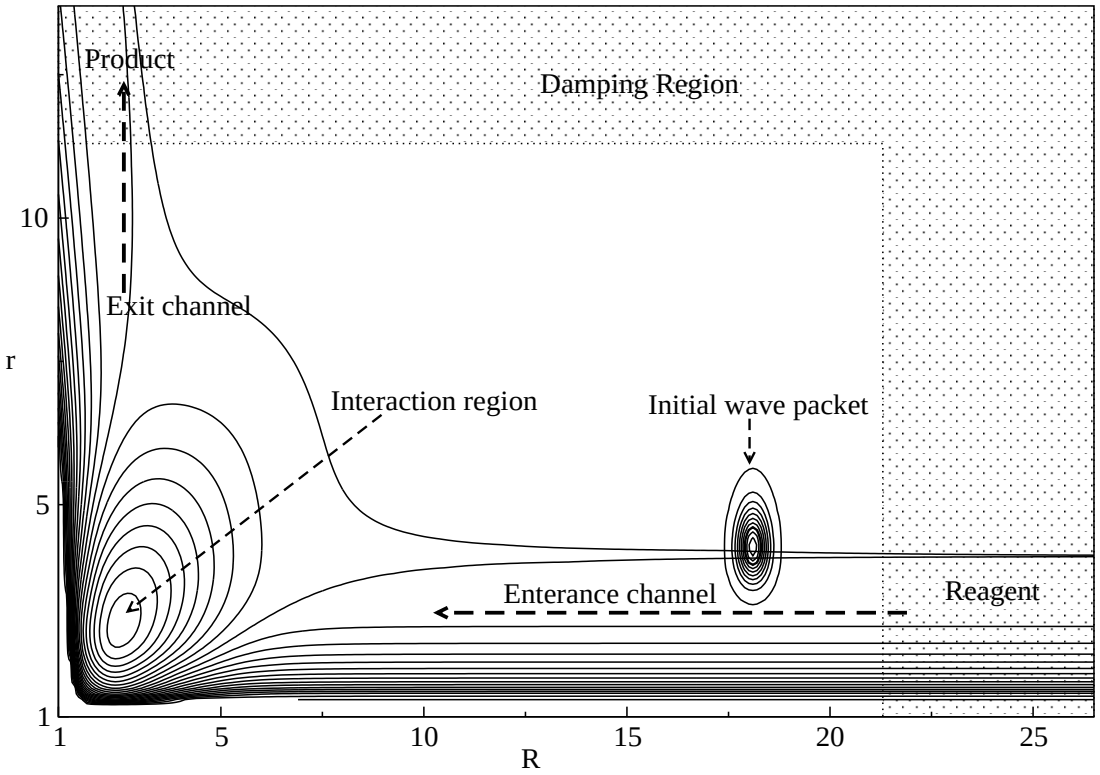

Figure 2.2: A pictorial diagram to study the collision dynamics in TDWP approach. The location of initial WP, analysis line, damping region and interaction region on the PES are shown.

2.2.1 Hamiltonian

Three dimensional adiabatic Hamiltonian of the A + BC collisional system in the mass-scaled reagent Jacobi coordinate can be written as

$$\hat{H} = -\frac{\hbar^2}{2\mu}\left[\frac{\partial^2}{\partial R^2} + \frac{\partial^2}{\partial r^2}\right] + \frac{\hat{j^2}}{2\mu r^2} + \frac{\hat{l^2}}{2\mu R^2} + V(R, r, \gamma). \tag{2.1}$$

In Eq.2.1, $\hat{j}$ is the rotational angular momentum operator of the BC molecule and is expressed as

$$j^2 = -\frac{\hbar}{sin^2\gamma}\left[sin\gamma\frac{\partial}{\partial\gamma}\left(sin\gamma\frac{\partial}{\partial\gamma}\right) + \frac{\partial^2}{\partial\gamma^2}\right]. \tag{2.2}$$

$\hat{l}$ is the orbital angular momentum operator and, $\mu = \sqrt{m_A m_B m_C/(m_A + m_B + m_C)}$, is the three-body (scaled) reduced mass. The BF z axis is defined along the Jacobi vector $\hat{R}$ while the diatom is kept in the (x,z) plane. The operator $\hat{l}^2$ can be expressed as

$$\hat{l^2} \equiv (\hat{J^2} - \hat{j^2}) = \hat{J^2} + \hat{j^2} - 2\hat{J}_z\hat{j}_z - \hat{J}_+\hat{j_-} - \hat{J}_-\hat{j_+}, \tag{2.3}$$

where $\hat{J}$ is the total angular momentum operator. $\hat{J}_z$ and $\hat{j}_z$ are the BF -z components of $\hat{J}$ and $\hat{j}$ respectively. $\hat{J}_+$, $\hat{J}_-$and $\hat{j_+}$, $\hat{j_-}$ are the corresponding raising and lowering operators. In the centrifugal sudden or coupled states (CS) approximation [59, 60] (as employed here) the last two terms of Eq.2.3 are neglected. This implies conservation of both $\hat{J}_z$ and $\hat{j}_z$ and Ω (the projection of both $\hat{J}$ and $\hat{j}$ on the BF-z axis) becomes a good quantum number. This approximation simplifies the $J \neq 0$ calculations by effectively reducing the dimensionality to three without seriously affecting the dynamical results generally [52]. $V(R, r, \gamma)$ represents the interaction potential of the collisional system.

2.2.2 Spatial Grid

The coordinate space, (x), is divided into a set of N discrete points with a spacing of Δx between two successive points. The eigenvalue of the position operator $\hat{x}$ at each grid point is given by [61, 62]

$$x_i = (i-1)\Delta x, i = 1, ..., N \tag{2.4}$$

The corresponding eigenvectors $|x_i\rangle$, are given by the orthogonality and completeness relations. The wavefunctions for an arbitrary physical state at the grid point is given by $\phi(x_i) = \langle x_i|\phi\rangle$. Wavefunctions are normalized on the grid and the normalization integral becomes $\langle\phi(x)|\phi(x)\rangle = 1$. The spacing between two successive points in the momentum space (k) is expressed as

$$\Delta k = \frac{2\pi}{N\Delta x}. \tag{2.5}$$

In the momentum space, the grid is centered at zero and all other points are distributed symmetrically on either side of it. If the maximum momentum is represented by p_{max} $(=\hbar k_{max})$ in the k space, then the total momentum ranges from $-p_{max}$ to $+p_{max}$. And the total volume of the phase space becomes, $2L|p_{max}| = Nh$.

The maximum energy on the discretized grid is given by [63]

$$\begin{aligned} E_{max} &= T_{max} + V_{max} \\ &= \frac{\pi^2\hbar^2}{2m(\Delta x)^2} + V_{max} \end{aligned}$$

The minimum energy $E_{min} = V_{min}$ is the minimum value of potential energy on the grid.

In the present construction, along the Jacobi distance R and r an equally spaced coordinate points of N_R and N_r, respectively, are used. The spacing between two points along R and r are ΔR and Δr, respectively. We construct a γ grid for each value of Ω by diagonalising the $cos\gamma$ operator in the basis of associate Legendre polynomials. The resulting diagonal elements represent the node of the N_γ-point Gauss Legendre quadrature.

2.2.3 Initial wave packet

The initial WP, $|\Psi(t=0)\rangle$, is prepared in the asymptotic reagent channel where interaction between the atom and diatom is negligible. It is taken as a product of translational wave function $F(R)$ for the motion along $\hat{R}$, the rovibrational wave function $\phi_{vj}(r)$ of the diatom and the associated Legendre polynomials to represent the motion along γ.

$$|\Psi(t=0)\rangle = F(R)\phi_{vj}(r)\hat{P}_J^{\Omega}(cos\gamma). \tag{2.6}$$

The function $F(R)$ is taken as a minimum uncertainty Gaussian wave packet (GWP)

$$F(R) = \left(\frac{1}{2\pi\delta}\right)^{\frac{1}{4}} \exp\left[-\frac{(R-R_0)^2}{4\delta^2} - ik_0(R-R_0)\right], \tag{2.7}$$

where δ is the width parameter of the GWP, R_0 is the location of the GWP in the coordinate space. The diatomic eigenfunction is obtained by solving the

eigenvalue equation

$$\left[-\frac{\hbar^2}{2\mu'}\frac{d^2}{dr^2} + V(r') + \frac{j(j+1)\hbar^2}{2\mu' r^2}\right]\phi_{vj}(r') = \epsilon_{vj}\phi_{vj}(r'). \tag{2.8}$$

Here μ' is the diatom reduced mass. ϵ_{vj} is the eigenvalue corresponding to v^{th} vibrational and j^{th} rotational state, $r' = \mathrm{r}(\mu/\mu')^{1/2}$ is the internuclear distance of the diatom BC. $V(r')$ is the diatomic potential energy obtained from the PES by setting R $\rightarrow \infty$. Sine Discrete Variable Representation (Sine-DVR) method of Cobert and Miller [64] is used to solve this eigenvalue equation.

2.2.4 Evolution of the WP

The general solution of the TDSE is given by

$$\Psi(t) = \hat{P}e^{[-i\hbar\int_0^T \hat{H}(t')dt']}\Psi(0)$$

where $\Psi(t)$ and $\Psi(0)$ represents the wavefunction at time t and 0, respectively. For an explicitly time independent Hamiltonian the solution reduces to

$$|\Psi(t)\rangle = e^{-\frac{i\hat{H}t}{\hbar}}|\Psi(0)\rangle \tag{2.9}$$

The exponential operator in the right side is known as time-evolution operator. This exponential operator contains kinetic energy ($\hat{T}$) and potential energy operator ($\hat{V}$). Since $\hat{T}$ and $\hat{V}$ do not commute with each other one needs to approximate the operator in an efficient way to minimize the commutating error. This time-evolution operator is approximated in the literature in a number of ways. For example, split operator (SO) [65–67] scheme, second order differencing scheme [68, 69], chebyshev polynomial scheme [70], short iterative Lanczos (SIL)

scheme [71] etc. In the present calculations the split operator method is used for the time evolution due to its computational efficiency.

The non commutating property of the $\hat{T}$ and $\hat{V}$ operators leads to a commutation error which is of first order of time $O(\Delta t)$, when the time evolution operator, containing the $\hat{T}$ and $\hat{V}$ in the exponential position, is split in simple straight forward way.

$$e^{-i\hat{H}t/\hbar} = e^{-i(\hat{T}+\hat{V})t/\hbar} = e^{-i\hat{T}t/\hbar} \times e^{-i\hat{V}t/\hbar} + O(\Delta t) \tag{2.10}$$

To reduces this commutation error Fleck *et al.* proposed a scheme known as split operator method [65]. In this scheme the the kinetic energy part of the time evolution operator is split symmetrically. The error arising in this way is reduced to third order in time $O(\Delta t^3)$

$$e^{-i(\hat{T}+\hat{V})t/\hbar} = e^{-i\hat{T}t/2\hbar} e^{-i\hat{V}t/\hbar} e^{-i\hat{T}t/2\hbar} + O(\Delta t^3) \tag{2.11}$$

Now the time evolution of the WP is given by

$$\begin{aligned} \Psi(t+\Delta t) &= e^{-i\hat{T}\Delta t/2\hbar} e^{-i\hat{V}\Delta t/\hbar} e^{-i\hat{T}\Delta t/2\hbar} \Psi(t) \\ &= Q\Psi(t) \end{aligned} \tag{2.12}$$

where, $Q\ Q^{\dagger} = 1$, in local representation. Though the norm is strictly conserved in this scheme, the energy conservation fails. To obtain comparatively accurate results, an optimum time step is selected based on the maximum potential energy

on the grid [65–67].

$$\Delta t < \frac{\pi}{3\Delta V_{max}}, \quad \Delta V_{max} = V_{max} - V_{min}. \tag{2.13}$$

Here it is noted that, like Eq. 2.11, the $\hat{V}$ can be split symmetrically keeping $\hat{T}$ in between. This kinetic reference SO scheme gives an identical result as that of Eq. 2.11.

After approximating with SO method, the exponential operator of E.q. 2.9 looks like

$$e^{-\frac{i\hat{H}\Delta t}{\hbar}} = e^{-\frac{iV\Delta t}{2\hbar}} e^{-\frac{iT(\gamma)\Delta t}{2\hbar}} e^{-\frac{iT(R,r)\Delta t}{\hbar}} e^{-\frac{iT(\gamma)\Delta t}{2\hbar}} e^{-\frac{iV\Delta t}{2\hbar}} + O(\Delta t)^3, \tag{2.14}$$

where, $T(R, r)$ and $T(\gamma)$ represent the radial and angular kinetic energy operators, respectively. To have a numerical solution of the Eq. 2.14, we evaluate the action of the kinetic ($\hat{T}$) and potential ($\hat{V}$) energy operators on the Hamiltonian separately. The operators $\hat{T}$ and $\hat{V}$ do not commute with each other as $\hat{T}$ is a function of the momentum (p), where as $\hat{V}$ is a function of position (x). The operation of $\hat{V}$ on Ψ is just a multiplication of its magnitude with the value of Ψ at each grid point x_i:

$$\hat{V}(x)\Psi(x_i) = V(x_i)\Psi(x_i) \tag{2.15}$$

But the kinetic energy operator ($\hat{T}$) is non local in the coordinate space and can not be evaluated by a simple multiplication.

To evaluate the radial part $T(R, r)$ of the kinetic energy operator we use the fast Fourier transformation method (FFT) [72].

In this method, the wave function $\Psi(x)$ is transformed to momentum space from the coordinate space by forward FFT (FT) followed by multiplication with the eigenvalue of the kinetic energy $T(k)$ operator, and then transforming it back to the coordinate space by an inverse FFT (FT^{-1}). In general, the continuous FFT can be represented as:

$$FT[\Psi(x)] = \overline{\Psi}(k) = \frac{1}{\sqrt{2\pi}} \int_{-\infty}^{\infty} \Psi(x) e^{-ikx} dx. \tag{2.16}$$

$$FT^{-1}[\overline{\Psi}(k)] = \Psi(x) = \frac{1}{\sqrt{2\pi}} \int_{-\infty}^{\infty} \overline{\Psi}(k) e^{ikx} dk \tag{2.17}$$

In this method the wave function must satisfy periodic boundary conditions and for band-limited functions this transformation is exact [72]. The amplitude of the function must be zero at the boundary of the phase space box. Otherwise, with progresses of time the WP gradually reaches the grid boundary and undergoes spurious reflections. The interference between the outgoing and reflected components of the WP introduces causes error. But wave functions (except the semilocalized wave functions) are not band-limited with finite support as they are not confined simultaneously both in coordinate and momentum spaces. However, this boundary conditions for the WPs can be met by multiplying with a suitable damping function. The unphysical reflection or wraparound of the time evolved WP at the grid boundaries is minimized in our calculations, by activating a sine-type damping function along R and r of the following form [73]

$$f(X_i) = \sin\left[\frac{\pi}{2} \frac{(X_{mask} + \Delta X_{mask} - X_i)}{\Delta X_{mask}}\right], \qquad X_i \geq X_{mask}. \tag{2.18}$$

In this equation, X_{mask} is the point at which the damping function is initiated

and $\Delta X_{mask}(= X_{max} - X_{mask})$ is the width of X over which the function decays from 1 to 0, with X_{max} being the maximum value of X in that direction. One more attractive feature of the FFT method is that it scales as $O(N \log N)$ with the number of grid points N [74]. Thus this method becomes especially suitable for large-scale problems as the computational effort increases slowly with the grid size.

But this FFT scheme fails to evaluate the rotational part of the kinetic energy operator (T_γ) as T_γ contains a $(1/\sin^2\gamma)$ term which leads to singularity in the discrete angle where $\gamma = 0$ and π. The evaluation of T_γ is performed by transforming the grid WP to angular momentum basis by using a discrete variable representation (DVR) - finite basis representation (FBR) transformation, multiplying by the diagonal value of the operator and then transforming it back to the grid representation [75, 76]. Numerically all these are done in a single step

$$\begin{aligned} e^{-\frac{iT(\gamma)\Delta t}{2\hbar}}|\Psi(\gamma')\rangle &= \sum_n \Bigg\{ \sum_j U^{\dagger}_{n',j} exp\Bigg[-\frac{i\hbar\Delta t}{4} \Bigg\{ \frac{1}{\mu R^2}[J(J+1) - 2K^2] \\ &+ \frac{1}{I} j(j+1) \Bigg\} \Bigg] U_{j,n} \Bigg\} |\Psi(\gamma)\rangle. \end{aligned} \tag{2.19}$$

Here U is the DVR -FBR transformation matrix and is obtained by diagonalising the $cos(\gamma)$ operator on the basis of associate Legendre polynomial function by using the recursion relation,

$$c_{l+1}\tilde{P}^{\Omega}_{l+1}(\cos\gamma) - cos\gamma\tilde{P}^{\Omega}_{l}(\cos\gamma) + c_l\tilde{P}^{\Omega}_{l-1}(\cos\gamma) = 0 \tag{2.20}$$

where [77],

$$c_l = \sqrt{\frac{l^2-\Omega^2}{4l^2-1}}\tilde{P}_l^{\Omega}(\cos\gamma) = (-1)^{\Omega}\sqrt{\frac{2l+1}{2}\frac{(l-\Omega)!}{(l+\Omega)!}}P_l^{\Omega}(\cos\gamma)$$

Colbert and Miller [64] have proposed an novel DVR technique to calculate the eigenvalue problem. This DVR technique uses the particle-in-a-box eigenfunction as a basis and is known as sine-DVR method. For a box of length $L = b - a$ (a, b are the boundary of the box) the coordinate grid points are given by

$$x_i = a + iL/N, \qquad i = 1, ..., N-1, \tag{2.21}$$

and the basis functions are given by

$$\phi_n(x) = \sqrt{\frac{2}{L}} sin\left(\frac{n\pi(x-a)}{L}\right) \qquad n = 1, ..., N-1. \tag{2.22}$$

The DVR representation of the kinetic energy is given by

$$\begin{aligned} T_{ii'} &= -\frac{\hbar^2}{2m}\Delta x \sum_{n=1}^{N-1} \phi_n(x_i)\phi_n''(x_{i'}) \qquad \text{where, } \Delta x = \frac{L}{N} \text{ is the grid spacing.} \\ &= -\frac{\hbar^2}{2m}\left(\frac{\pi}{L}\right)^2 \frac{2}{N}\sum_{n=1}^{N-1} n^2 sin\left(\frac{n\pi i}{N}\right) sin\left(\frac{n\pi i'}{N}\right) \end{aligned} \tag{2.23}$$

The analytical solution of this equation is given by [64]

$$T_{ii'} = \frac{\hbar^2}{2m}\frac{(-1)^{i-i'}}{\Delta x^2}A \tag{2.24}$$

$$\begin{aligned} \text{where,} \quad A &= \frac{\pi}{3} && \text{when } i = i' \\ &= \frac{2}{(i-i')^2} && \text{when } i \neq i'. \end{aligned}$$

We used this sine-DVR method to prepare the initial wavefunction of the diatom.

The time evolution of the WP is done by dividing the total propagation time t into N_t segments with step length Δt. Assuming that the Hamiltonian is not explicitly dependent on time, the r.h.s of the Eq. 2.9 forms a continuous dynamical group and is known as time-evolution operator denoted by $\hat{U}(t, t_0)$. Now, the time evolution is given by :

$$\begin{aligned} \hat{U}(t, t_0) &= e^{-i\hat{H}t/\hbar} \quad \text{for} \;\; t_0 = 0 \\ \hat{U}(t) &= \Pi_{n=0}^{N_t-1} \hat{U}((n+1)\Delta t, n\Delta t) \end{aligned} \tag{2.25}$$

$\hat{U}(t, t_0)$ is a linear operator and is unitary:

$$\hat{U}\hat{U}^\dagger = \hat{U}^\dagger\hat{U} = \mathbf{1} \tag{2.26}$$

2.2.5 Analysis at the product asymptotes

After solving the TDSE the initial state selected energy resolved reaction probability is calculated from the expectation value of the flux operator $\hat{F}$ at a dividing surface along product channel (at $r = r_d$). The flux operator $\hat{F}$ is given by [78–80]

$$\hat{F} = -\frac{i\hbar}{2\mu}\left[\frac{\partial}{\partial r}\delta(r - r_d) + \delta(r - r_d)\frac{\partial}{\partial r}\right]. \tag{2.27}$$

The energy normalized scattering function is obtained at the dividing surface as

$$|\Phi(R, r_d.\gamma, E)\rangle = |\psi(R, r_d.\gamma, E)\rangle/\kappa_E. \tag{2.28}$$

The function $\psi(R, r_d.\gamma, E)$ is obtained at the dividing surface through Fourier transformation of the time-dependent WP as

$$\psi(R, r_d, \gamma, E) = \frac{1}{\sqrt{2\pi}} \int_{-\infty}^{\infty} \psi(R, r_d, \gamma, t) e^{iEt/\hbar} dt|_{r=r_d}. \tag{2.29}$$

The quantity κ_E in Eq.2.28 is the weight of the translational energy component of the initial WP of total energy (relative translational + rovibrational) E, and is given by

$$\kappa_E = \sqrt{\left(\frac{\mu}{2\pi\hbar|\mathbf{k}_{vj}|}\right)} \int_{-\infty}^{\infty} F(R) exp(ikR) dR, \tag{2.30}$$

where $\mathbf{k}_{vj}$ is the initial wave vector corresponding to the approach of reagents and its magnitude is given by, $|\mathbf{k}_{vj}| = \frac{\sqrt{2\mu E}}{\hbar}$, where E is the relative collision energy of the reagent.

The reaction probability of the two channels (A + BC $\rightarrow$ AB + C and A + BC $\rightarrow$ AC + B) are separated by comparing the internuclear distances of the respective product diatoms. The WP flux is considered to represent the R1 channel if $d_{AB} < d_{AC}$ (d stands for internuclear distance) and to represent the R2 in the reverse case.

2.3 Time independent approach

Time-independent quantum mechanical calculations are performed here by employing the standard 'ABC : a quantum reactive scattering program' of Sk-

outeris *et al.* [55]. In this implementation a coupled-channel hyperspherical coordinate method is used to solve the time independent Schrödinger equation, $(\hat{H} - E)\Psi = 0$, for the motion of three nuclei on a single adiabatic PES. The Delves hyperspherical coordinates [56–58] are used in this implementation and the total propagation length (ρ) is symmetrically divided into N sector of length $\Delta\rho$. The hyperspherical basis functions ($B^{J,\Omega}_{\alpha v_\alpha j_\alpha \Omega_\alpha}$) are computed for each sector by taking the diatomic potential of each arrangement as a reference potential and is given by

$$B^{JM}_{\alpha v_\alpha j_\alpha \Omega_\alpha} = \frac{D^J_{M\Omega_\alpha}(\phi_\alpha, \theta_\alpha, 0) Y_{j_\alpha \Omega_\alpha}(\lambda_\alpha, \psi_\alpha) \Phi_\alpha(\eta_\alpha)}{\rho^{5/2} sin\eta_\alpha cos\eta_\alpha}. \tag{2.31}$$

Here α is the arrangement channel ($\alpha = 1, 2, 3$), ϕ_α, θ_α, ψ_α are the Euler angles, λ_α and η_α are the internal hyperspherical angles, v_α and j_α indicates the vibrational and rotational quantum number for the arrangement α. Here, ρ , D, Y and Φ represents hyperspherical radius, a Wigner function, spherical harmonics and a rovibrational function, respectively. The rovibrational functions (ϕ) is defined by solving a one-dimensional Schrödinger equation associated with the reference potential in that arrangement channel with the aid of finite difference method. The problems of over completeness in the small-ρ exchange region are overcome by canonical orthogonalization of the resulting multiple-arrangement basis set [81] This is done by monitoring the maximum overlaps as well as the full dimensional overlaps, which are relatively more time consuming.

For each value of total energy (E), the wave function of the atom-diatom arrangement channels ($\Psi_{J\Omega}$) are simultaneously expanded in Delves hyperspherical

coordinates in terms of hyperspherical basis function ($B^{J,\Omega}_{\alpha v_\alpha j_\alpha \Omega_\alpha}$) [82]

$$\Psi_{JM} \;=\; \sum_{\alpha v_\alpha j_\alpha} B^{JM}_{\alpha v_\alpha j_\alpha \Omega_\alpha}.g_{\alpha v_\alpha j_\alpha \Omega_\alpha}(\rho). \tag{2.32}$$

Here $g(\rho)$ is the coefficient of expansion. The number of basis function, $B(\rho)$, considered to generate Ψ are sufficiently large to make the set complete.

The time-independent adiabatic Hamiltonian of the A + BC collisional system is expressed in the Delves hyperspherical coordinate in the following way [58]

$$\hat{H} = -\frac{\hbar^2}{2\mu\rho^5}\frac{\partial}{\partial\rho}\rho^5\frac{\partial}{\partial\rho} \;+\; \frac{\Delta^2}{2\mu\rho^2} \;+\; V(\rho\lambda_\alpha\eta_\alpha)\;, \tag{2.33}$$

where Δ^2 is the Smith's grand angular momentum operator [83, 84] and is given by

$$\Delta^2 = -\frac{\hbar^2}{sin^2 2\eta_\alpha}\frac{\partial}{\partial\eta_\alpha}sin^2 2\eta_\alpha\frac{\partial}{\partial\eta_\alpha} \;+\; \frac{\hat{l}^2}{cos^2\eta_\alpha} \;+\; \frac{\hat{j}^2}{sin^2\eta_\alpha}. \tag{2.34}$$

In the 'ABC program', the angular momentum basis functions are made in helicity (k) representation not in angular momentum representation (l) and the helicity quantum number is restricted such that $|k| \leq \min(J, j, k_{max})$. Here k_{max} is the suitably chosen truncation value of k. Thus the helicity representation becomes incomplete for large value of j and J. The relationship between orbital angular momentum and helicity representation takes the following form.

$$|JMjl\rangle \;=\; \sum_{-min(J,j,k_{max})}^{min(J,j,k_{max})} |JMjk\rangle D^{Jj}_{kl} \tag{2.35}$$

where D_{kl}^{Jj} is the component of an eigenvector of the matrix representation of the operator l^2 in the truncated helicity basis. The diagonal and off-diagonal elements of the l^2 matrix are given by

$$\begin{aligned}\langle JMjk|l^2|JMjk\rangle &= J(J+1)+j(j+1)-2k^2 \quad \text{and} \\ \langle JMjk'|l^2|JMjk\rangle &= [J(J+1)-k'k]^{1/2}[j(j+1)-k'k]^{1/2}\delta_{|k'-k|,1},\end{aligned}$$

respectively.

Substitution of equation 2.32 into Schrödinger equation leads to the second order coupled matrix equations:

$$\frac{d^2g(\rho)}{d\rho^2} = O^{-1}Ug(\rho). \tag{2.36}$$

Here O and U are the overlap matrix elements and potential energy - kinetic energy coupling matrix elements, respectively, and are expressed in the following way

$$\begin{aligned}O_{\alpha v_\alpha j_\alpha \Omega_\alpha}^{\alpha' v'_{\alpha'} j'_{\alpha'} \Omega'_{\alpha'}} &= \left\langle B_{\alpha v_\alpha j_\alpha \Omega_\alpha}^{JM} | B_{\alpha' v'_{\alpha'} j'_{\alpha'} \Omega'_{\alpha'}}^{JM} \right\rangle \qquad \text{and} \\ U_{\alpha v_\alpha j_\alpha \Omega_\alpha}^{\alpha' v'_{\alpha'} j'_{\alpha'} \Omega'_{\alpha'}} &= \left\langle B_{\alpha v_\alpha j_\alpha \Omega_\alpha}^{JM} | \frac{2\mu}{\hbar^2}(\bar{H}-E) - \frac{1}{4\rho^2} | B_{\alpha' v'_{\alpha'} j'_{\alpha'} \Omega'_{\alpha'}}^{JM} \right\rangle .\end{aligned} \tag{2.37}$$

In the above equation $\bar{H}$ contains all the term of full Hamiltonian other than the ρ dependent derivative terms.

The evaluation of the O and U matrices are done by using Gauss-Legendre quadrature, trapezoidal rule and analytical integration for the λ_α angles, η_α and Euler angles (ϕ_α, θ_α and ϕ_α), respectively. The most difficult integrals involve

inter channel ($\alpha \neq \alpha'$) matrix elements, as these require evaluation of the basis for one channel at the grid points of the other. This is usually the most time-consuming part of the calculation.

The solution matrix of the expansion coefficients are propagated through all the sectors starting from a small value of $\rho = \rho_{min}$, where the interaction potential is very high, to the asymptotes ($\rho = \rho_{max}$), where the interaction potential is negligible. This is done by solving the coupled channel equation first within the sector and then chaining its value at the end of the sector with that at the beginning of the next one.

The solution of this coupled channel equations is carried out by using a constant potential log derivative method [85]. The log-derivative matrix is defined by

$$Y(\rho) = g'(\rho)g^{-1}(\rho) \tag{2.38}$$

In matrix notation, the coupled channel equation can be written as

$$g''(\rho) = W(\rho)g(\rho) \tag{2.39}$$

The matrix Ricatti [86] equation is obtained from Eq. 2.38 and 2.39

$$Y'(\rho) = W(\rho) - Y^2\rho. \tag{2.40}$$

The log derivative matrix becomes undefined whenever the determinant of the wavefunction vanishes. These singularities prohibit the use of standard numerical integration techniques for the solution of Eq.2.40. However the log derivative matrix may be safely propagated using a special form of invariant imbedding.

We define an imbedding-type propagator,ς on an interval $[\rho_1, \rho_2]$ by

$$\begin{bmatrix} g'(\rho_1) \\ g'(\rho_2) \end{bmatrix} = \begin{bmatrix} \varsigma_1(\rho_1,\rho_2) & \varsigma_2(\rho_1,\rho_2) \\ \varsigma_3(\rho_1,\rho_2) & \varsigma_4(\rho_1,\rho_2) \end{bmatrix} \begin{bmatrix} g(\rho_1) \\ g(\rho_2) \end{bmatrix}. \tag{2.41}$$

The blocks of this propagator are obtained by solving appropriate boundary value problems on the interval $[\rho_1, \rho_2]$ [87]. The stability of the matrix ς is independent of whether or not the log derivative matrix has a singularity at some point within the interval. The solution of the equation 2.41 gives the recursion relation for the log derivative matrix and is expressed as

$$Y(\rho_2) = \varsigma_4(\rho_1,\rho_2) - \varsigma_3(\rho_1,\rho_2) \times [Y(\rho_1) + \varsigma_1(\rho_1,\rho_2)]^{-1}\varsigma_2(\rho_1,\rho_2) \tag{2.42}$$

This recursion relation forms the basis of the log derivative method. The integration range is partitioned into a series of small intervals or sectors, the propagator matrix ς is constructed for each sector, and the log derivative matrix is propagated by recursive application of Eq. 2.42.

At the asymptotes, the final log-derivative matrices $Y(\rho = \infty)$ are matched to both the reactant and product states by applying the reactive scattering boundary conditions [58] to extract the related S-matrix elements.

The solution of scrödinger equation using the 'ABC reactive scattering program' yields parity-adapted S-matrix elements ($S^{J,P}_{n'k',nk}(E)$). The latter are combined and converted into a parity independent S-matrix ($S^{J}_{n'k',nk}(E)$) elements in the following way [55]

$$S^{J}_{n'k',nk}(E) = S^{J}_{n'-k',n-k}(E) = \frac{\sqrt{(1+\delta_{k'0})(1+\delta_{k'0})}}{2}\left[S^{J,+1}_{n'k',nk} + S^{J,-1}_{n'k',nk}\right],$$

and $S^J_{n'k',n-k}(E) = S^J_{n'-k',nk}(E) = (-1)^J \frac{\sqrt{(1+\delta_{k'0})(1+\delta_{k'0})}}{2} \left[S^{J,+1}_{n'k',nk} - S^{J,-1}_{n'k',nk}\right]$.

In the above equations $\alpha v j$ and $\alpha' v' j'$ are collectively expressed by n and n', respectively. From this parity independent state-to-state S-matrix we can get the state-to-state reaction probability by the following relation.

$$P^J_{\alpha' v' j' k' \leftarrow \alpha v j k}(E) = |S^J_{\alpha' v' j' k' \leftarrow \alpha v j k}(E)|^2. \tag{2.44}$$

In the above equation, α and α' are the channel indices, with α representing the reagent, A + BC, and α' the product (elastic, inelastic and reactive collisional outcome). The quantities v (v') and j (j') represent the vibrational and rotational quantum levels of reagent (product) diatom, respectively. The projection of J and j (j') on the body-fixed z axis is given by k (k'). These helicity quantum numbers are limited to $0 \leq k(k') \leq min[J, j(j')]$ within the centrifugal sudden approximation.

The state-selected total reaction probability of any channel is obtained by summing up the contribution to the probability from all open j' and v' levels of the product molecule at a given collision energy (E)

$$P^J_{vj}(E) = \sum_{v'j'k'k} P^J_{\alpha' v' j' k' \leftarrow \alpha v j k}(E). \tag{2.45}$$

The initial state-selected integral cross section for elastic, inelastic and reactive processes for total angular momentum $J = 0$ is calculated by

$$\sigma^{J=0} = \frac{\pi}{|\mathbf{k}_{vj}|^2} |T|^2 \tag{2.46}$$

where, $T = \delta_{n'n} - S_{n'n}$. n and n' are the composite index of reactant and product, respectively. Consequently, the $J = 0$ cross sections for elastic ($\sigma_{el}^{J=0}$) inelastic ($\sigma_{in}^{J=0}$) and reactive ($\sigma_{re}^{J=0}$) processes are given as

$$\sigma_{el}^{J=0} = \frac{\pi}{|\mathbf{k}_{vj}|^2}|1 - S^{J=0}_{\alpha vj \leftarrow \alpha vj}|^2, \tag{2.47a}$$

$$\sigma_{in}^{J=0} = \frac{\pi}{|\mathbf{k}_{vj}|^2}\sum_{\alpha=\alpha'}|S^{J=0}_{v'j'(\neq vj)\leftarrow vj}|^2, \tag{2.47b}$$

$$\sigma_{re}^{J=0} = \frac{\pi}{|\mathbf{k}_{vj}|^2}\sum_{\alpha\neq\alpha'}|S^{J=0}|^2, \tag{2.47c}$$

where, $\mathbf{k}_{vj}$ is the initial wave vector.

The energy dependent elastic and reactive rate constant for the s-wave scattering can be obtained by multiplying the respective cross section with the velocity vector (v), where $|v| = \sqrt{2E/\mu}$.

In the limit of ultracold temperature or vanishing collision energy ($\mathbf{k}_{vj} \to 0$) Wigner law [88] holds. The Wigner law states the the elastic, inelastic and reactive cross section will obey the following relations

$$\sigma_{el} \propto E^{2l}, \tag{2.48a}$$

$$\sigma_{in} \propto E^{l-\frac{1}{2}}, \tag{2.48b}$$

$$\sigma_{re} \propto E^{l-\frac{1}{2}}. \tag{2.48c}$$

For the s-wave scattering the above relation reduces to

$$\sigma_{el} \propto E^0, \tag{2.49a}$$

$$\sigma_{in} \propto E^{-1/2}, \tag{2.49b}$$

$$\sigma_{re} \propto E^{-1/2}. \tag{2.49c}$$

In the Wigner limit [88], the scattering can not resolve the structure of the object as the de Broglie wavelength associated with them are very long and in general much longer then the molecule. At this condition, it is not important at what potential the colliding particle scatters off but it is more important to know how the potential look at long length. The concept of scattering length is introduced here. In the Wigner limit, the scattering cross section is conveniently expressed in terms of scattering length, which is defined as [26, 89]

$$a_{vj} = -\lim_{\mathbf{k}_{vj}\to 0} \frac{\delta(\mathbf{k}_{vj})}{\mathbf{k}_{vj}}, \tag{2.50}$$

where δ represents the phase shift in the limit $\mathbf{k}_{vj} \to 0$. Basically it describes the s-wave scattering amplitude at low collision energy. For multichannel scattering, $a_{vj} = \alpha_{vj} - i\beta_{vj}$, is a complex number. In this case the poles of S-matrix can be located on either the positive or negative energy axis of the Riemann surface. [26] Bound and quasi-bound states correspond to the poles appearing on the physical and non-physical energy sheet of this surface with $Im(\mathbf{k}_{vj}) > 0$ and $Im(\mathbf{k}_{vj}) < 0$, respectively [26]. In terms of elastic component of the S-matrix the parameters

α and β are given by [26]

$$\alpha_{vj} = -\lim_{\mathbf{k}_{vj}\to 0} \frac{Im(S^{el})}{2|\mathbf{k}_{vj}|}; \tag{2.51a}$$

$$\beta_{vj} = \lim_{\mathbf{k}_{vj}\to 0} \frac{1 - Re(S^{el})}{2|\mathbf{k}_{vj}|}. \tag{2.51b}$$

2.4 Calculation of integral reaction cross section and Thermal rate constant

Initial state selected energy resolved integral reaction cross section, $\sigma_{vj}(E)$, is calculated by [90, 91]

$$\sigma_{vj}(E) = \frac{\pi}{k^2} N_{vj}(E), \tag{2.52}$$

where $N_{vj}(E)$ represents the reaction probability summed over the partial waves of the total angular momentum, J, and the rotational degeneracy. This is defined as "initial state selected cumulative reaction probability" in the literature and is expressed as [90]

$$N_{vj}(E) = \sum_{\Omega=0}^{j} \frac{g_\Omega}{2j+1} \sum_{J\geq\Omega}^{J_{Max}} (2J+1) P_{vj}^{J\Omega}(E), \tag{2.53}$$

where g_Ω represents the degeneracy factor, $g_\Omega = 1$ when $\Omega = 0$ and $g_\Omega = 2$ when $\Omega \neq 0$.

The quantity $P_{vj}^{J\Omega}(E)$ is the reaction probability obtained from the expectation value of the flux operator in the basis of the reactive scattering wave function at a given energy.

An averaging of $\sigma_{vj}(E)$ over the Boltzmann distribution of collision energies gives rise to initial state selected temperature dependent rate constant, $k_{vj}(T)$, [92]

$$k_{vj}(T) = \left(\frac{8K_BT}{\pi\mu}\right)^{1/2} \frac{1}{(K_BT)^2} \int_0^\infty E\sigma_{vj}(E)exp(-E/K_BT)dE, \tag{2.54}$$

where K_B is the Boltzmann constant.

Now the temperature dependent rate constant for a particular initial vibrational level is obtained by averaging over Boltzmann distribution of population of its rotational levels.

$$k_v(T) = \sum_j \frac{k_{vj}(T)}{Q_{rot}}(2j+1)exp(-Bj(j+1)hc/K_BT), \tag{2.55}$$

where B is the rotational constant of the LiH molecule and the rotational partition function Q_{rot} is given by

$$Q_{rot} = \sum_j (2j+1)exp(-Bj(j+1)hc/K_BT) \tag{2.56}$$

Chapter 3

Quantum dynamics of H + LiH reaction and its isotopic variants

3.1 Introduction

In this chapter, we present and discuss the initial state selected reaction probability, cross section and the thermal rate constant for the H + LiH reaction on the ground state PES developed by Wernli *et al.* [35] within the centrifugal sudden (CS) approximation [59] using the theoretical and computational procedure presented in the previous chapter (chapter 2). The collision dynamics is treated here in a time dependent quantum mechanical framework. The effect of reagent rotational and vibrational excitation are examined. The kinematic effect on deuterium substitution on the dynamics is also discussed. The results are compared with the literature data, whenever available. The results are found to have a considerable differences with the previous time-dependent quantum mechanical (TDQM) results of Padmanaban *et al.* [48, 49] on the DMJ [30] PES. The deviations of the new results with that of Padmanaban *et al.* are attributed to the

nature of the PES.

3.2 Results and discussion

3.2.1 H + LiH reaction dynamics

In the following, the probabilities of the H + LiH (v, j) reaction are calculated up to a collision energy of 1.0 eV from a lowest collision energy of $\sim$ 0.015 eV. The probabilities of the H + LiH (v=0, j=0) reaction are plotted in figure 3.1 for a few representative values of the total angular momentum J = 0, 10, 20, 30, 40, 50, 60 and 65. The solid, dashed and dotted curves in this figure represent the depletion (R1), exchange (R2) and total (R1+ R2) reaction probability, respectively. The channel specific reaction probabilities are calculated by comparing the internuclear distance (d) of the product H_2 and LiH molecules. If $d_{H_2} < d_{LiH}$ then the corresponding flux is considered to represent LiH depletion processes (R1), and in reverse case it represent the R2 processes. The reaction probabilities are converged with respect to the numerical grid parameters given in Table 3.1. Analogous to the observations by Padmanaban *et al.* on the DMJ PES, the reaction probability in figure 3.1 exhibits resonance structures at low energies. However, the detailed structure of these resonances appears to be quite different in the two cases. These resonances disappear and the scattering becomes more direct at higher collision energies and with increasing total angular momentum. It can be seen from figure 3.1 that the LiH depletion path is preferred over the H-exchange path. This is in contrast to the earlier observations [49] on the DMJ PES, in which the exchange path was found to be generally favoured. It is also found from the figure 3.1 that beyond $J > 40$, the contribution of H-exchange path (R2) is minimal.

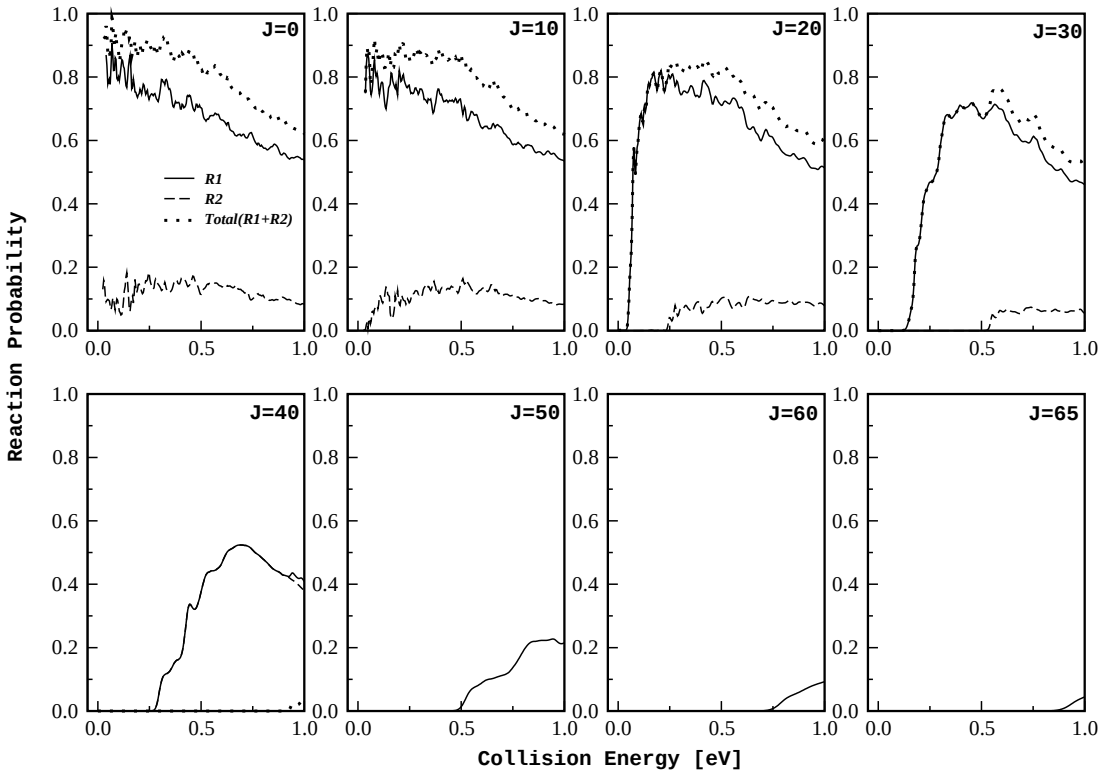

Figure 3.1: Energy resolved probability of the H + LiH ($v = 0$, $j = 0$) reaction. The probabilities of the LiH depletion (R1) and H-exchange (R2) channels are shown by solid and dashed curves, respectively. The dotted curve represents the total (R1 + R2) reaction probability.

Table 3.1: Numerical grid parameters and properties of the initial wave function used in the present study

Parameter	Value	Description
$N_R/N_r/N_\gamma$	256/64/50	Number of grid points
R_{min}/R_{max} (a_0)	1.0/34.15	Extension of the grid along R
r_{min}/r_{max} (a_0)	0.50/7.43	Extension of the grid along r
$\Delta R/\Delta r$ (a_0)	0.13/0.11	Grid spacings along R and r
r_d (a_0)	4.79	Location of the dividing surface in the product channel
R_{mask}/r_{mask} (a_0)	26.48/5.56	Starting point of the masking function
R_0 (a_0)	22.50	Initial location of the center of the GWP in the coordinate space
E_{trans} (eV)	0.6	Initial translational kinetic energy
δ (a_0)	0.23	Initial width parameter of the GWP
Δt (fs)	0.135	Length of the time step used in the WP propagation
t (fs)	675	Total propagation time

In order to access the partial wave contribution to the cross section at a given collision energy (E), degeneracy weighted reaction probability as a function of J for R1 and R2 channel are calculated and are plotted in figure 3.2. Inclusion of partial wave contribution for total angular momentum upto $J = 70$ and $J = 42$ is found to be necessary to obtain the converged cross sections for the R1 and R2 reactive channels, respectively, in the given energy range.

The integral cross sections of the H + LiH (v =0, j) reaction for the R1 and R2 channels are presented in the panel a and b of figure 3.3, respectively. The reaction cross sections are plotted as a function of collision energies, and for various rotational quantum state of the LiH molecule (j = 0 - 4). As stated before that there is no barrier found on the Wernli *et al.* [35] PES, therefore the reaction has no threshold and cross section decreases with increasing collision

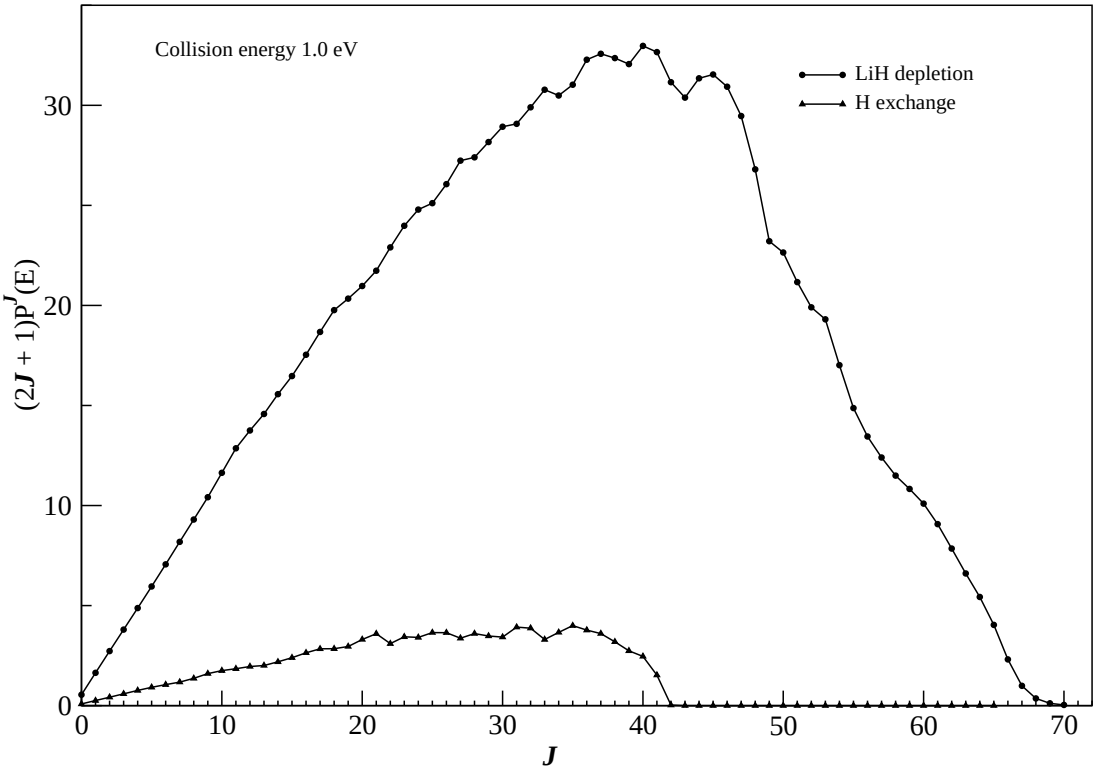

Figure 3.2: Weighted partial wave contribution to the integral cross section of the R1 and R2 channels at 1.0 eV collision energy for the H + LiH collision.

energy. It can be seen from the plots that the rotational excitation of the reagent decreases the reactivity of both the channels. The extent of decrease of reactivity of the depletion channel is quite significant between $j = 0$ and $j \neq 0$. For $j \neq 0$ the depletion cross sections are close to each other. This can be contrasted with the findings of Padmanaban *et al.* on the DMJ PES [figure 6 of Ref. 27], where it was found that the reactivity of the LiH depletion channel (R1) grows with the rotationally hot reagent LiH at low collision energies and approaches similar values at higher collision energies. The reactivity of the H-exchange channel (R2) showed a mild decrease with increasing rotational excitation. The present results are clearly in favour of the earlier TDQM findings of Padmanaban *et al.* for the R2 channel (despite the extent of decrease is large in the present case) but in contradiction with the results for the R1 channel on the DMJ PES [49]. The results reported by Liu *et al.* [39] and Kim *et al.* [32] are included for the LiH ($v = 0$, $j = 0$) depletion channel in panel a of figure 3.3. It can be seen that the present results reproduce them fairly well as regard to their trend of variation with collision energies. Most importantly, it is clear from figure 3.3 that the LiH depletion channel is favored over the H-exchange channel, in sharp contrast with the results obtained on the DMJ PES [49]. In the inset of panel a and b of figure 3.3 the present cross sections results for LiH (v =0, j =0) are compared with the earlier quantum calculations results obtained on the DMJ PES [49]. It can be seen that the two results differ significantly from each other. It is seen that the LiH depletion reactivity dominates for all j values and it is at least ten times of the H-exchange (LiH retention) reactivity.

A detailed examination of the reactivity of the H + LiH system is attempted in this chapter. We therefore tried to calculate the NR cross section in H + LiH

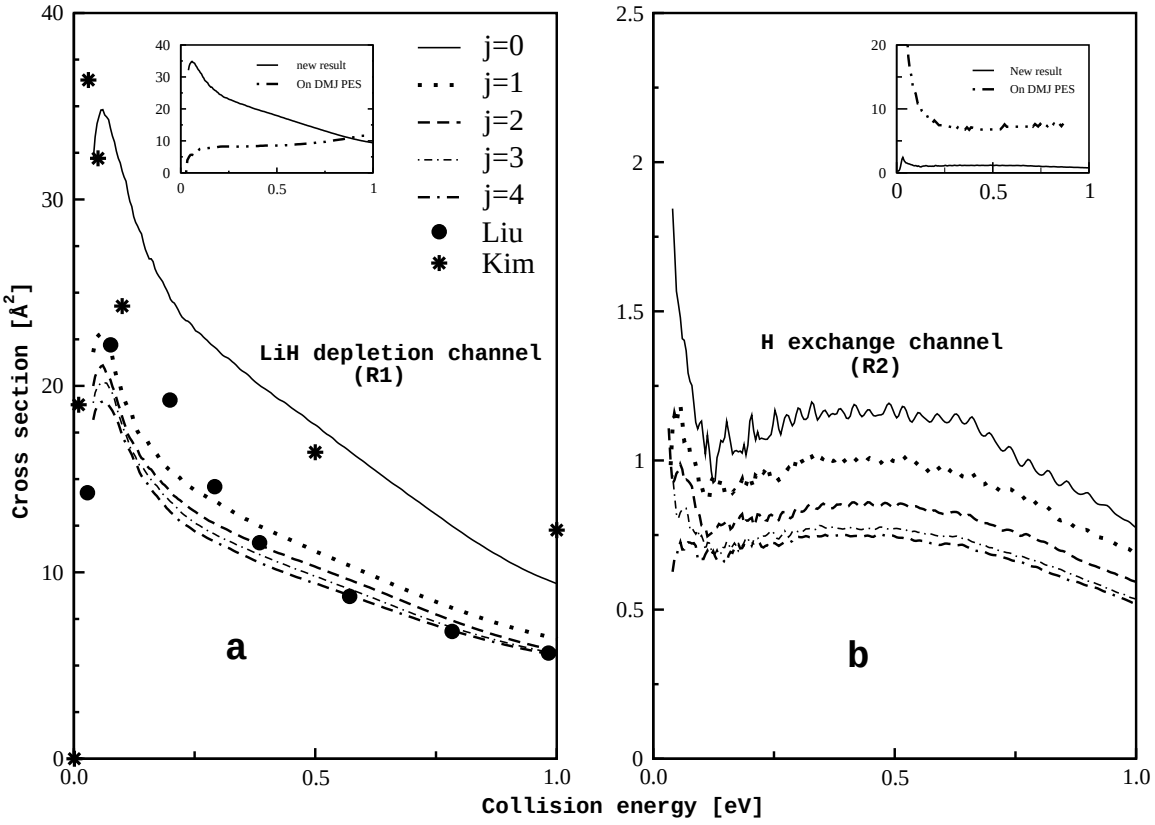

Figure 3.3: Integral cross section of the H + LiH (v =0 ,j) reaction as a function of collision energy. The cross sections for the R1 and R2 channels are plotted in panel a and b, respectively, for different j values indicated in panel a. The results of Liu *et al.* [39] and Kim *et al.* [32] for the H + LiH ($v = 0$, $j = 0$) are shown by the circle and asterisk, respectively, in panel a. In the inset of both the panels the present results for H + LiH ($v = 0$, $j = 0$) are compared with the previous findings [49] on the DMJ PES [30].

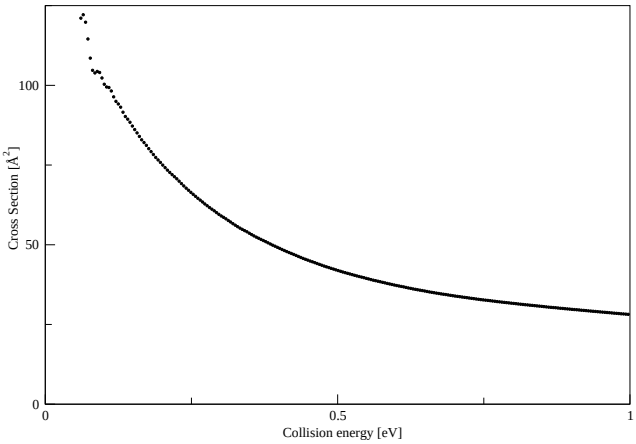

Figure 3.4: Non reactive cross section for the H + LiH ($v = 0$, $j = 0$) reaction as a function of collision energy.

($v = 0$, $j = 0$) collisions by constructing a dividing surface at large R value. The NR flux of the WP collected on this surface and integrated over r and γ value to calculate the NR probability. The latter are then converted to the integral cross sections. Contribution of partial waves for the total angular momentum up to, $J = 50$, is included in the NR cross sections. The results are plotted in figure 3.4. The NR probability dominates for higher values of J. At this point we add a caution that, calculation of NR probabilities is numerically cumbersome. This is because of the closeness of the initial WP, dividing surface and absorbing boundary in the reagent channel. This may cause some unavoidable interference effects. The NR probability can not be equated to, 1.0 - total reaction probability, in this case particularly for higher J values. The latter issue is also discussed by Bodo *et al.* [29].

Let us now examine the effect of reagent vibrational excitation on the reactivity of this system. In figure 3.5, the reactivity of the LiH depletion (panel a) and H-exchange (panel b) channel is presented for the H + LiH ($v = 0$-3, $j = 0$) reaction.

It can be seen from figure 3.5(a) that the vibrational excitation of the reagent LiH molecule causes a substantial reduction of its depletion cross section whereas, the same causes a substantial increase of its exchange reactivity [cf.,figure 3.5(b)]. These trends are in order with the earlier findings [49] on the DMJ PES, however, the extent of decrease or increase and the overall magnitude of reaction cross sections is dramatically different in the two cases. At this point it is worthwhile to compare the above findings with those available in the literature. Bovino *et al.* [16] have carried out quantum dynamics study of the H + LiH reaction by the coupled channel hyperspherical method employing the PES of Wernli *et al.* [35]. The reaction cross sections are calculated by a J-shifting method [93] in their study. These authors found that the H-exchange channel dominates at low temperature conditions whereas, the LiH depletion channel dominates at thermal conditions. The cross section results obtained at thermal conditions and presented above are in perfect accord with the observations of Bovino *et al.* [16].

A very rapid destruction of LiH in collision with ubiquitous H atom in the interstellar dust clouds has been proposed to be very likely in the recombination era [16]. Now, our finding of substantial decrease of LiH depletion cross sections with the rotational [*cf.*, figure,3.3(a)] and vibrational [*cf.*, figure 3.5(a)] excitation strongly asserts that this depletion path forms the most dominant mechanism in H + LiH collisions in the 'astrophysical conditions'.

The dynamical results on the Wernli *et al.* PES are discussed and compared with those of time-dependent quantum calculation results obtained by Padmanaban *et al.* on the DMJ PES [49] in the preceding paragraphs. Understandably the difference in two sets of results arises from a difference of the underlying

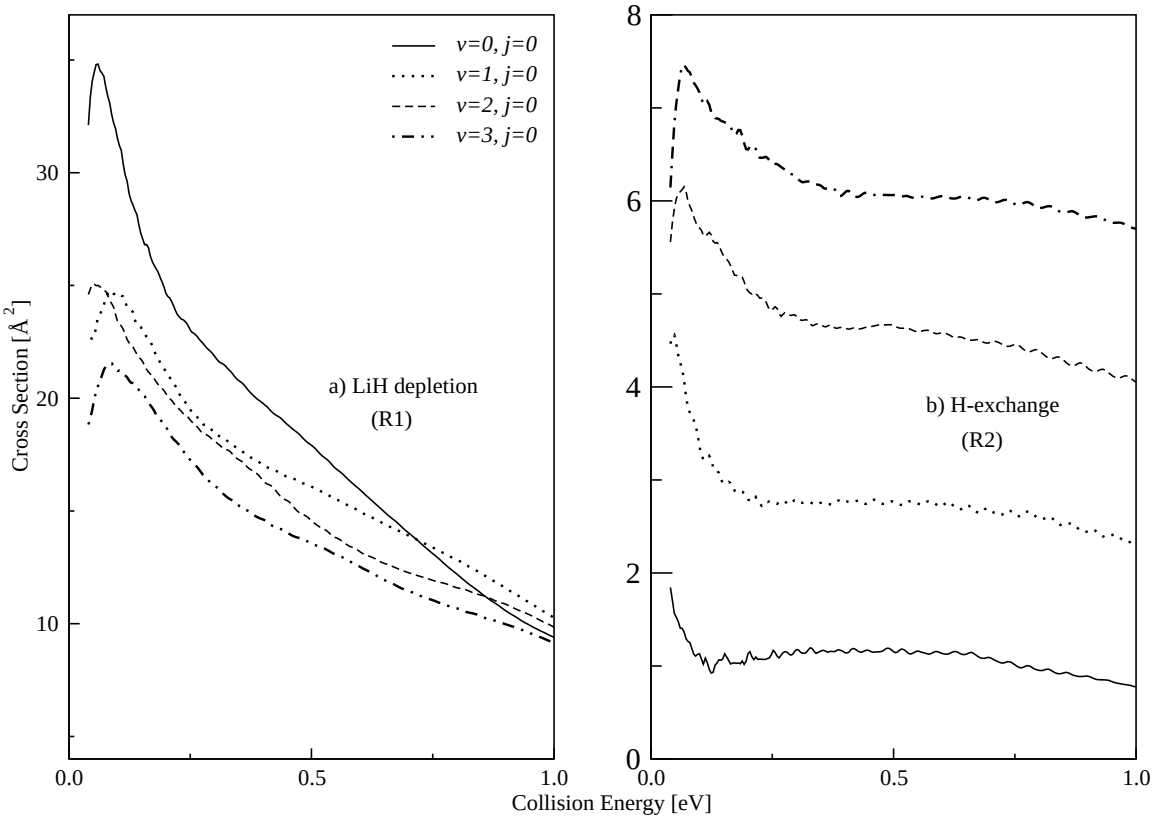

Figure 3.5: Effect of reagent vibration on the H + LiH (v =0-3, j) = 0 reaction dynamics.

PESs. It is already stated in the chapter 1 (Introduction) that the DMJ PES [30] is semiempirical whereas, the Wernli PES [35] is *ab initio* . The latter PES is highly attractive in nature along the collinear minimum energy path of the LiH depletion channel. The DMJ PES is also attractive along this path but supports two unphysical wells, one in the reagent valley (of $\sim$ 0.068 eV depth) and the another in the product valley (of $\sim$ 0.045 eV depth) relative to the asymptotes of the Wernli PES (see figure 1.1). As a result of these unphysical wells small barriers appear in the reagent and product channels along the minimum energy path on the DMJ PES. Wells of depth $\sim$ 0.28 eV and $\sim$ 0.038 eV are found on the DMJ [30] and Wernli *et al.* [35] PES, respectively, along the collinear minimum energy path of the H-exchange channel (see figure 1.2). The difference in the dynamical outcomes on the two PESs can therefore be attributed to the differences in the accuracy of the energy points and the topography of the minimum energy paths as described above.

The reactivity of a given chemical system is governed by several factors. There is no unique set of rules by which the outcome of a given microscopic chemical event can be interpreted. Statistical concepts based on the observations were developed over the past decades. These concepts and the related correlations mostly relied on the phase space theory [94], kinematic considerations and the dynamical factors [95]. The phase space theory [94] predicts an increase of reactivity with an increase in the rotational excitation of reagent molecule owing to the availability of many product states. In practice, such an interpretation could not be generalized. The kinematic considerations also played important role in the collisional outcome in many cases. Different mass combination modifies the skewing angle of the underlying PES. The dynamical factors are related

to the detailed topography of the PES, most importantly the minimum energy path [96]. It appears to be still premature to uniquely relate the dynamical outcome of a given chemical event to the specific feature of the underlying PES. Close correlations can however be made.

The reagent rotation generally decreases the reactivity of a system occurring through a preferred orientation of reagents. Rotational excitation of reagent disrupts this orientation. The present H + LiH system appears to be collinearly dominated and a decrease of reactivity with the reagent rotational excitation for lower j values supports this interpretation. A decline of reactivity with increase in the reagent rotation is also predicted for both L + LL and L + HL (L : light and H : heavy) mass combinations [95]. The present mass combination is closer to the former category. The contradictory variation of the reactivity of the R1 channel with reagent rotational excitation on the DMJ PES clearly stems from the artifacts (discussed above) present on it.

The effect of reagent vibration on the reactivity of a chemical system has been extensively studied by Polanyi and coworkers [96]. The collinear minimum energy path for the LiH depletion channel is of attractive type and there is no barrier found either in the reagent or product channel. Because of this reagent vibration is ineffective in promoting the reactivity of the depletion channel. Reagent vibration generally promotes the reactivity on a PES with a late barrier [96].

The dynamics of the H-exchange channel appears to be more complex. Existence of potential basin is found along the collinear minimum energy path of this channel [*cf* figure 1.2 on page 12]. Such a feature of the PES was also discussed in the early literature [97]. The basin appears at the distance of closest approach

of the reagents and is much deeper (vide supra) on the DMJ PES. The reagent therefore approach and cling together at the distance of closest approach. Perhaps it allows an effective transfer of translational and vibrational energies to the reactive channel on both the PESs [96].

Initial state selected temperature dependent rate constants of the H + LiH (v = 0, j) reaction calculated using Eq.(2.54) are plotted in panel a (LiH depletion rate) and b (H-exchange rate) of figure 3.6. It can be seen that the rate constant for both the channels increases with increasing temperature and then decreases at higher temperature. The increase of the reaction rate at lower temperature is much rapid for the LiH depletion channel. The LiH depletion rates are much larger than H-exchange rates at a given temperature. Analogous to the cross sections results of figure 3.3, the reaction rates also decrease with rotational excitation of the reagent LiH molecule. This is in contrast to the earlier findings on the H + LiH system on the DMJ PES [49]. In the latter, although the trend of variation of the rate constant results with temperature is analogous to the present findings, significant differences exist in their magnitude. Furthermore, LiH depletion rates revealed an opposite variation with the reagent rotational excitation as compared to the present findings. Also, in the present case the rate constant curves for both the channels [*cf.*, figures 3.6(a-b)] peak at higher temperature [$>$ 2500 K] as compared to the same found at $\sim$ 1000 K [49] on the DMJ PES.

Bovino *et al.* [16] have reported the LiH depletion rates over a wide temperature range. In their study, they calculated the rate of formation of o-H_2 and p-H_2 separately through the LiH depletion path. Except at lower temperature ($< \sim$ 1000 K) the rate of formation of o-H_2 was found to be preferred over the formation

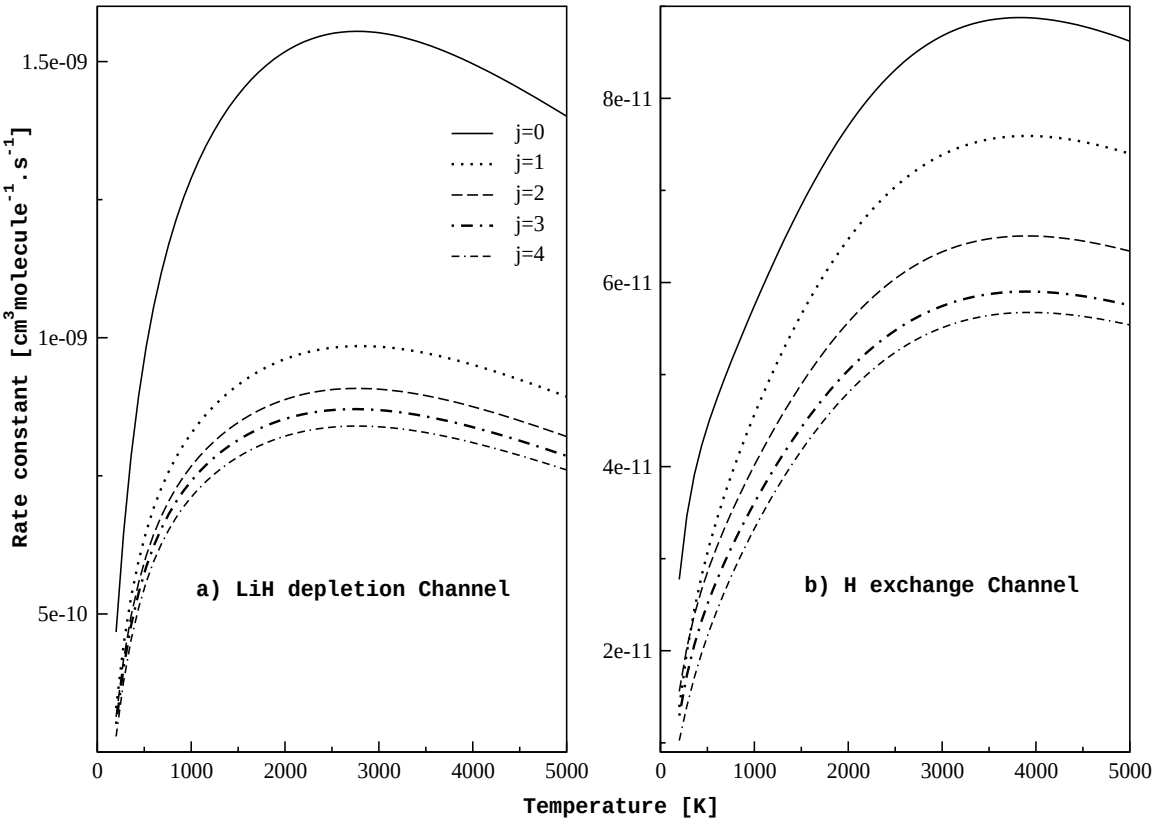

Figure 3.6: State selected thermal rate constant of the LiH depletion (panel a) and H-exchange (panel b) channels of the H + LiH ($v = 0$, j) reaction. The rate constant curves for different j values are identified by different line types and indicated in panel a.

of p-H_2. At thermal conditions the LiH destruction rate was found to dominate over the H-exchange rate. We note that the rate constant results presented by us in figure 3.6(a) represent initial state selected and averaged over all possible (at the given temperature) rotational and vibrational states of the product H_2. Our rate constant results therefore represent the statistically combined results of the rates of formation of o-H_2 and p-H_2 calculated by Bovino *et al.* [16].

To this end, we present in figure 3.7 the rate constant results averaged over thermal population of reagent rotational levels, $j = 0$-4 of the LiH depletion (panel a) and H-exchange (panel b) reactions. It can be seen that the LiH depletion rates are much larger than the H-exchange rates. Same conclusions are drawn in the recent study of Bovino *et al.* [16] on the Wernli PES [35]. For, comparison, we include the rate constant results of Bovino *et al.* [16] in panel a of figure 3.6. In this figure the stars and filled circles represent the rate of o-H_2 and p-H_2 formation, respectively, and reproduced from Bovino *et al.* [16]. It can be seen that the trend of variation of the overall depletion rate is in accord with the results of Bovino *et al.* [16]. The overall depletion rate of figure 3.7 (a) above 200 K is fit to the functional form, $k(T) = a_1(T/300K)^{a_2}exp(-T/a_3)$, as suggested by Stancil [14] in their kinetic model of lithium reactions in the primordial gas clouds. A value of temperature independent rate coefficient, $a_1 = 2.0 \times 10^{-11}$ cm^3 s^{-1}, was conjectured for the LiH depletion reaction by Stancil *et al.* [14]. A fit to the present rate constant results of figure 3.7(a) yields, $a_1 = 1.627 \times 10^{-10}$ cm^3 s^{-1}, $a_2 = 0.502$, $a_3 = 5367$ K. The rate constant data derived from this fit are superimposed on the quantum dynamics results and shown by the dotted line in figure 3.7 (a). It can be seen that the quantum dynamics results are reproduced extremely well by the fit. The rate constant results obtained by Padmanaban

et al. on the DMJ PES [49] were fit to a functional form, $k(T)$ = a$T\times$ exp(-bT), a modified version of the equation of Stancil *et al.* [14]. This equation was used in the DMJ paper [30] to fit the rate constants derived by them from QCT calculations. Using this equation, a = 9.03 $\times$ 10^{-15} cm^{3}molecule^{-1} s^{-1}K^{-1} and b = 0.0011 K^{-1} was derived by fitting the rate constants obtained on the DMJ PES [49].

Bovino *et al.* [16] have used the latter equation and derived, a = 2.05 $\times$ 10^{-12} cm^3 s^{-1}K^{-1}, b = 0.00058 for *o*-H_2 formation and a = 2.18 $\times$ 10^{-12} cm^3 s^{-1}K^{-1}, b = 0.00084 for *p*-H_2 formation through the LiH depletion path. We also used this equation to fit the overall LiH depletion rate given in figure 3.7(a) and obtained, a = 1.03575 $\times$ 10^{-12} cm^3 s^{-1}K^{-1} and b = 0.0004. These results are very similar to those of Bovino *et al.* [16]. The rate constant results obtained from this fit are also superimposed in figure 3.7(a) and are shown by the dashed line. From a comparison of various results presented above, it appears that the original fit equation of Stancil *et al.* [14] is far superior to meaningfully represent the present rate constant data. This equation with the present fit parameters may be utilized for astrophysical applications with greater confidence.

3.2.2 Kinematic effects on the H + LiH reaction dynamics

The kinematic effect due to replacement of H by D atom in the H + LiH reaction dynamics is discussed in the following. Apart from the H + LiH, three other collisional systems *viz.*, H + LiD, D + LiH and D + LiD are relevant for the discussion. All three latter collision processes proceed through similar pathways [*viz.*, depletion (R1) and exchange (R2)] as in the case of H + LiH system.

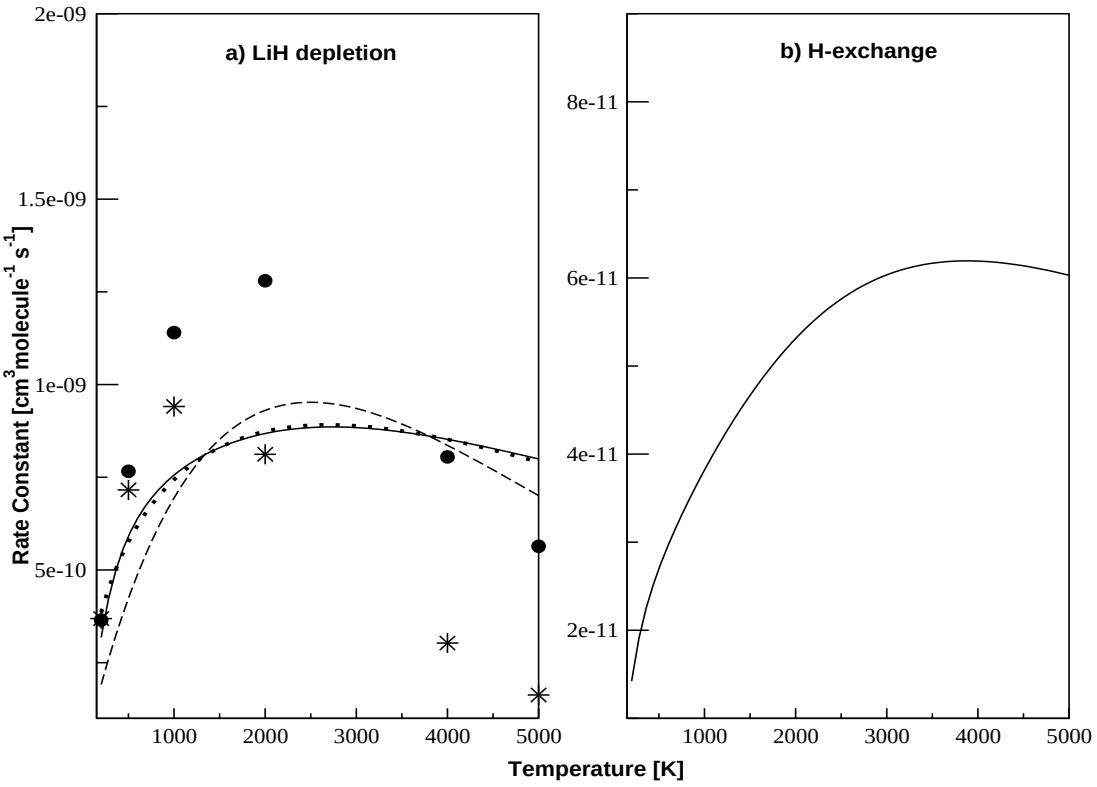

Figure 3.7: Boltzmann averaged (over j = 0-4) thermal rate constant (solid curve) of the LiH depletion (panel a) and H-exchange (panel b) channel of H + LiH (v = 0) reaction. The rate constants of LiH depletion reaction are fitted to the original functional form as well as a modified form proposed by Stancil *et al.* [14]. These fit results are superimposed in panel a and shown by the dotted line and dashed line, respectively. The rates of formation of oH$_2$ (asterisks) and pH$_2$ (filled circles) through the LiH depletion path calculated by Bovino *et al.* [16] are also included in panel a.

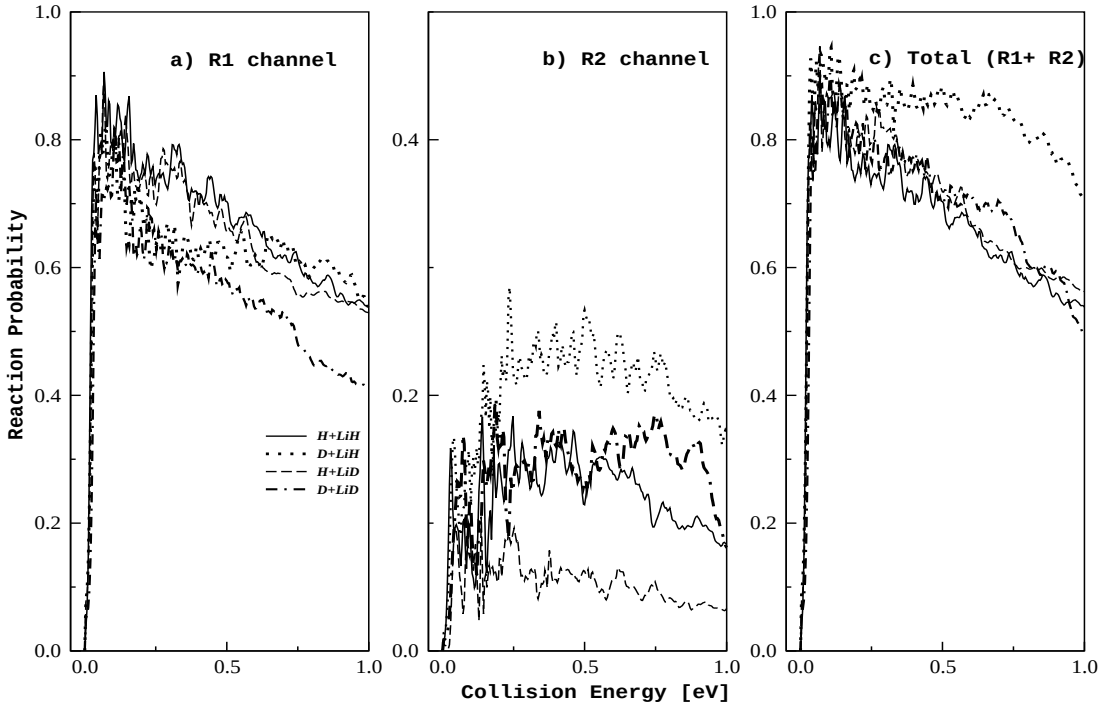

Figure 3.8: Probability as a function of collision energy for the H + LiH (v = 0, j = 0) reaction and its isotopic variants shown by different line types indicated in the panel a.

The channel specific (R1 and R2) and the total (R1 + R2) probability of the H + LiH (v =0, j =0) reaction and its isotopic variants is plotted as a function of collision energy in figure 3.8. It can be seen that the overall variation of the reaction probability for both the channels is similar. In all cases, the depletion reaction dominates over the exchange reaction. The resonances appear to be more pronounced at lower collision energies in the isotopic reactions.

Integral cross sections of the H + LiH (v =0, j =0) reaction and its isotopic analogues are plotted in panel a (R1 channel) and b (R2 channel) of figure 3.9. The resonance oscillations seen in the reaction probability curves disappear upon

averaging over many partial wave contributions of the total angular momentum J= 70 for the depletion reaction and J= 42 for the exchange reaction in the reaction cross sections. The depletion reaction dominates over the exchange reaction in each case. While the cross section values of the H + LiH, H + LiD and D + LiD reactions are very similar, the cross sections of the D + LiH reaction are significantly different from the rest. In the latter case, the cross sections of both the R1 and R2 channel are larger than those of the other three reaction. Because of larger mass of the incoming D atom, its translational velocity is lower than that of incoming H atom at a given energy. Therefore, a relatively slower approach of the D atom allows an effective transfer of its translational kinetic energy to the internal degrees of freedom of the reagent LiH molecule and causes an increase in the reaction cross sections. A steric crowding perhaps causes a decrease in the reactivity of the D + LiD reaction.

The cross section results of Liu *et al.* [39] obtained by the QCT calculations on the Prudente *et al.* PES [31] for the isotopic reactions are superimposed in panel a of figure 3.9 and shown by the open circle (H + LiH), filled circle (D + LiH), open triangle (H + LiD) and filled triangle (D + LiD). It can be seen that the trajectory results also support larger cross sections for the D + LiH reaction. They found that the product forward scattering intensity increases with increasing mass factor values defined as, $cos^2\beta = \frac{m_A m_C}{(m_A + m_B)(m_B + m_C)}$, for A +BC $\longrightarrow$ AB + C reaction [98]. This mass factor is largest (= 0.528) for the D + LiH reaction [39].

Finally in figure 3.10 the initial state selected rate constant values of the H + LiH (v = 0, j = 0) reaction and its isotopic variants are plotted as a function of temperature. The rates of the depletion and exchange reactions are plotted

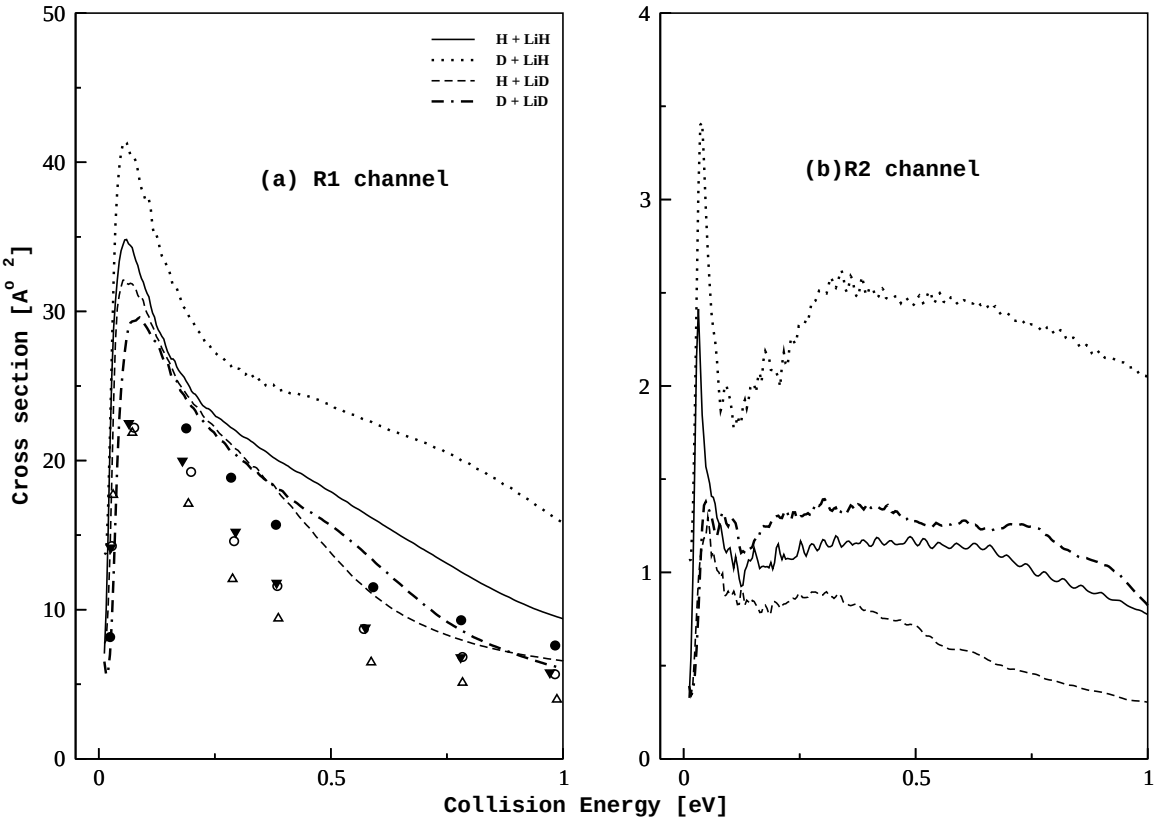

Figure 3.9: Cross Section as a function of collision energy of the H + LiH ($v = 0$, $j = 0$) reaction and its isotopic variants shown by the different line types indicated in panel a. The cross sections of the R1 and R2 channel are shown in panel a and b, respectively. The QCT results of Liu *et al.* [39] are superimposed in panel a and shown by the open circle (H + LiH), filled circle (D + LiH), open triangle (H + LiD) and filled triangle (D + LiD).

in panel a and b, respectively. Analogous to the cross section results, the D + LiH reaction rate constants are much larger for both the channels as compared to other three reactions. The rate constant of the D + LiD reaction is smallest owing to a larger reduced mass of this system.

3.3 Summary

We presented a detailed theoretical account of the H + LiH reaction dynamics on a new improved *ab initio* PES [35]. The early barrier in the reagent (H + LiH) valley and late well in the product (Li + H_2) valley are found to be absent on this PES. The dynamics calculations are carried out with the aid of a time-dependent WP method. The results are compared with the time-dependent quantum mechanical results of Padmanaban *et al.* obtained on a semi-empirical PES (DMJ PES) and also with the available recent literature data. While the present results are in very good accord with the available results from the recent literature, they deviate significantly from the earlier quantum mechanical findings on the DMJ PES. The major findings of the present investigations are the following.

1. The reactivity of the LiH depletion channel is far greater than that of the H-exchange (LiH formation) channel. This is in accord with the findings in the current literature.

2. Reactivity of both the LiH depletion and the LiH formation (H-exchange) channel decreases with rotationally hot reagent LiH. The exchange reactivity is at least ten times lower than the depletion reactivity.

3. While the vibrational excitation of the reagent LiH decreases the reactivity of the depletion channel, the same increases the reactivity of the H-exchange

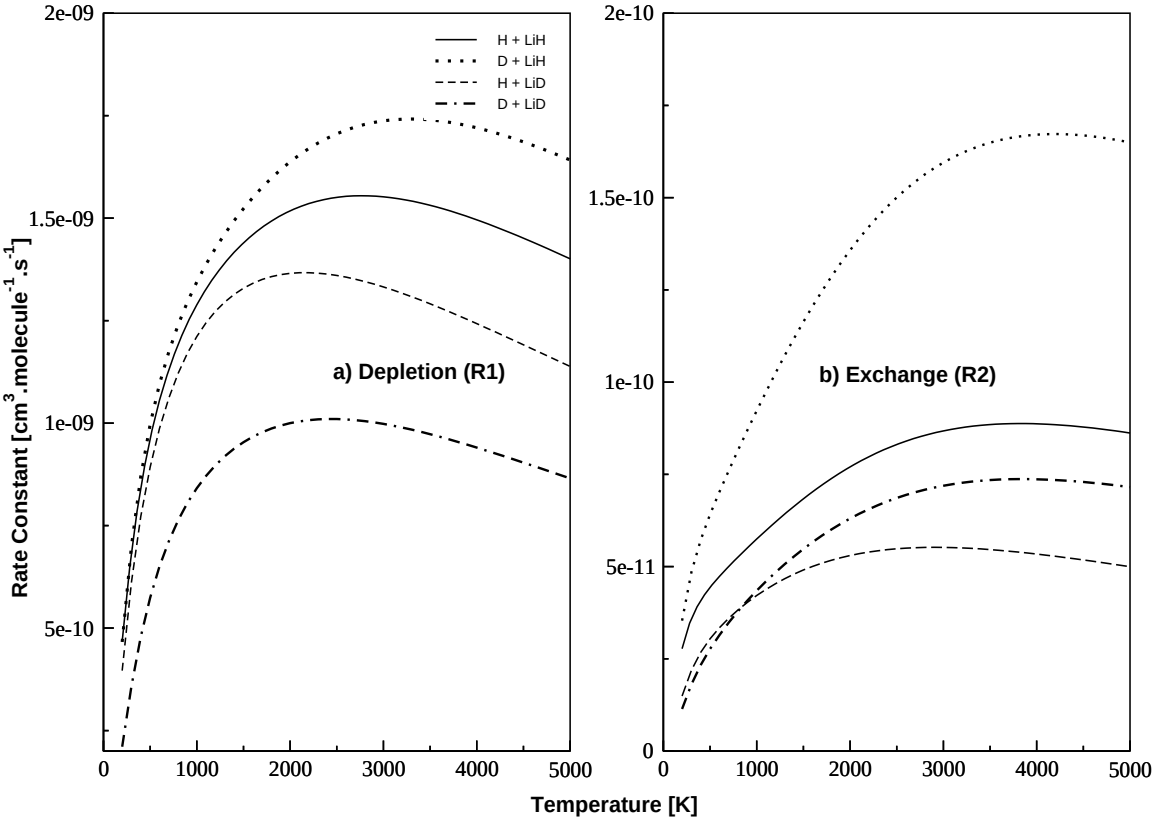

Figure 3.10: Rate constant as a function of temperature of the H + LiH ($v = 0$, $j = 0$) reaction and its isotopic variants shown by the different line types indicated in panel a. The rate constant values of the depletion and exchange channel are shown in panel a and b, respectively.

channel.

4. The rates of the depletion channel is much larger than that of the exchange channel. The present reaction rates calculated employing the most accurate PES available on this system elegantly fit to a formula, $k(T) = 1.627\times10^{-10}cm^3s^{-1}\times(T/300K)^{0.502}exp[-T/5367K]$, for the depletion channel. Considering the high accuracy of the present rate constant data, the above analytical equation is expected to be valuable for important astrophysical applications.

5. Isotopic substitution revealed that the reactivity of the D + LiH reaction is largest. This is in accord with recent quasi-classical trajectory results. Lower translational kinetic energy of the D atom (compared to the H atom) at a given energy causes an efficient transfer of energy to the internal degrees of freedom of the LiH molecule and increase the reactivity.

Finally it is gratifying to note that the above findings are in accord with the conjecture that the LiH molecules are efficiently destroyed by collision with ubiquitous H atoms in the astrophysical environments.

Chapter 4

Quantum dynamics of H + LiH^+ reaction on its electronic ground state

4.1 Introduction

The initial state selected reaction dynamics for the H + LiH^+ reaction on its electronic ground PES is studied by a time dependent wave packet (TDWP) method described in chapter 2. The initial state selected and energy resolved reaction probabilities, integral reaction cross sections and thermal rate constants of the H + LiH^+ reaction are presented and discussed in this Chapter. The effect of reagent rotational excitation ($v = 0$, $j = 0$ - 4) is also discussed. As discussed in the chapter 1 [page 14], the collision dynamics in the thermal conditions on the ground electronic PES may proceed through the following four paths

(i) H_2 + Li^+ (depletion, R1),

(ii) LiH^+ + H (exchange, R2),

(*iii*) H + LiH^+ (non-reactive, NR) and

(*iv*) H + H + Li^+ (collision-induced-dissociation, CID).

The first two paths (R1 and R2) are the reactive paths and because of low binding energy of the reactant LiH^+ molecule ($D_0 \approx 0.112eV$), the reagent has a high possibility to dissociate. In fact, in thermal collision CID is the major competing channel [47, 54].

The channel specific reactive probability is calculated by comparing the internuclear distance of the product diatom. The H_2 formation channel R1 is populated when $d_{H_2} < d_{HLi^+}$ (where d is the internuclear distance), otherwise the H exchange channel R2 is populated. Since the CID channel is a major competing channel in the dynamics and since both the reactive and dissociative flux proceed through the same dividing surface, we minimize the contribution of CID flux into the reactive one by discarding the WP flux having $d_{H_2} > 4.2\ a_0$ from R1 and $d_{LiH^+} > 9.1\ a_0$ from R2. These are the distances which represent approximately the dissociation threshold of the respective diatomic potential energy function estimated from the employed PES in this study. Admittedly, this is the only strategy than can be adopted in the Jacobi coordinate framework. This may however appears crude, but nevertheless this strategy does discards considerably the CID flux flowing into both the reactive channels. Despite the best efforts made to prevent the flow of the dissociative WP flux into the reactive channels, there may still remain some minor contribution as the CID seems to be a major channel in this reaction.

4.2 Results and discussion

The reaction probabilities are calculated up to a collision energy of 1.0 eV. The convergence of the result is checked with respect to the numerical grid parameters listed in Table 4.1. It is found that the reaction dynamics is quite sensitive to the choice of the location of the dividing surface in the asymptotic product channel. We tried with several choices and finally fixed the dividing surface at r=10.5 a_0 which yields the best converged results along with the other numerical parameters given in Table 4.1.

The channel specific total reaction probabilities as a function of collision energy are plotted in figure 4.1 for a few representative values of the total angular momentum, $J = 0, 10, 20, 40, 60$ and 90. The probabilities of the LiH^+ depletion channel (R1) and the hydrogen exchange channel (R2) are shown by the solid and dotted lines, respectively whereas, the total reaction probability (R1 + R2) are shown by the dashed lines. Since the reaction is intrinsically barrierless it proceeds without any threshold as can be clearly seen from the J=0 reaction probability curves. For higher J values the reaction develops a threshold originating from an increase in the height of the centrifugal barrier and hence the onset of the reaction probability curve shift towards the higher collision energy. The centrifugal potential term ($V_{cent} = \frac{\hbar^2[J(J+1)]-2K^2}{2\mu R^2}$) adds a barrier to the PES and the height of the barrier increases with J. Sharp resonance structures at low energies for both R1 and R2 channels are found in figure 4.1 which implies the formation of metastable complex during the course of the reaction. The resonances are less prominent at higher energies, revealing a more direct nature of the collision dynamics. The LiH^+ depletion channel (as can be seen from figure 4.1) is preferred over the hydrogen exchange channel for the H + LiH^+ reaction.

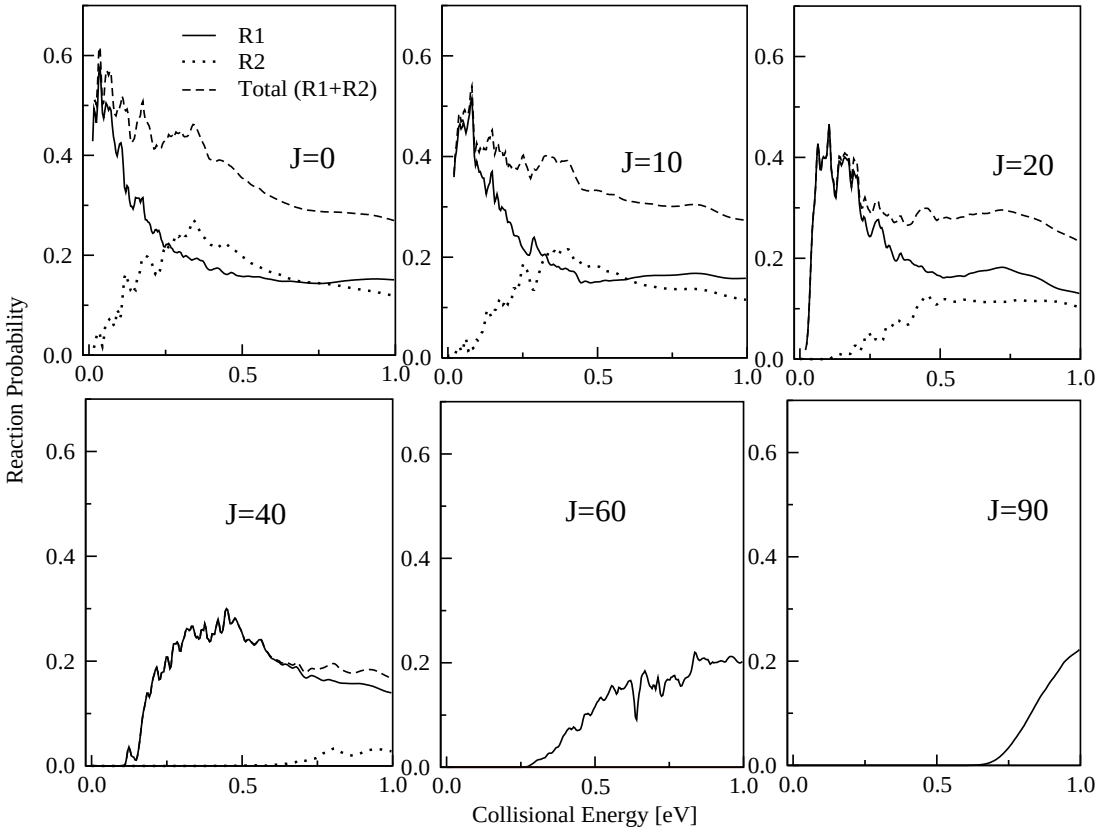

Figure 4.1: The probability of H + LiH^+ ($v = 0, j = 0,$) reaction as a function of collision energy. The probabilities of R1 and R2 channel are shown by the solid and dotted lines, respectively. The dashed line indicate the total probability of the H + LiH^+ reaction.

Table 4.1: Numerical grid parameters and properties of the initial wave function used in the present study.

Parameter	Value	Description
$N_R/N_r/N_\gamma$	256/128/48	Number of grid points
R_{min}/R_{max} (a_0)	1.0/26.50	Extension of the grid along R
r_{min}/r_{max} (a_0)	1.0/13.70	Extension of the grid along r
$\Delta R/\Delta r$ (a_0)	0.10/0.10	Grid spacings along R and r
r_d (a_0)	10.50	Location of the dividing surface in the product channel
R_{mask}/r_{mask} (a_0)	21.30/11.00	Starting point of the masking function
R_0 (a_0)	18.10	Initial location of the center of the GWP in the coordinate space
E_{trans} (eV)	0.5	Initial translational kinetic energy
δ (a_0)	0.25	Initial width parameter of the GWP
Δt (fs)	0.135	Length of the time step used in the WP propagation
T (fs)	540	Total propagation time

Reaction probabilities of both R1 and R2 channels decrease with increasing J. It can be seen from figure 4.1 that within the given collision energy range of $\sim$ 0.02 eV - 1.0 eV, the exchange channel makes negligible contribution beyond J=40. Therefore, for higher angular momentum the reactivity of the H + LiH^+ system is governed by the depletion path. Resonances also become less prominent for higher J values.

The J-dependence of the degeneracy $(2J+1)$ weighted reaction probability for the R1 and R2 channels at a collision energy of 1.0 eV are plotted in figure 4.2. Partial wave contributions up to $J = 95$ and $J = 36$ were found to be necessary to obtain converged reaction cross section for the R1 and R2 channels, respectively. It can be from the figure 4.2 that the weighted probability value initially increases with J and then decreases at higher values of J. The initial increment here is

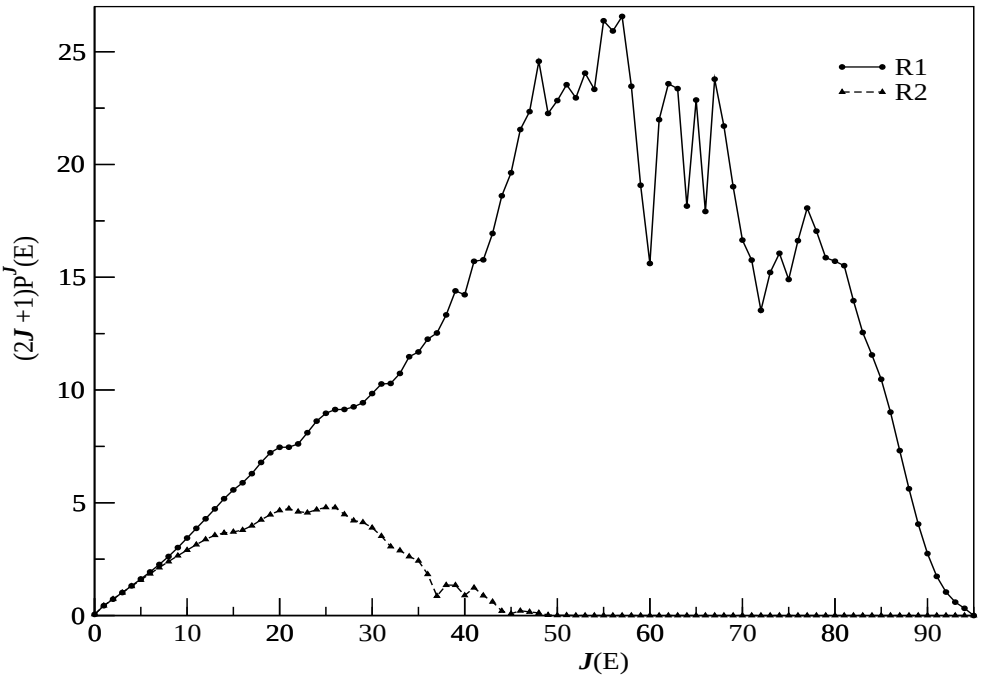

Figure 4.2: Weighted partial wave contribution to the integral cross section of the R1 and R2 channels at 1.0 eV collision energy for the H + LiH^+ reaction.

due to the $(2J + 1)$ degeneracy factor and the diminution in the later part (large J value) is due to the shift of the reaction threshold caused by the centrifugal barrier. The initial state selected and channel specific cross section as a function of collision energy of the H +LiH^+ reaction are shown in the figure 4.3 (a-b). These are integral cross sections represent a weighted sum of the reaction probabilities over different partial wave contributions [-min$(j, J) \leqslant \Omega \leqslant +min(j, J)$] calculated by using the Eq. 2.52 [chapter 2, page 42]. The reaction cross sections are calculated for $v = 0$ and $j = 0 - 4$ of the reagent LiH^+ and are shown by different line types indicated in panel a. The reaction cross sections are converged for the lowest collision energy of ~ 0.02 eV. Analogous to the observations made for the neutral H + LiH reaction , the cross sections for the H + LiH^+ reaction for

the R1 channel generally decrease with increasing collision energy. For hydrogen exchange channel (cf. figure 4.3(b)) the cross section show some increase for the intermediate collision energies ($\sim$ 0.2-0.4 eV), then decreases with further increase in collision energy. With reagent rotational excitation the cross sections decreases for both the channels. The disruption of the preferred geometry with reagent rotation probably causes this diminution of reactivity [95]. The resonance oscillations seen in the reaction probability curves of figure 4.1 average out with different partial wave contributions in the reaction cross sections. The reaction cross sections of the LiH^+ depletion channel are much larger than the hydrogen exchange channel for any given initial state (v = 0, j = 0 - 4) of the reactant. This is in accordance to the findings on the H + LiH reaction presented in the previous chapter (Chapter 3). The reaction cross sections obtained by a three-dimensional QCT calculations are extracted from Ref. [54] and compared with our $v = 0$, $j = 0$ results in the inset of figure 4.3(a-b). The QCT and the present quantum mechanical results are shown by the dashed and solid lines, respectively. It can be seen that the overall trend of variation of cross section with energy is similar in both cases, although their magnitude differs.

Thermal rate constants for the H + $LiH^+(v = 0, j = 0-4)$ are calculated up to 10000 K within the CS approximation. The state selected thermal rate constant, k_{vj}(T), calculated with the aid of Eq. 2.54 are shown in figure 4.4(a-b). Rate is found to increase with temperature, reaches a maximum and then decrease with further increase of temperature. Similar to the trend of cross section, k_{vj}(T) shows a decrease with increasing j for both the R1 and R2 channels.

The Boltzmann averaged (over $j = 0-4$) thermal rate constants of the depletion and exchange channel are shown in figure 4.5. It can be seen that the depletion

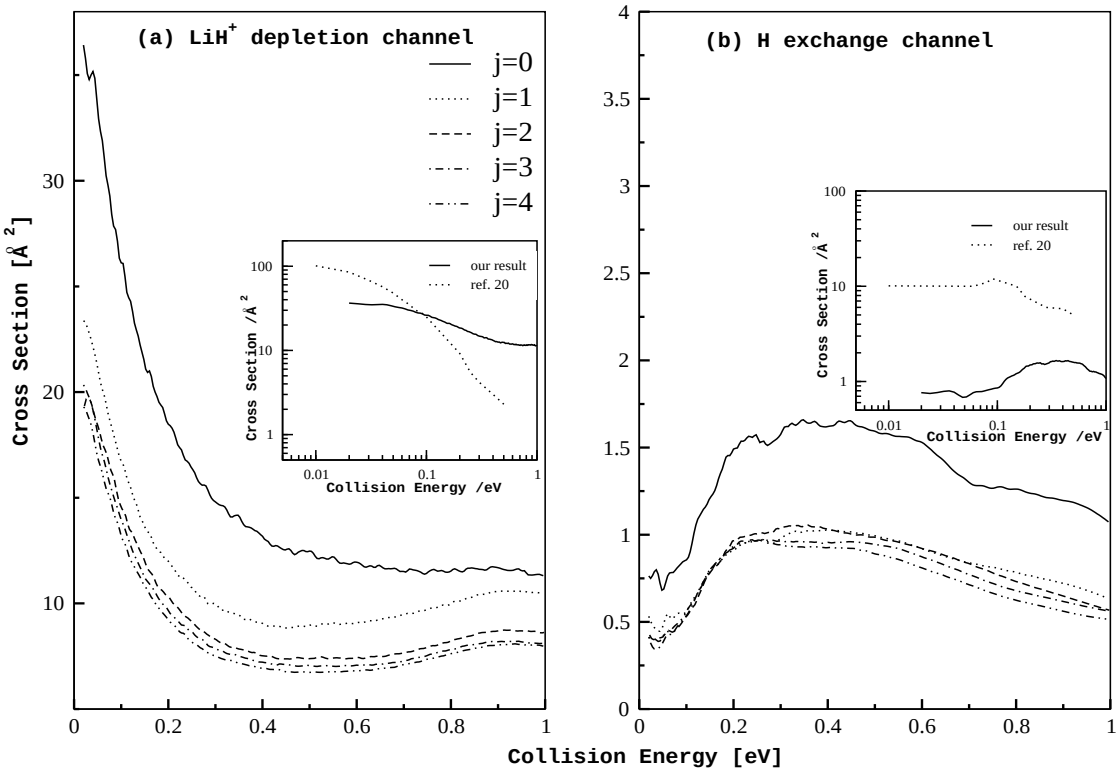

Figure 4.3: Channel specific integral cross-section as a function of collision energy for the H + $LiH^+(v = 0, j)$ reaction. The QCT cross sections for the $v = 0$, $j = 0$ reaction (dotted line) are extracted from the ref. [54] and compared with our results (solid lines) in the inset of both the pannel a and b.

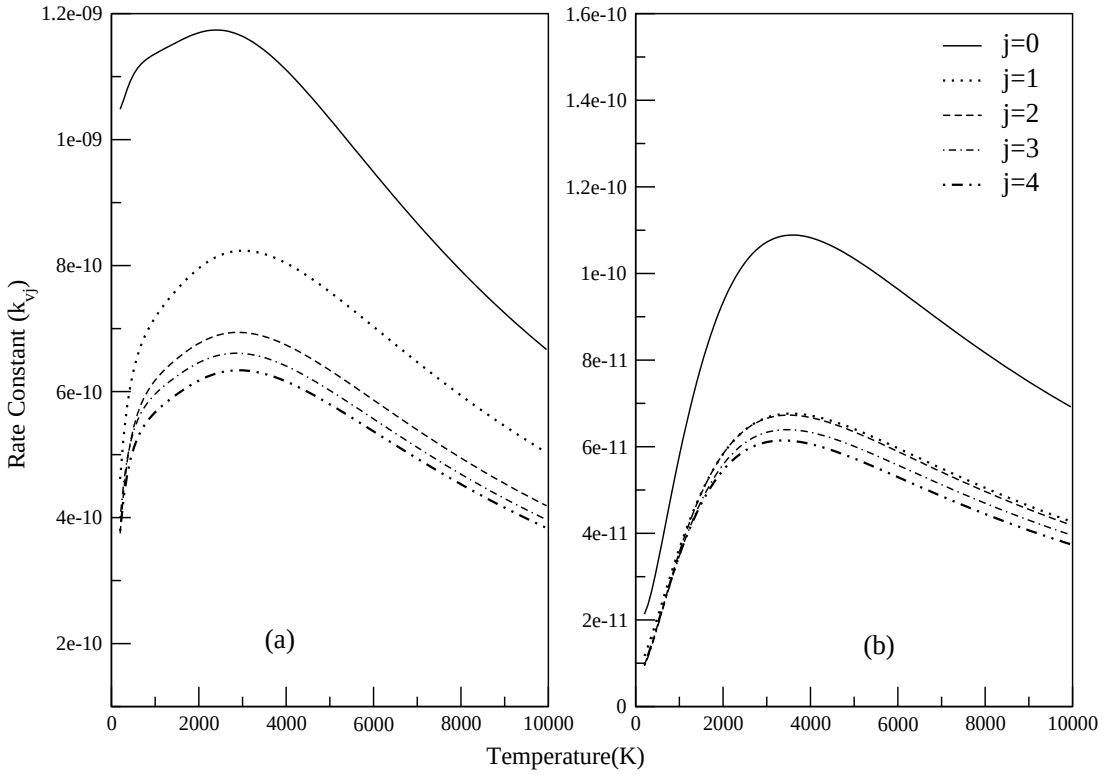

Figure 4.4: Initial state selected thermal rate constants of the LiH^+ depletion and H-exchange channels of the H + LiH^+ (v = 0,j) reaction are shown in panel a and panel b, respectively. The rate constant curve for different j values are identified by different line types and indicated in panel b.

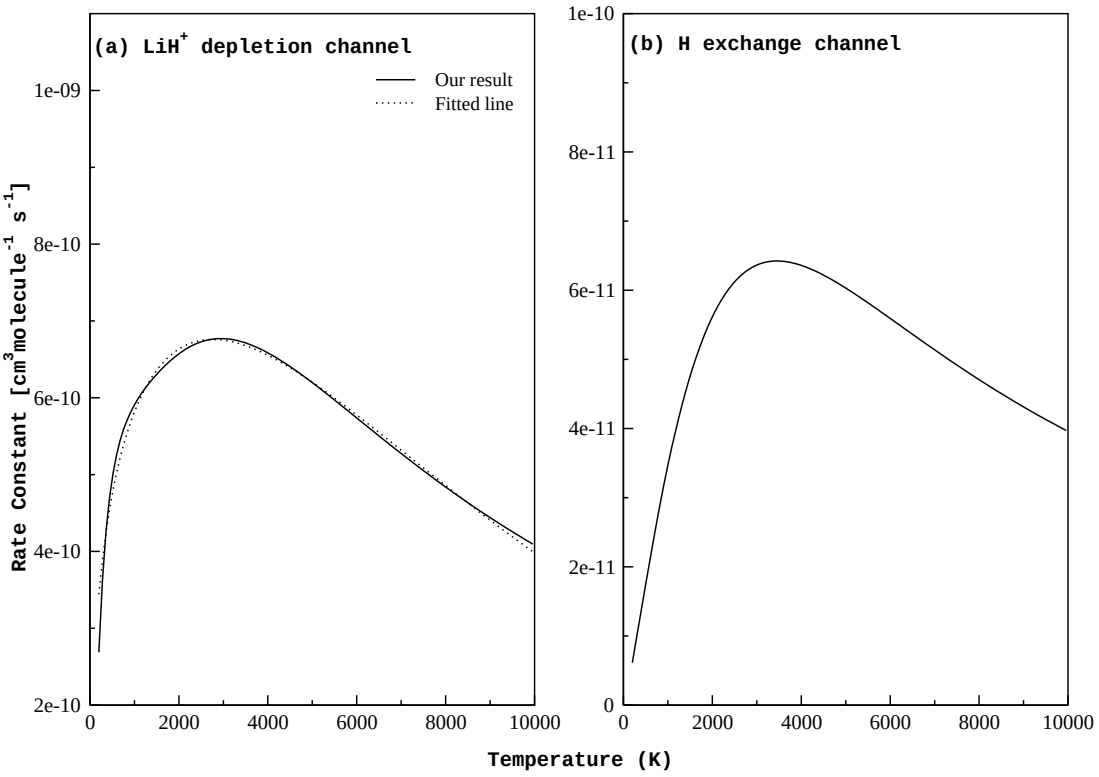

Figure 4.5: Boltzmann averaged (over j=0,4) thermal rate constants for the H + LiH^+ reaction. The rate constant for the depletion channel is fitted to the empirical formula proposed by Stancil *et al.* [14] and shown as dotted line in panel a (see text for details).

rates are higher than the exchange rates for any given temperature.

The depletion rate constants for the reagent LiH^+ are fitted to the functional form, $k(T) = a_1 \left(\frac{T}{300}\right)^{a_2} exp\left(-\frac{T}{a_3}\right)$ as proposed by Stancil *et al.* [14] in their kinetic model of primordial lithium reaction. Rate constant values obtained from the fit are included in panel a of figure 4.5 and shown as dotted lines. We obtained values a_1=4.16106×10^{-10}cm^{3}s^{-1}, a_2=0.397502, a_3=6953.43 K as compared with the corresponding value a_1=3.0×10^{-10}cm^{3}s^{-1} estimated by Stancil *et al.* [14].

4.3 Summary

Quantum dynamics of H + LiH^+ reaction is studied employing the *ab initio* PES developed by Martinazzo *et al.* [41]. A time dependent wave packet approach within the CS approximation is undertaken and state selected reaction probability, integral reaction cross section and thermal rate constant are reported. Effect of reagent rotational excitation is also discussed. Effort is made to minimize the contribution of low energy CID channel into the reactive dynamics. The prime observation of this study are follows

1. The LiH^+ depletion reaction is found to be more favoured over the H exchange path.

2. Rotational excitation of the reagent causes a demotion of reactivity for both LiH^+ depletion and H-exchange processes.

3. The LiH^+ molecule is destroyed by collision with H and this LiH^+ depletion processes proceed through a fairly high rate.

Chapter 5

H + LiH collision dynamics at ultracold temperature conditions

5.1 Introduction

Interaction of atoms and molecules at low collision energy has drawn considerable attention of researchers in chemical reaction dynamics during the past several years [89, 99–128]. In fact, with the emergence of modern techniques it is now possible to study the molecular interactions and chemical reactions, experimentally, at mili Kelvin temperature range [99–101]. In such situations the dynamics is solely controlled by quantum effects and any tiny perturbation can influence the scattering processes resulting changes in the dynamical outcome. In this ultracold temperature conditions, the de Broglie wavelength associated with the colliding particles is extremely large and the long-range part of the interaction potential play the crucial role in the dynamics. In such exotic temperature conditions the internal energy of the reactants is the driving force for the reaction to proceed. Because of the slow movement of the reagents they interact with

each other for a sufficiently long time which leads to an efficient transfer of energy among reagents and products. In fact, the dynamics at ultracold conditions is constrained by the internal energy and the internal angular momentum conversion effect. It is found that quasi-resonant vibration-rotation (QRVR) transfers in atom-diatom systems [102] and quasi-resonant rotation-rotation (QRRR) transfers and quasi-resonant vibration-vibration (QRVV) transfers in molecule-molecule systems [103–106] occur with high efficiency at ultracold temperature regime. It was found that the cross section and rate of elastic, inelastic and reactive collisions are by and large insensitive to the finer details of the interaction potentials and follow the Wigner threshold law in the limit of zero collision energy [88].

In this chapter, the H + LiH collision dynamics on the electronic ground PES constructed by Wernli *et al.* [35] is studied, at cold and ultracold temperature condition by utilizing the 'ABC quantum scattering program' of Skouteris *et al.* [55]. The lowest and highest collision energy considered here are 10^{-9} eV and 0.01 eV, respectively. Initial state selected probability as well as state-to-state probability, integral cross section and rate constant are calculated for the various mechanistic paths of the H + LiH collision processes. The effect of reagent vibrational excitation at this exotic temperature condition is also discussed along with a comparison with the same studied at thermal conditions (*cf.* Chapter 3).

The possible scattering path for the H + LiH reaction on its electronic ground state includes R1, R2, NR processes [page 11]. This NR and R2 channels lead to the same product diatom (LiH) and in the present quantum mechanical calculations they can not be distinguished clearly rather they are collectively attributed to two processes - elastic and inelastic.

Therefore, the H + LiH collision dynamics is studied here for the following three mechanistic pathways:

1. H + LiH(v j) → Li + H_2(v' j') (LiH depletion)

2. H + LiH(v j) → H + LiH(v j) (Elastic collisions)

3. H + LiH(v j) → H + LiH(v' j') (Inelastic collisions).

At this point it is noteworthy that special care must be taken to study the dynamics at ultracold temperature conditions. The interaction potential at the asymptomatic region of the PES must be negligibly small compared to the collisional energy, which itself is very small. Hence any tiny contribution from the long range part of the interaction potential can not be ignored in the ultracold condition.

5.2 Results and discussion

To calculate the dynamical observables by using 'ABC program' one needs to ensure the convergence of the various numerical parameters involved in the calculations. Extensive test calculations are performed to obtain the convergence in this study. The maximum value of the internal energy (E_{max}) and the maximum value of the diatomic rotational quantum number (j_{max}) controls the size of the basis set. At a collision energy $\sim 10^{-9}$ eV, convergence is achieved for the state-to-state probability within 1% by using $E_{max} = 2.0$ eV and $j_{max} = 25$. For collision energies higher than 10^{-4} eV, convergence is achieved for a maximum hyper radius, $\rho_{max} = 50\ a_0$ and integration step size $\Delta\rho = 0.01\ a_0$. However, for collision energies below 10^{-4} eV increasingly large ρ_{max} values were required for

the convergence. At this point we mention that reactive and inelastic components converge much rapidly than elastic component and the convergence of the elastic component turns out to be computationally very expensive. It is found that for collision energies of $\sim 10^{-9}$ eV, $\rho_{max} = 227\ a_0$ and $\Delta\rho = 0.005\ a_0$ are required to obtain converged results. These lead to a convergence of the elastic component within a deviation of $\sim 5\%$. The basis set corresponding to these parameters involves 925 rovibrational functions.

Initial state selected energy dependent total probabilities of the reactive (LiH depletion), elastic and inelastic processes for the H + LiH (v = 0 - 1, j = 0) scattering at total angular momentum J = 0, calculated by using the TIQM framework described in chapter 2 are presented in figure 5.1. Here the reactive, elastic and inelastic probabilities are shown by black, blue and red colour lines, respectively. The solid and dotted lines represent the probabilities for the initial vibrational state (v) as 0 and 1, respectively. From figure 5.1, it is clearly seen that the dynamics at ultracold conditions for the H + LiH(v = 0-1, j = 0) collisions is dominated by the elastic collision processes. It can also be seen from this figure that with increasing collision energy the elastic collision probability decreases whereas, the reactive and inelastic (for v = 1) collision probability increases and becomes dominant at thermal conditions. The inelastic process for the H + LiH(v = 0,j = 0) collision is purely endothermic and hence, do not occur at ultracold conditions. This inelastic channel is found to open only beyond the collision energy $\sim$ 0.0018 eV. This is because the minimum energy required to rotationally excite the reagent (from v = 0,j = 0 to v = 0,j = 1 level of LiH) is $\sim$ 0.0018 eV. This type of constraint in energy conservation is absent for the inelastic processes to occur in case of H + LiH(v = 1,j = 0) scattering as the lower vibrational level (v

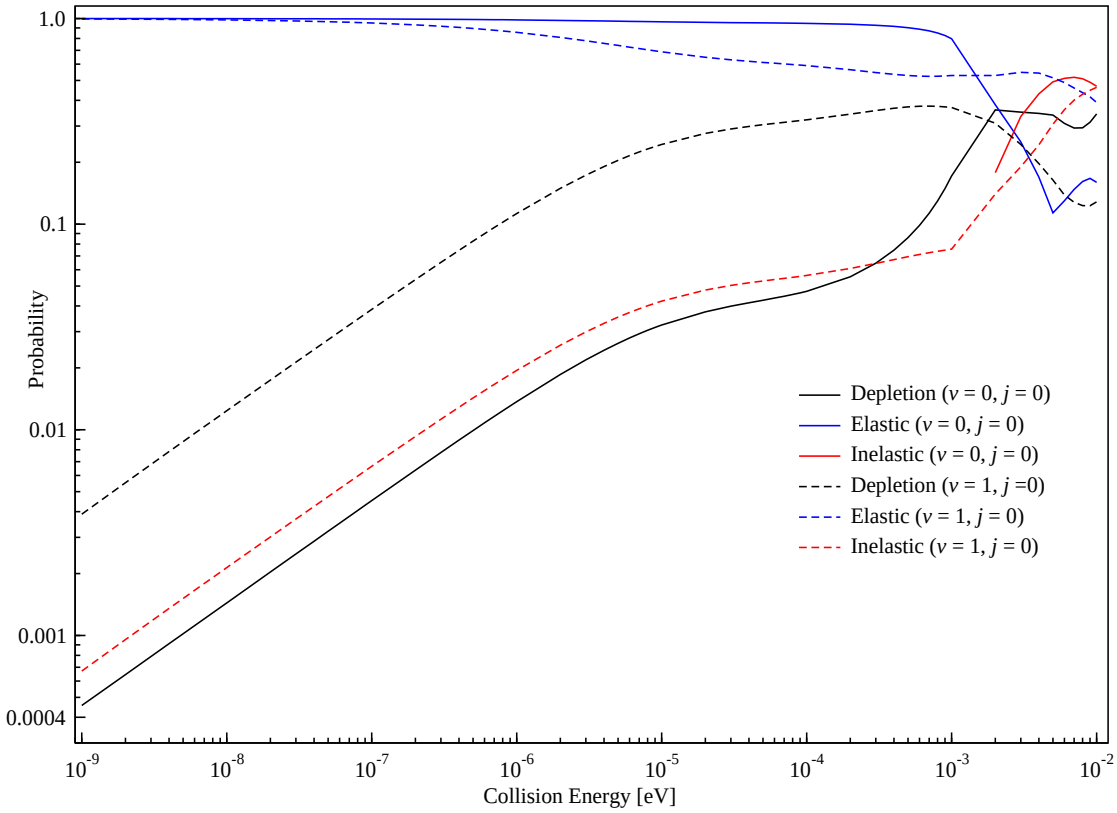

Figure 5.1: Initial state-selected probabilities for the H + LiH(v = 0 - 1, j = 0) collisions for J = 0. The probabilities of the LiH depletion and elastic and inelastic components of LiH retention channels are shown in the figure by black, blue and red lines, respectively. The initial vibrational state of the reagent LiH is distinguished by solid (for v = 0) and dashed (for v = 1) lines.

= 0) is energetically accessible for this case. The H + LiH($v = 1$,$j = 0$) scattering leads to a vibrationally cold LiH molecule at low collision energy via inelastic collision processes. It is also seen from the figure 5.1 that elastic probability decreases a little with vibrational excitation of the reagent LiH from $v = 0$ to $v =$ 1 state at ultracold conditions. Contrary to the observation at thermal conditions [presented in chapter 3, page 52], the LiH depletion probability is found to increase with vibrational excitation of the reagent at ultracold conditions. It can also be seen from the figure 5.1 that at relatively higher collisional energy ($\sim$ 0.0017 eV), which is in the thermal range, the vibrational excitation causes a diminution of reactivity. The enhanced reactivity with reagent vibrational excitation may be attributed to the fact that the excitation of reagent vibration increases the number of accessible product states and the slowly moving reagent can therefore efficiently move into the product channel. With increasing collision energy, the velocity of the reagent increases. In such conditions the presence of late barrier in the PES (which is absent in this system) enhances the reactivity [96].

Vibrational and rotational populations of the product H_2 molecule formed *via* LiH($v = 0$-1, $j = 0$) depletion path at the collision energy of 10^{-9} eV and 0.01 eV are presented in figure 5.2 to figure 5.5. State-to-state probabilities of the H + LiH($v = 0$, $j = 0$) depletion reaction, calculated at the collision energy of 10^{-9} eV and 0.01 eV, are shown in figure 5.2(a-b) and figure 5.3(a-b), respectively, whereas, the same for the H + LiH($v = 1$, $j = 0$) are plotted in figure 5.4(a-b) and figure 5.5(a-b), respectively. In these figures, the vibrational populations are shown in panel (a) and the rotational populations in each of the energetically open vibrational levels of product H_2 are presented in panel (b). It can be seen from figure 5.2(a), that even at collision energy as low as 10^{-9} eV the yield of the

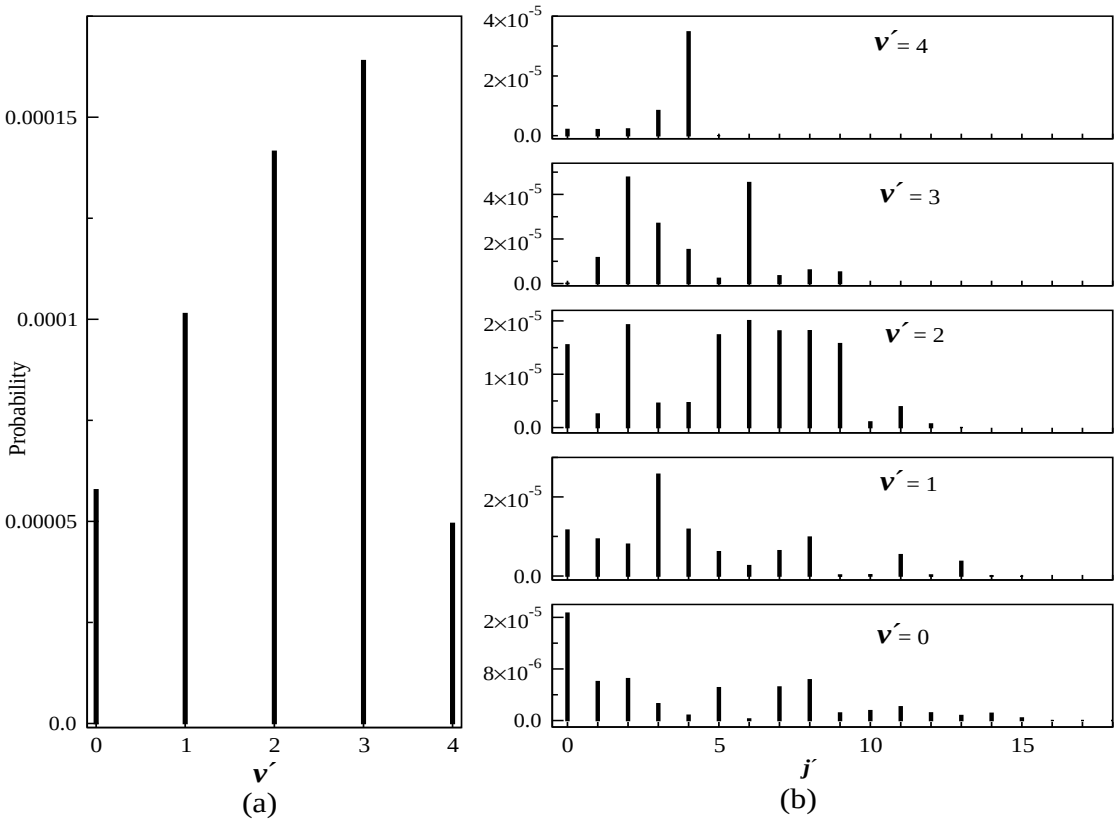

Figure 5.2: State-to-state probability of H + LiH($v = 0,\ j = 0$) $\longrightarrow$ Li + H_2 (v', j') reaction at a collision energy 10^{-9} eV. The product vibrational and rotational excitations are shown in panel a and b, respectively.

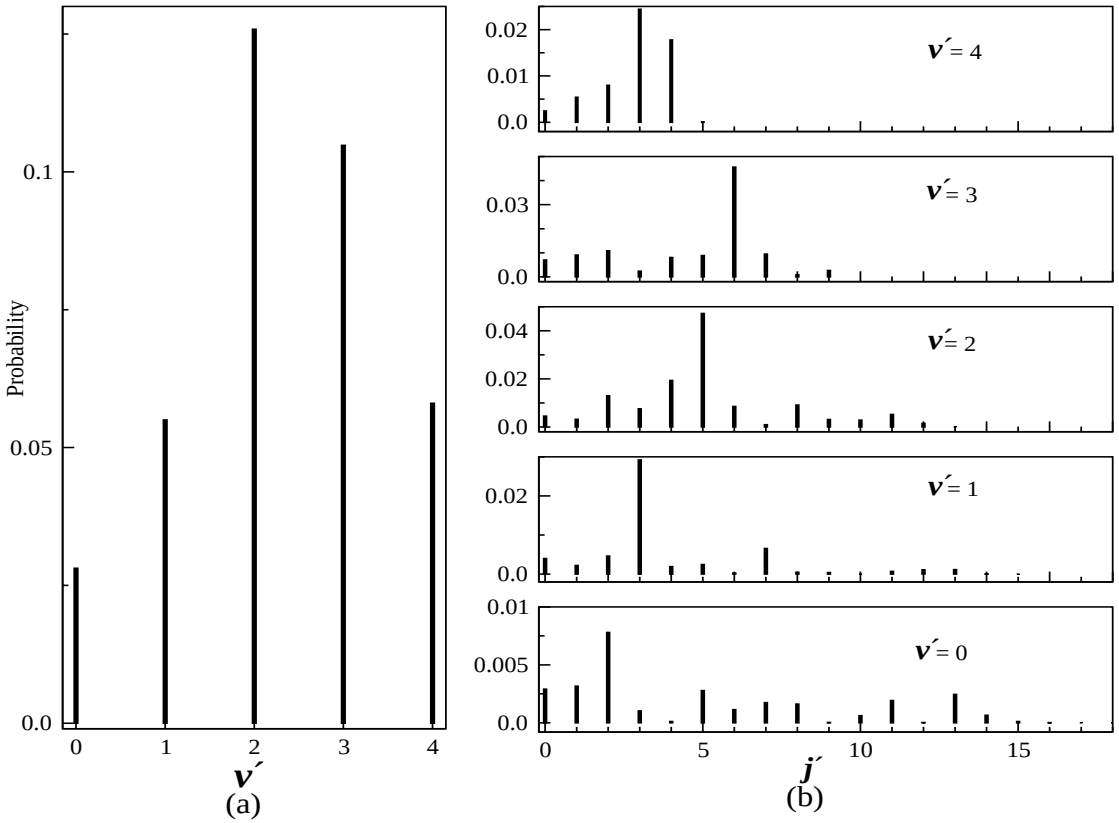

Figure 5.3: Same as figure 5.2, at a collision energy 0.01 eV.

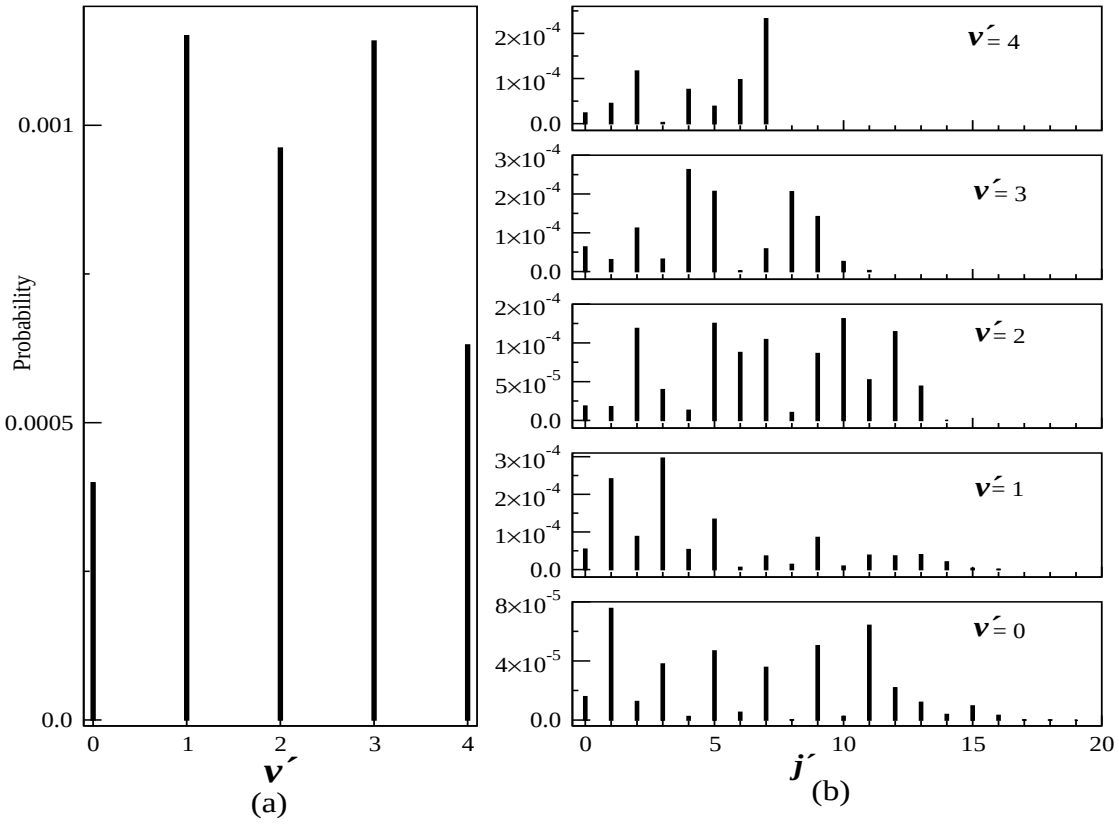

Figure 5.4: Vibrationally (panel a) and rotationally (panel b) resolved reaction probability for the H + LiH ($v = 0$, $j = 0$) $\longrightarrow$ Li + $H_2(v', j')$ reaction at a collision energy 10^{-9} eV.

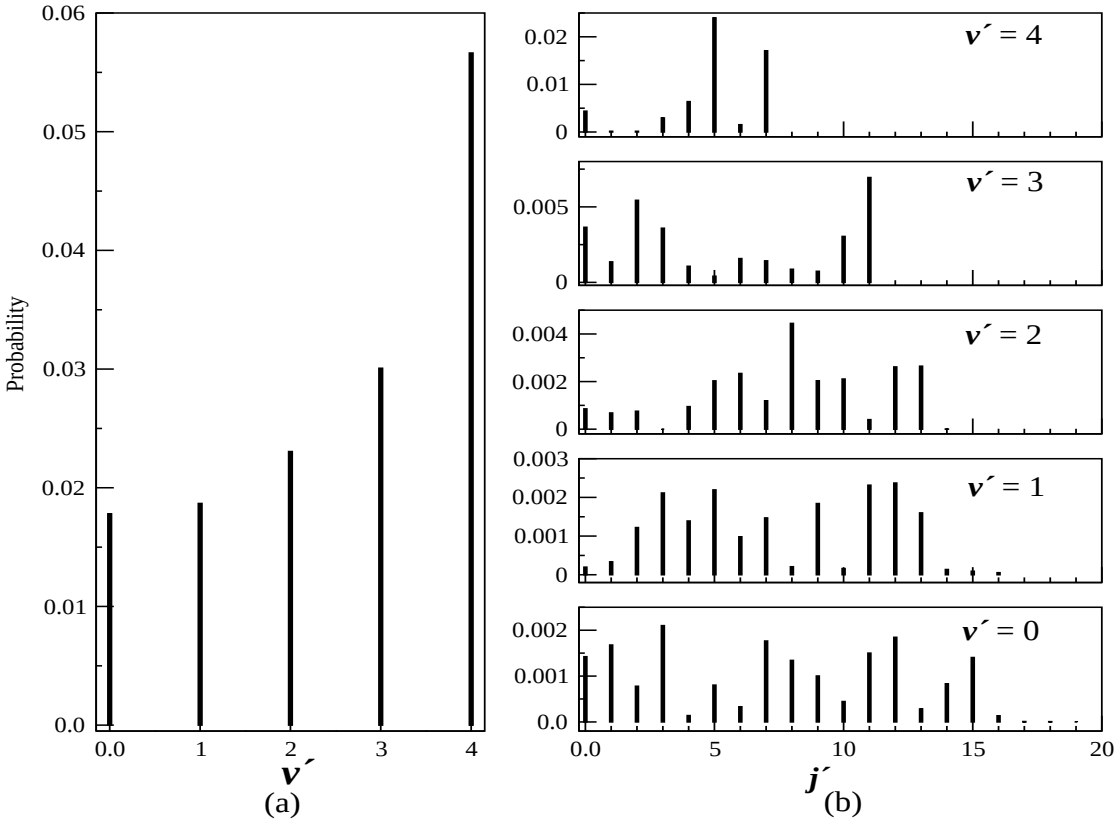

Figure 5.5: Same as figure 5.4 but at the collision energy 0.01 eV.

product H_2 molecules in excited vibrational levels is significant. The population of H_2 molecules is predominant in the $v' = 3$ vibrational level. Formation of vibrationally and rotationally hot H_2, reduces the energy gap between reactant and product. Thus exothermicity of the reaction is partially utilised to excite the product ro-vibrational levels.

From panel b of figure 5.2, it can be seen that a wide range of rotational levels of H_2 are populated at this ultracold conditions. Formation of H_2 at various rotationally excited levels are determined by the anisotropic interaction between

H and LiH along with a competition between rotational angular momentum and internal energy. Conservation of internal energy requires the product to be formed in a rotational level which has the internal energy closest to that of reactants. This means, for an exothermic reaction, like the one studied here, conservation of internal energy leads to the formation of rotationally hot product. This causes a large deviation of energy due to orbital angular momentum. On the other hand, conservation of orbital angular momentum requires the product to be formed in the same rotational level as that of reactant. A compromise between the two factors cause the maximum population of H_2 at modest rotationally excited level at 10^{-9} eV collision energy for the H + LiH ($v = 0$, $j = 0$) reaction.

The pattern of ro-vibrational distribution of product is qualitatively different for the reagent in the $v = 1$ level compared to $v = 0$ level. Vibrational excitation of the reagent (LiH) increases the exothermicity of the reactions and also increases the number of energetically accessible ro-vibrational product channels for the reagents to transform to product. From figure 5.4(a), it can be see that the H_2 molecules are forming in the vibrational levels $v' = 0$ - 4, with dominant population in the $v' = 1$ and $v' = 3$. It can also be seen from figure 5.4(b) that the tendency to form rotationally hot H_2 is relatively more for reagent at $v = 1$ level than the reagent at $v = 0$ level.

The initial state selected elastic, inelastic and reactive (LiH depletion) cross-sections and non thermal rates for the H + LiH($v = 0$ - $1, j = 0$) collisions for the total angular momentum $J = 0$ are plotted as a function of collision energy in figure 5.6(a) and 5.6(b), respectively. Similar to figure 5.1 the LiH depletion, elastic and inelastic processes are identified by black, blue and red colour lines, respectively, and the reagent vibrational states 0 and 1 are distinguished by solid

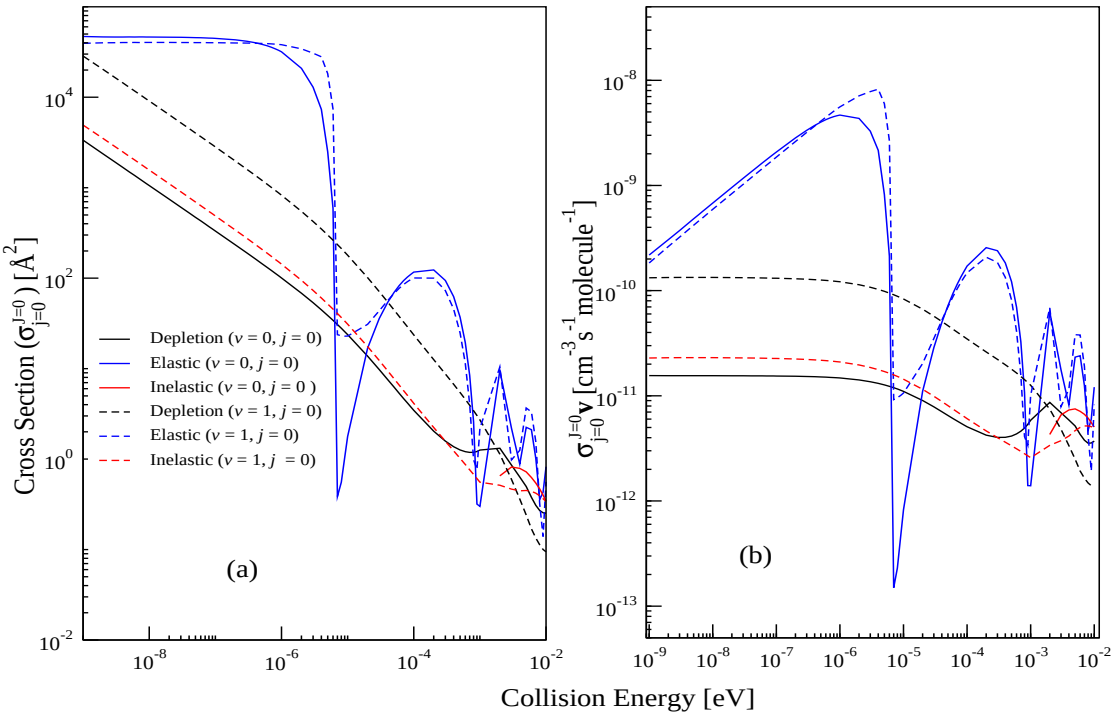

Figure 5.6: The initial state-selected energy dependent cross sections (panel a) and rate constant (panel b) for the elastic, inelastic and LiH depletion process for H + LiH (v = 0 - 1, j = 0) collisions at the total angular momentum J = 0.

Table 5.1: The value of the real part (α) and imaginary part (β) of the scattering length for the initial vibration level $v = 0$ and 1 for H + LiH(v,$j = 0$) scattering.

v	α (Å)	β (Å)
0	-0.68	49.57
1	-0.19	47.87

and dashes line types, respectively. The $J = 0$ cross sections are calculated by using the equations 2.47(a-c) [see page 40]. The non-thermal rate constants are then obtained by multiplying the $J = 0$ cross sections by the magnitude of velocity of the reagents. From figure 5.6(a-b), it can be seen that the Wigner threshold starts at $\sim 10^{-7}$ eV. Below this energy elastic cross section as well as reactive and inelastic rate become invariant with collision energy. It can also be seen from the figure 5.6 that the energy dependent cross sections for inelastic (for $v = 1$) and reactive processes vary linearly in the logarithmic scale with a slope of, $-\frac{1}{2}$ Å^2/eV. Here it is noteworthy that for any vibrational level (v) of the reagent with $j = 0$ and total angular momentum $J = 0$, one always have $l = 0$. This means, for $j = J = 0$, the collision leads to purely s-wave scattering. For the s-wave scattering the inelastic and reactive cross section varies as inverse square root of collision energy whereas rate of the elastic process changes as the square root of energy [88].

The scattering lengths of the H + LiH($v = 0$ - 1, $j = 0$) collisions are calculated by using the relations 2.51(a-b) and are presented in table 5.1. A negative value of α is obtained for both $v = 0$ and 1 reactant states. This indicates nonexistence of bound or quasi bound state near the threshold as the the existence of bound or quasi bound state near the threshold leads to a large positive value of α [26].

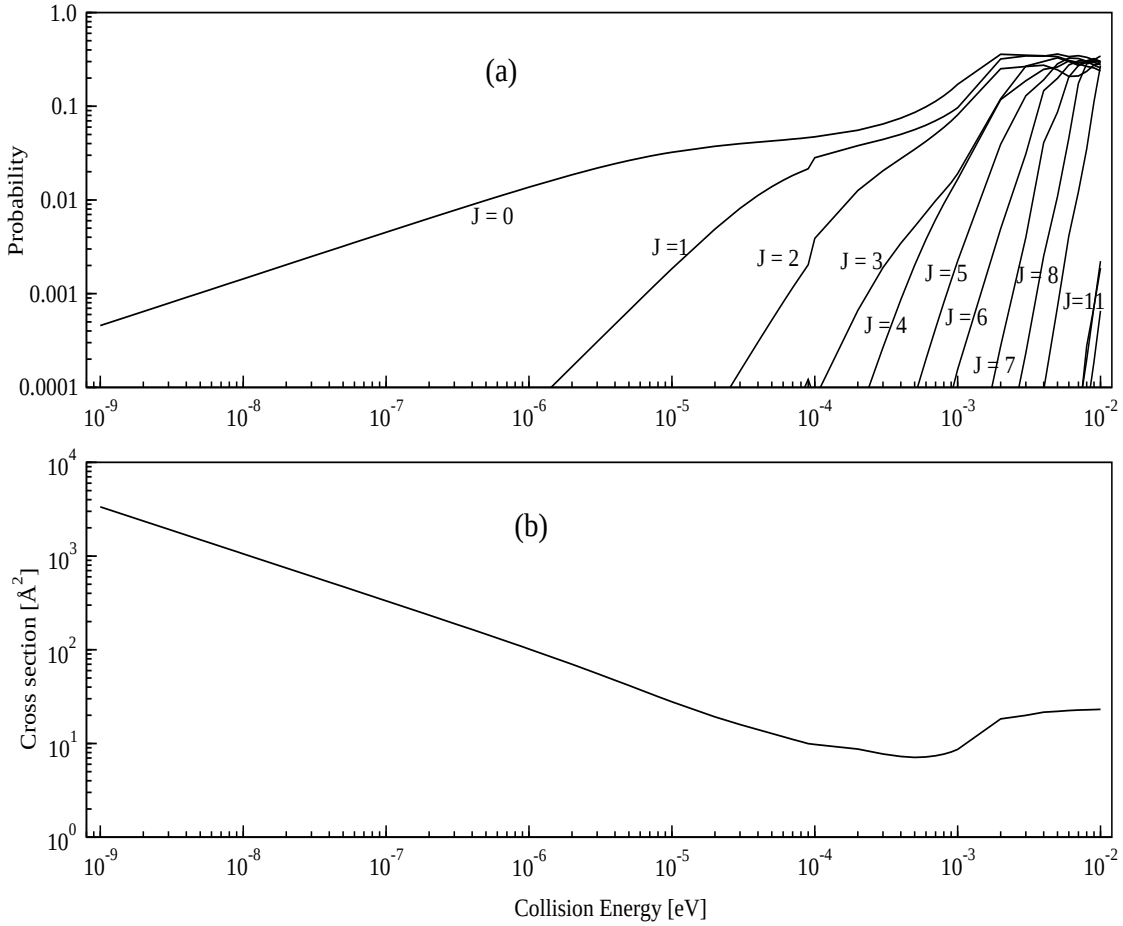

Figure 5.7: The effect of total angular momentum J on the probability of H + LiH(v =0, j=0) → Li + H_2 process (panel a). The initial state selected LiH depletion cross section, calculated by considering the contribution from partial waves J upto 16, is shown in panel b.

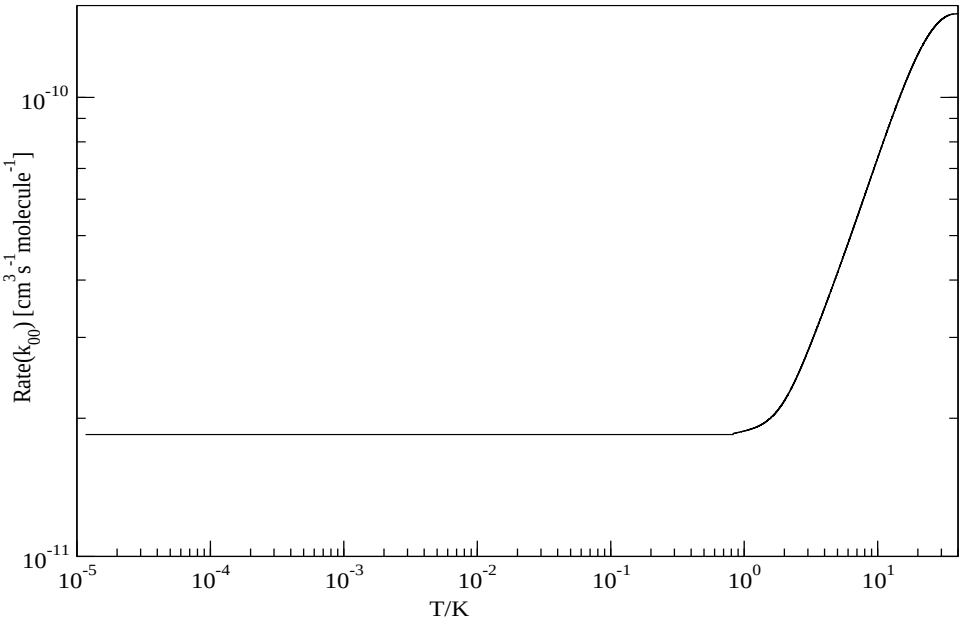

Figure 5.8: Initial state selected rate constant for the H + LiH (v =0, j=0) $\rightarrow$ Li + H_2 reaction plotted as a function of temperature in a logarithmic scale. The rate is found to have a constant value of $\sim 1.84 \times 10^{-11}$ cm^{3}s^{-1}molecule^{-1} below $\sim$ 1.0 K.

The energy dependent probability of LiH depletion processes for $J > 0$ is calculated for the H + LiH(v= 0, j=0) collision and are shown in figure 5.7(a). The probability curve develops a barrier with increasing J originating from the increase in angular momentum barrier. It can also be seen that at ultracold conditions only $J = 0$ partial wave contributes to the dynamics of H + LiH(v= 0, j=0) collision. These findings confirms that s-wave scattering is the only mechanism at ultracold conditions.

The initial state selected integral cross section is then calculated by averaging all the partial wave contributions necessary within the calculated range of collision energy and is shown in figure 5.7(b). It is found that consideration of partial wave contributions upto $J = 16$ is sufficient for the present calculation. As expected,

the integral cross section is found to follow the Wigner law in the lower part of the energy diagram where only s-wave contributes, and the slope of cross section *vs.* collision energy curve is $-\frac{1}{2}$ Å^2/eV.

The initial state selected thermal rate constant for the reactive processes of the H + LiH($v = 0$,$j = 0$) collision is then calculated with the aid of equation 2.54 and by utilizing the cross section data presented above. The results are shown in figure 5.8 in a logarithmic scale. Below $\sim$ 1.0 K temperature, the rate constant becomes invariant with temperature. At the low temperature LiH($v = 0$,$j = 0$) depletes with a rate of $\sim 1.84 \times 10^{-11}$ cm^{-3}s^{-1}molecule^{-1} in collision with H.

5.3 Summary and outlook

H + LiH($v = 0$ -1,$j = 0$) collision dynamics is studied at the cold and ultracold temperature conditions by utilizing the 'ABC reactive scattering programme' [55]. The collision dynamics is examined here within the collision energy range of 10^{-9} eV to 0.01 eV. The probability, integral cross section and energy dependent rate constant of the elastic, inelastic and reactive (LiH depletion) processes are reported for s-wave scattering ($J = 0$). The initial state-selected reaction cross sections and thermal rate constants are also calculated for the reactive LiH depletion path by including the partial wave contribution for total angular momentum upto $J = 16$. The major findings of this chapter are the following.

1. Contrary to the observation at thermal conditions, the LiH depletion process is dominated by elastic collision.

2. Vibrational excitation of the reagent increases the depletion probability. The reverse effect was observed at thermal conditions.

3. Vibrationally and rotationally excited H_2 are found to form through the LiH depletion processes. Even at the lowest collision energy of 10^{-9} eV rotationally hot product (H_2) forms. Population of product H_2 at higher rotational levels, as large as $j' = 17$ with $v' = 0$, was observed.

4. The real part of the scattering length has a small negative value. This indicates the absence of any bound or quasi bound state near threshold.

Chapter 6

H + LiH^+ collision dynamics at ultracold temperature conditions

6.1 Introduction

In this chapter we attempt to understand the H + $LiH^+(v = 0, j)$ collision dynamics at the cold and ultracold temperature conditions on its electronic ground PES [41], employing a time-independent quantum mechanical methodology as implemented in the ABC scattering program module by Skouteries *et al.* [55]. State-to-state probability, integral cross section and energy dependent rate constant (for s-wave scattering) for the LiH^+ depletion/retention processes are calculated. Integral cross sections and thermal rates are also reported for the LiH^+ depletion channel by including the contributions of all partial waves of the total angular momentum upto $J = 18$. Large vibrational and rotational excitation of the product H_2 molecules *via* LiH^+ depletion path is found at the lowest collision energy of 10^{-9} eV considered in this work. At such low energies validity of Wigner threshold law [88] in the collision dynamics is also established. The prob-

able paths for the H + LiH^+ scattering on its electronic ground state includes R1, R2, NR and CID processes [page 14]. But, at the cold temperature conditions, the contribution of the CID channel is insignificant because of the unavailability of sufficient energy necessary for three body dissociation. Now, the NR and R2 channels can be distinguished, in principle, based on the arrangement of the nuclei, but in some sense these two channels are identical as they leads to the same products and in this quantum mechanical calculations they can not be cleanly separated. These two channels collectively yield the LiH^+ retention probability and are associated with two processes - elastic and inelastic.

Therefore, in this study of the H + LiH^+ collision dynamics we focus on the following processes:

1. $H + LiH^+(v\ j) \rightarrow H_2(v'\ j') + Li^+$ (LiH^+ depletion)
2. $H + LiH^+(v\ j) \rightarrow H + LiH^+(v\ j)$ (Elastic collisions)
3. $H + LiH^+(v\ j) \rightarrow H + LiH^+(v'\ j')$ (Inelastic collisions)

In order to ensure the convergence of the results with respect to various parameters for the total angular momentum $J = 0$, extensive test calculations are carried out. As state-to-state probabilities, cross sections and rates are of primary interest in the present study we tried to optimize the individual S-matrix elements. For collision energies higher than 10^{-4} eV, convergence is achieved for a maximum hyper radius, $\rho_{max} = 50\ a_0$ and integration step size $\Delta\rho = 0.01\ a_0$. However, for collision energies below 10^{-4} eV increasingly large ρ_{max} values are required for the convergence of the results and it turns out to be computationally very expensive. We find that for collision energies of $\sim 10^{-9}$ eV, $\rho_{max} = 300\ a_0$ and $\Delta\rho = 0.001\ a_0$ are required to obtain converged results. The maximum value

of the internal energy in any channel also plays important role in the convergence behaviour. We find that, E_{max} = 0.13 eV yields the best converged results. This E_{max} value is very close to the LiH^+ dissociation energy (D_e), of $\sim$ 0.13869 eV [47]. The use of E_{max} = 0.13 eV opens up 31 rotational channels and all of them are included in the present calculations. Considering all three paths (R1, R2 and NR) a total of 384 channels are included altogether in the calculations in order to obtain converged results.

6.2 Results and discussion

The total probabilities [calculated using Eq. 2.45] of reactive, elastic and inelastic scattering as a function of collision energy of the H + LiH^+ (v = 0, j = 0) collisional system for J = 0 are presented in figure 6.1 and distinguished by different line types indicated in the panel. It is interesting to note from figure 6.1 that the elastic collision probability (leading to LiH^+ retention) dominates at the ultracold temperature regime. However, with increasing collision energy the LiH^+ depletion probability increases and becomes the dominant event at cold and thermal conditions. It can be seen from figure 6.1 that the inelastic channel leading to internally excited LiH^+ remains closed at the ultracold temperature conditions. The sum of the three probabilities presented in figure 6.1 at cold and ultracold temperatures equals to $\sim$ 1.0. This unitarity reveals that the CID channel that dominates at the thermal condition (as discussed in chapter 4) remains closed at the cold and ultracold conditions. This is expected result as in the limit of zero collision energy the contribution from the CID process should be vanishingly small.

In order to assess the contribution of the open vibrational and rotational levels of the product molecules to the reactive $LiH^+(v = 0, j = 0)$ depletion probability presented in figure 6.1, state-to-state probability values of the $LiH^+(v = 0, j = 0)$ depletion reaction are plotted in figure 6.2(a-b) and figure 6.3(a-b) calculated at the collision energy of 10^{-9} eV and 0.01 eV, respectively. In figure 6.2 contribution to the probability from vibrationally and rotationally (within a given vibrational level) excited product H_2 is shown in panel a and b, respectively. It can be seen from panel a that the most efficient energy transfer occurs to the $v' = 9$ vibrational level of H_2. The excitation to the energy levels lower than $v' = 3$ and higher than $v' = 12$ is minimal. A possible explanation of this observation can perhaps be given based on energetic considerations in the following way.

The LiH^+ depletion path is collinearly dominated as obvious from the topography of the PES shown in Ref. [47]. The reaction exoergicity is ~ 4.36 eV along this path. The H_2 molecule supports about fifteen bound vibrational levels on this PES (the reference zero of energy on the PES is considered to be the asymptotically separated H + LiH^+ reagents) [47]. The reagents (H + LiH^+) quickly slide down the steep depletion path and cling in the shallow potential well at ultracold temperature conditions. The large exoergicity released is efficiently transferred to the product vibration in this situation. It can be seen from panel b of figure 6.2 that rotationally hot H_2 molecules are produced for the lower vibrational excitation in the limit of zero collision energy. This result is in perfect accord with the conservation of total energy during the entire collision event. Comparison of results of figure 6.2(a-b) with those obtained at the highest collision energy of 0.01 eV considered in this paper and presented in 6.3(a-b) reveals the following. The product vibrational and rotational distribution remains similar in the two

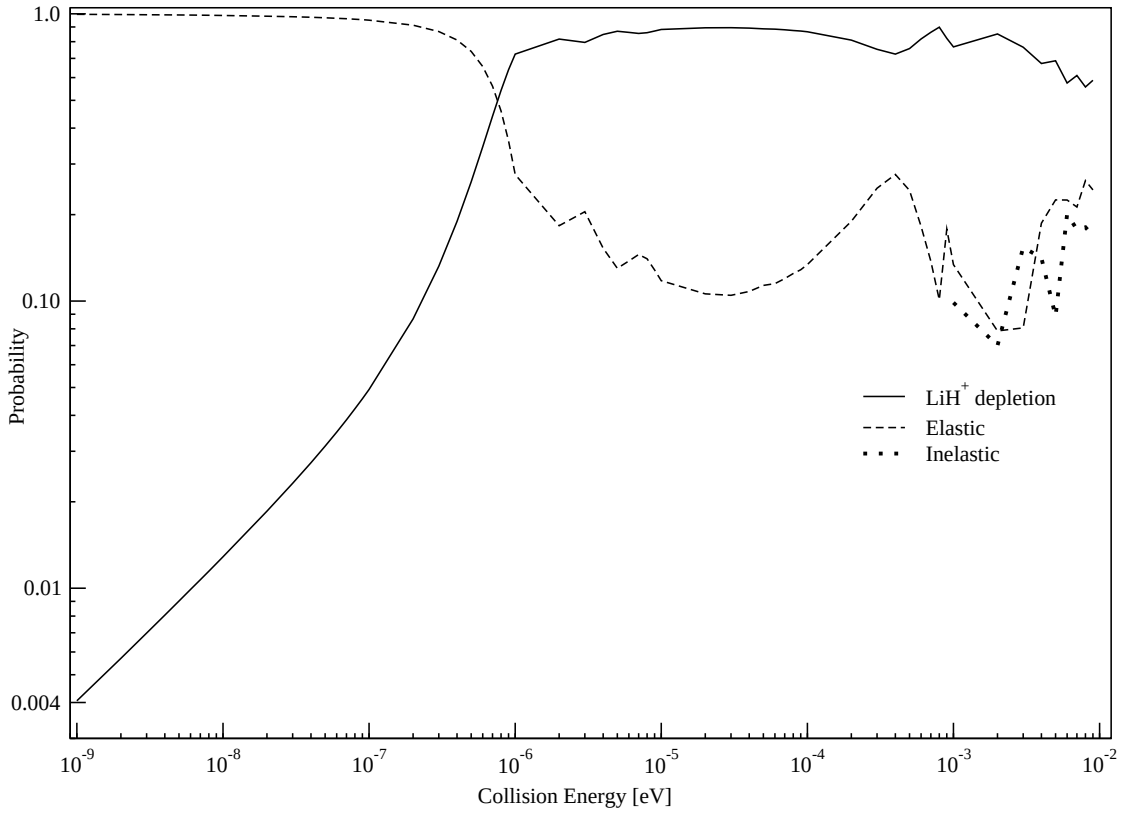

Figure 6.1: Initial state-selected probabilities (averaged over all open vibrational and rotational states of products at the given collision energy) of the H + LiH^+($v = 0$, $j = 0$) collisions for $J = 0$. The probabilities of the LiH^+ depletion and elastic and inelastic components of LiH^+ retention channels are shown in the figure by solid, dashed and dotted lines respectively.

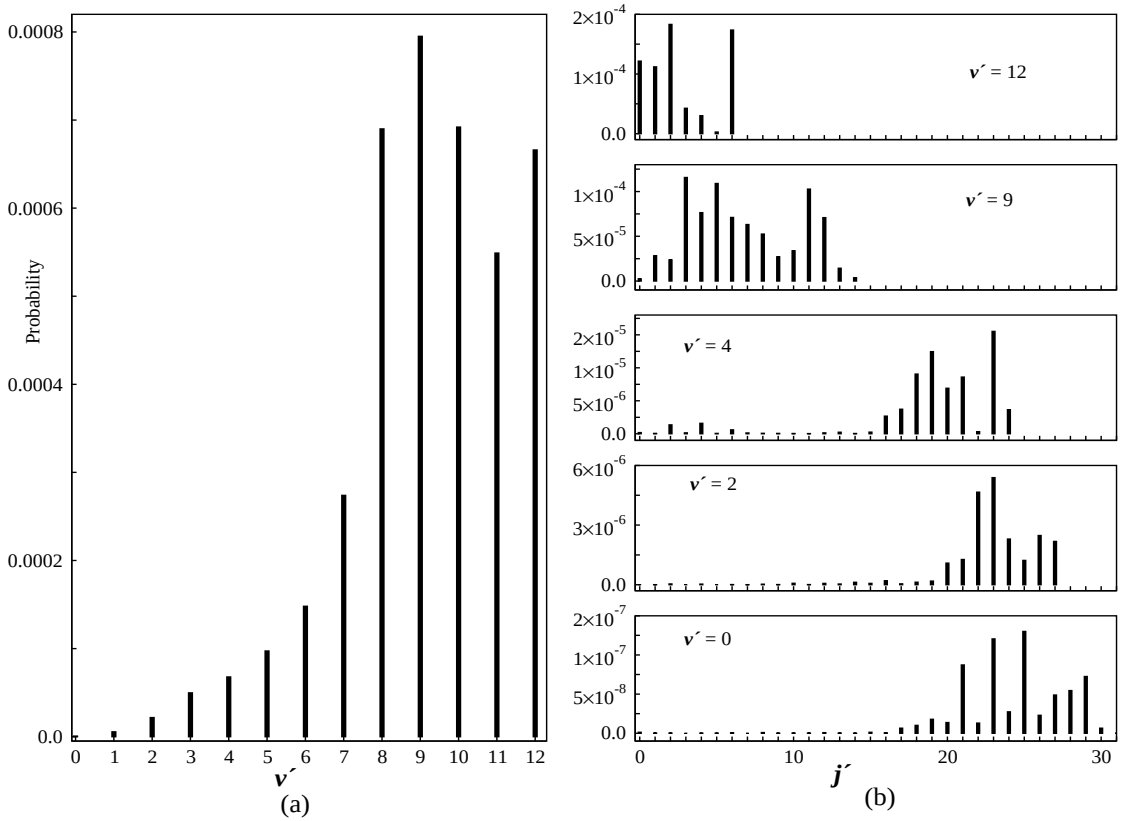

Figure 6.2: State-to-state probability of H + LiH^+ ($v = 0$, $j = 0$) $\longrightarrow$ Li^+ + H_2 (v', j') reaction at a collision energy 10^{-9} eV. The product vibrational and rotational excitations are shown in panel a and b, respectively.

cases. In the latter case the probability of excitation to the $v' = 12$ level of H_2 is maximum and both vibrational and rotational excitation probabilities are larger compared to those obtained at the lowest collision energy of 10^{-9} eV [*cf.* 6.2(a-b)]. This is in accordance with the results of figure 6.1, that the total reactive probability increases with increasing collision energy.

For the LiH^+ retention processes it is observed that the initial vibrational state of LiH^+ ($v = 0$) is not altered by collision with H within the observed collision

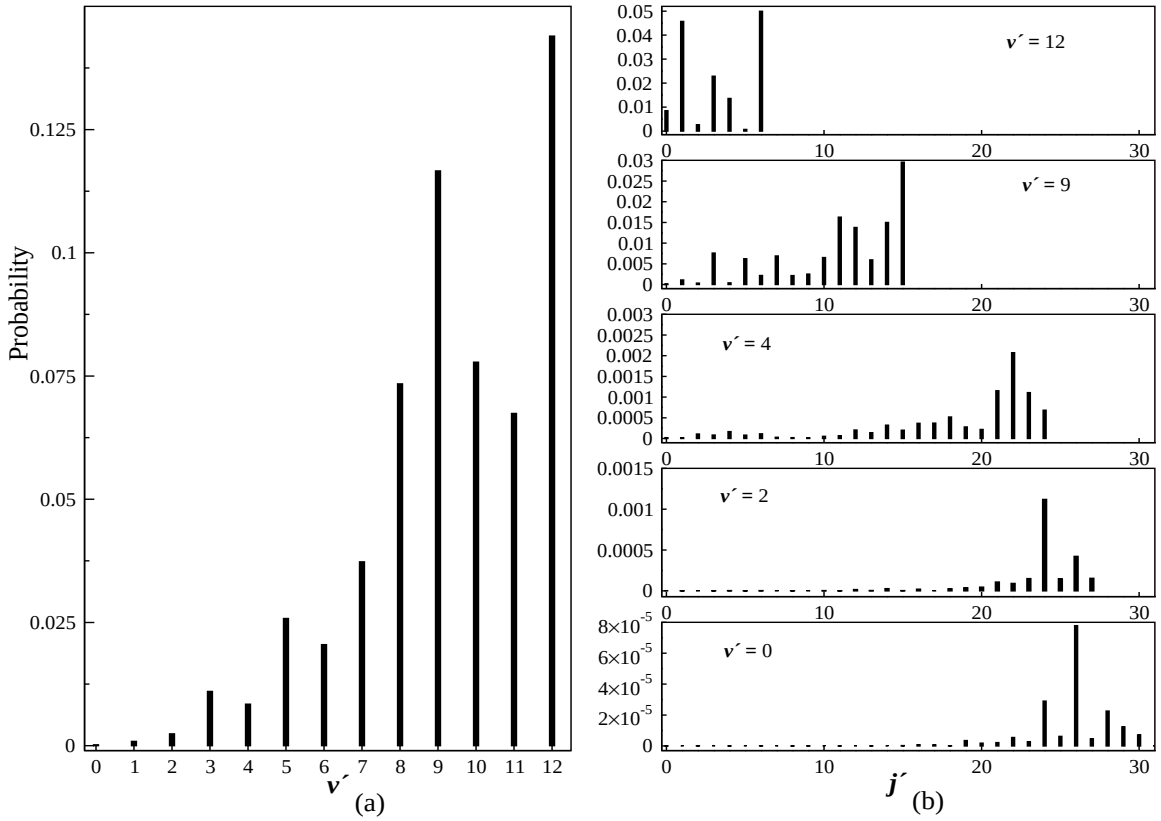

Figure 6.3: Same as figure 6.2 but at the collision energy 0.01 eV.

energy range. The rotational states of LiH^+ on the other hand alters. At very low collision energy only the ground, $j' = 0$, rotational level of product LiH^+ is populated and the collision is essentially elastic. With increasing collision energy the rotationally excited (upto $j' = 6$ within the calculated energy range) LiH^+ molecules are also formed. This is consistent with the results plotted in figure 6.1. It can be seen that the LiH^+ retention process is elastic at very low collision energies. In the limit of ultracold temperature conditions the available energy is inadequate for any further higher internal excitation of product LiH^+. It can be seen from figure 6.1 that the inelastic component of LiH^+ retention appears beyond $\sim 10^{-3}$ eV only.

The effect of rotational excitation of the reagent molecule on the depletion, elastic and inelastic probabilities in H + $LiH^+(v = 0, j)$ collision for $J = 0$ and for $J = j$ are shown in panel a, b and c of figure 6.4 and figure 6.5, respectively. It is noteworthy to mention at this point that for $J = 0$ and $j = 0$, the dynamics is purely governed by s-wave scattering. It can be seen from figure 6.4 that both the depletion and inelastic probability becomes vanishingly small for, $J = 0$, collisions at the ultracold temperatures with increase in the reagent rotational excitation. In such situations, the collision dynamics becomes purely elastic as can be seen from panel b of figure 6.4. The increase in the height of angular momentum barrier with rotational excitation primarily contributes to the decrease of the depletion and inelastic probabilities. As can be seen from figure 6.1 that the threshold of inelastic scattering occurs at higher collision energy for $LiH^+(j = 0)$. This threshold shifts to the lower collision energy with rotationally excited reagent [cf. figure 4(c)]. For LiH^+ $(j = 1)$ this threshold occurs below $\sim 10^{-7}$ eV collision energy. This is due to the availability of lower rotational states and

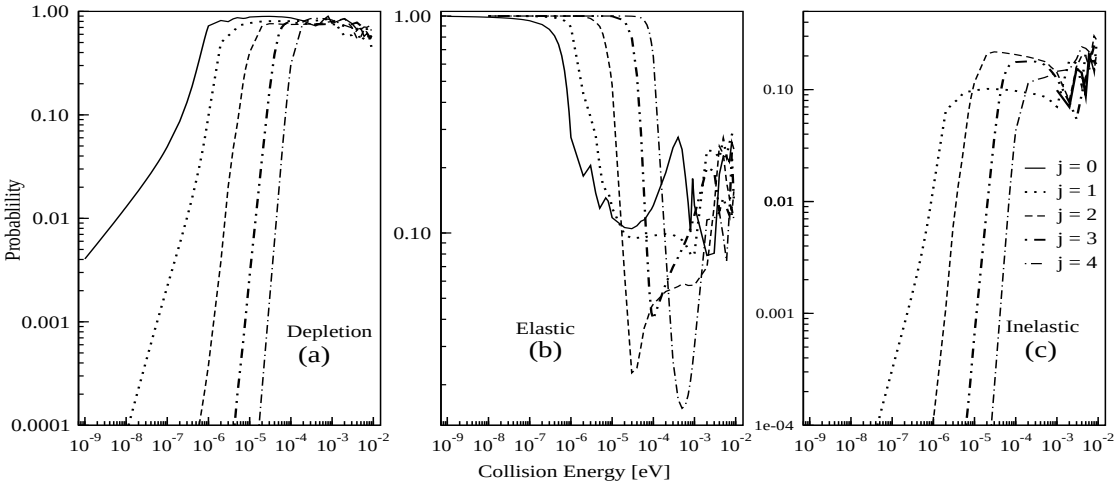

Figure 6.4: Initial state selected depletion, elastic and inelastic probabilities in H + $LiH^+(v = 0, j)$ collisions for $J = 0$ shown in panel a, b and c, respectively.

enough energy to populate them in such collisions.

The initial state selected reaction probability for $J = j$ are shown in figure 6.5. From figure 6.5, it is clear that both the depletion and inelastic processes contribute to the scattering with rotationally excited reagent LiH^+ at the ultracold temperature conditions and the dynamics no longer remains elastic as found in figure 6.4 for $J = 0$. While the depletion probability decreases with increasing rotational excitation the inelastic probability increases. With reagent rotational excitation the availability of lower rotational levels mainly causes the increment of inelastic scattering probability. The decrease in depletion probability with reagent rotational excitation is a combined effect of reagent orientation effect and competition between inelastic and reactive scattering. It is notworthy that both s-wave and non-s-wave scattering contributes to the dynamics for $j = J$ and $j > 0$. For example for $j = J = 1$ the results include contribution from $l =$

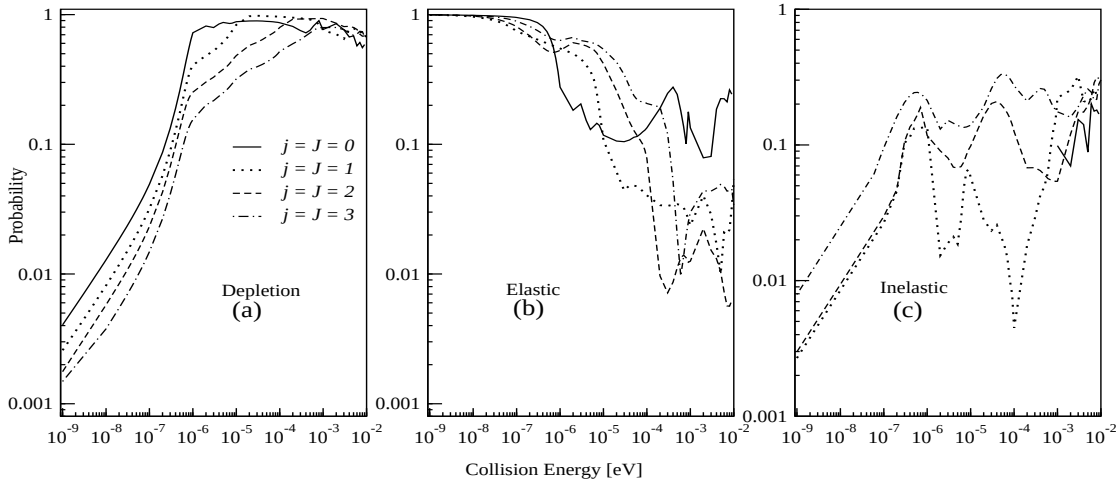

Figure 6.5: Same as figure 6.4 for s-wave scattering $j = J$.

0, 1 and 2.

The s-wave scattering cross sections calculated by using Eqs. 2.47(a-c) are shown as a function of collision energy in figure 6.6(a). The $LiH^+(v = 0, j = 0)$ depletion cross section is shown by the solid line. The elastic and inelastic components of the LiH^+ retention cross sections are shown by the dashed and dotted lines, respectively. It can be seen from figure 6.6(a) that the Wigner limit [88] is reached at the ultracold temperature conditions below $\sim 10^{-8}$ eV. The elastic component of LiH^+ retention cross section exhibits the expected behaviour, *viz.*, $\sigma_{el}^{J=0} \propto E^0$, in the limit of vanishing collision energy. In the latter energy limit, $\sigma_{re}^{J=0} \propto E^{-\frac{1}{2}}$, and the slope of the LiH^+ depletion cross section curve is $\sim$ -0.50 Å^2/eV.

The energy dependent rate constants (for $J = 0$) are plotted in figure 6.6(b). As in figure 6.6(a), the LiH^+ depletion, elastic and inelastic rates are shown by

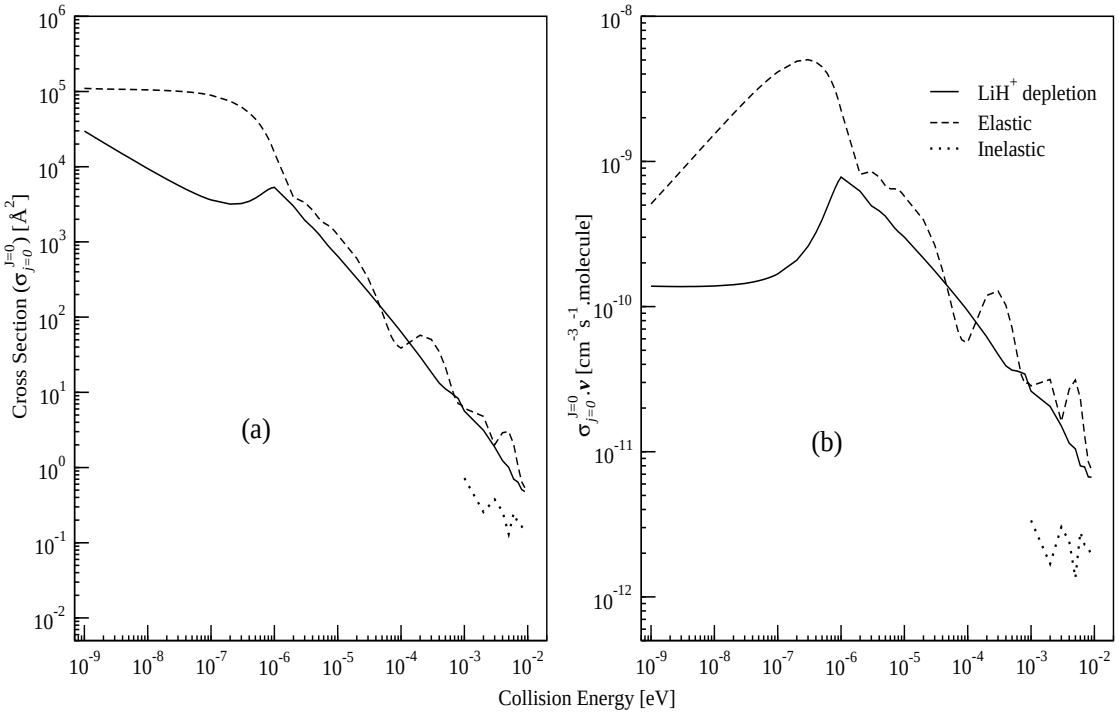

Figure 6.6: The initial state-selected elastic, inelastic and LiH^+ depletion cross sections (panel a) and rate constant (panel b) for the $H + LiH^+$ ($v = 0$, $j = 0$) collisions for the total angular momentum $J = 0$ plotted as a function of collision energy. Both the elastic and depletion processes are found to follow the Wigner law [88] below $\sim 10^{-8}$ eV collision energy.

solid, dashed and dotted lines, respectively, in figure 6.6(b). The rate constants can also be seen to exhibit the Wigner behaviour *viz.*, $\sigma_{el}^{J=0}.v \propto E^{\frac{1}{2}}$ and $\sigma_{re}^{J=0}.v \propto E^0$ in the limit of vanishing collision energy. The rate of the inelastic processes is negligible in this energy range.

The real part of the scattering length is found to be positive and has a large value. A value of $\alpha = 91.69$ Å and $\beta = 11.21$ Å is obtained in the Wigner regime. A large positive value of α may be an indication of the existence of a bound or a quasi-bound state close to a channel threshold.

The LiH^+ ($v = 0$, $j = 0$) depletion probability calculated for $J \neq 0$ is plotted in panel a of figure 6.7 for some selected values of J indicated in the panel. It can be seen from this figure that the J-dependence of the probability is similar to the ones shown in panel a of figure 6.4. In contrast to the latter, the threshold of the probability curves of figure 6.7(a) shifts more rapidly to the higher collision energy because of an increase of the height of the centrifugal barrier with increasing J. This finding is consistent with the variation of reactive and inelastic probabilities shown in figure 6.4. The probability curves of figure 6.7(a) reveal that contribution of partial wave components of $J > 2$ is insignificant to the collision dynamics at ultracold temperatures. In fact it can be seen that for collision energy as low as $\sim 10^{-8}$ eV, it becomes purely s-wave scattering.

As stated before within the studied collision energy range partial wave contribution for J upto 18 is found to be important. The corresponding depletion probabilities are calculated and the integral cross sections are obtained with the aid of Eq. 2.53. These results are plotted in panel b of figure 6.7. The slope of this cross section curve is $\sim$ -0.5 $Å^2$/eV in this limit of lowest collision energy is

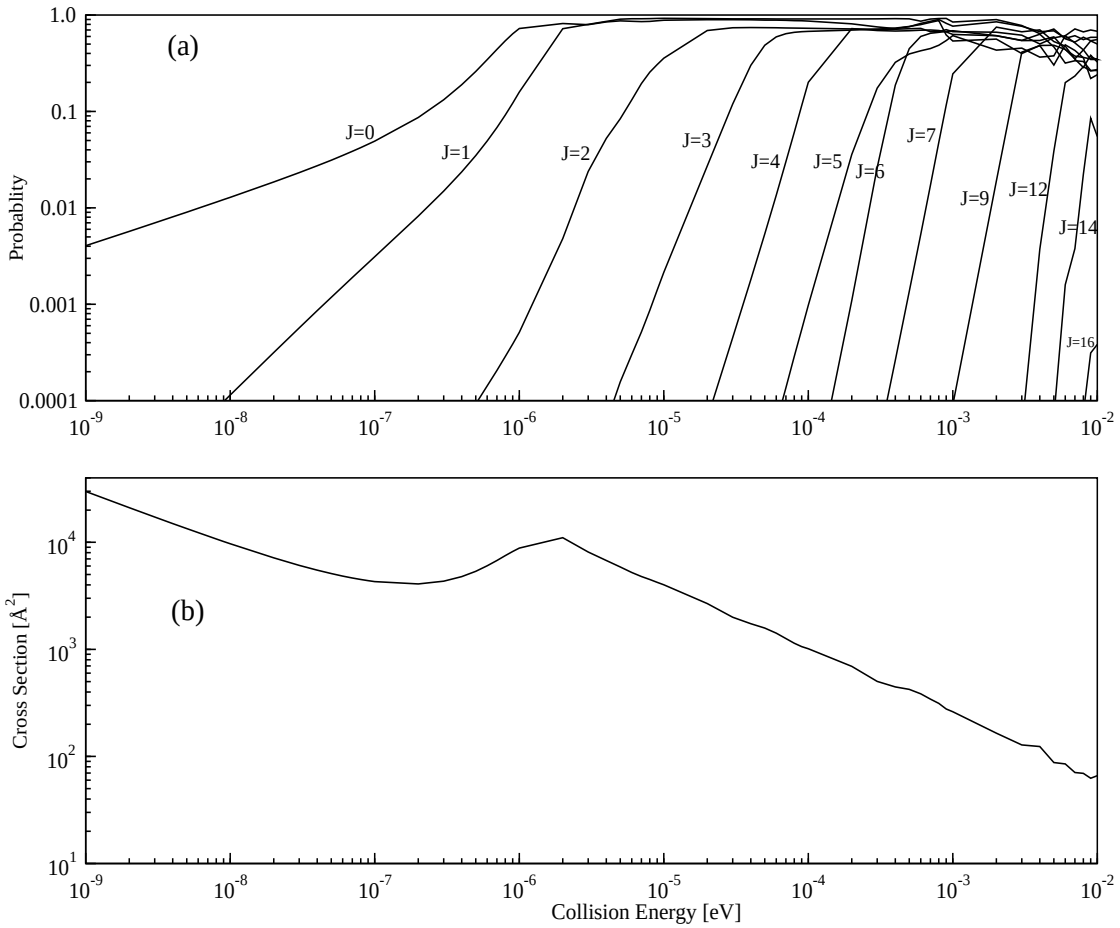

Figure 6.7: Probability (panel a) of H + LiH^+(v =0, j=0) → Li^+ + H_2 reactive processes as a function of collision energy for different values of the total angular momentum J (indicated in the panel). The LiH^+ depletion cross section through the reactive processes mentioned above calculated including the contribution from partial waves for J upto 18 is shown in panel b as a function of collision energy. Both the abscissa and ordinate of the plot are in logarithmic scale.

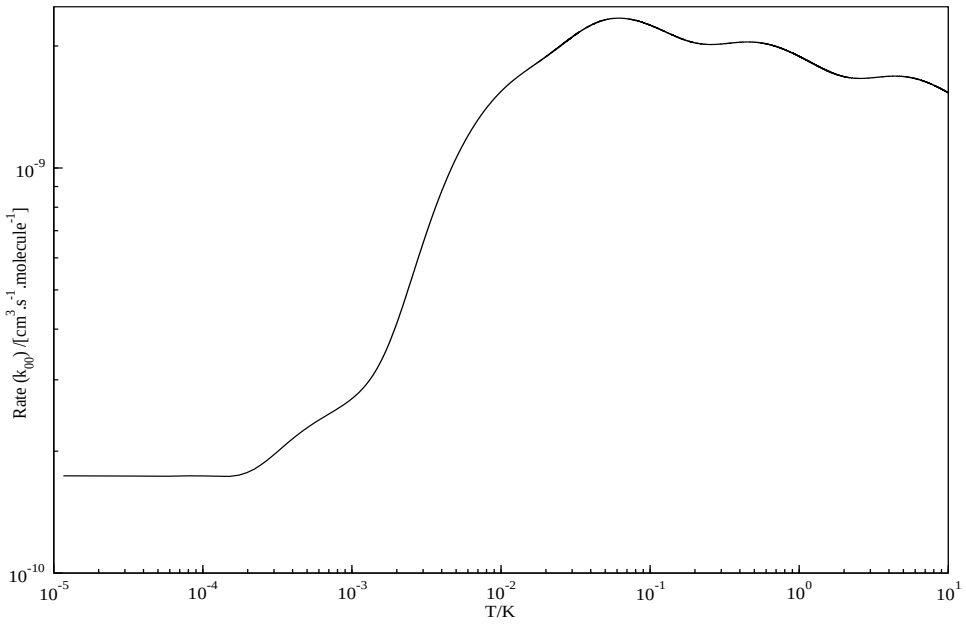

Figure 6.8: Temperature dependent rate constant for the H + LiH^+ (v =0, j=0) → Li^+ + H_2 reaction plotted in a logarithmic scale. The rate is found to have a constant value of ∼ 1.74 × 10^{-10} $cm^3s^{-1}molecule^{-1}$ below ∼ 10^{-4} K.

in accord with the Wigner behaviour illustrated above.

Using the cross section data presented above, the initial state-selected ($v = 0$, $j = 0$) rate constant of the reactive processes is calculated within the temperature range 10^{-5} K to 10 K with the aid of Eq. 2.54. The results are plotted in figure 6.8 in the logarithmic scale. It can be seen that the LiH^+ depletion rate constant attains a nearly constant value of $\sim 1.7376 \times 10^{-10}$ $cm^3.s^{-1}.molecule^{-1}$ below the temperature of $\sim 10^{-4}$ K.

6.3 Summary and outlook

Dynamics of H + LiH^+ collisions is studied at the cold and ultracold temperature conditions by a time-independent quantum mechanical method. The collision dynamics is examined for collision energy as low as $\sim 10^{-9}$ eV. The dynamics of this system is proposed to have intimate connection with the Li chemistry of early universe model. At ultracold temperature conditions LiH^+ depletion and elastic scattering mainly contributes to the collisional outcome. The probability, integral cross section and energy dependent rate of product formation *via.* elastic, inelastic and reactive (LiH^+ depletion) processes are reported for *s*-wave scattering ($J = 0$). The initial state-selected reaction cross sections and thermal rate constants are also calculated for the reactive LiH^+ depletion path by including the partial wave contribution for total angular momentum upto $J = 18$. The major findings of this paper are the following.

1. The elastic scattering dominates over the reactive scattering at ultracold temperature conditions. This means that the probability of LiH^+ retention is more than LiH^+ depletion at this temperature condition which is in

contrast to the result obtained at cold and thermal conditions of temperature. A similar conclusion was drawn by Bovino *et al.* [16] by examining the system at low (10^{-4} eV) collision energy.

2. The reactive LiH^+ ($v = 0$, $j = 0$) depletion dynamics leads to the formation of vibrationally and rotationally excited product H_2. Vibrational and rotational excitations as large as $v' = 12$ and $j' = 30$, are found at the lowest collision energy of 10^{-9} eV considered in this study.

3. Rotational excitation of the reagent decreases the depletion probability. Inelastic process increases slowly for the H + LiH^+($v = 0$, j) collisions at ultracold temperature conditions with rotational excitation of the reagent for $J = j$ case. But for $J = 0$, it quenches.

4. It is found that the higher J values (> 2) do not contribute to the reaction cross section and thermal rate constant at very low collision energy for H + LiH^+($v = 0$, $j = 0$) collision. This finding reconfirms that the s-wave scattering is the only mechanism that governs the H + LiH^+ collision dynamics at the ultracold temperature conditions.

Chapter 7

Summary and outlook

The theoretical study of the collisional dynamics of LiH and LiH^+ with H at thermal and ultracold conditions is presented in this thesis. The dynamical calculations are performed using *ab initio* state-of-the-art PESs developed by Martinazzo *et al.* [41] and Wernli *et al.* [35] for the H + LiH collision and H + LiH^+ collision, respectively. A grid based time dependent wave packet (TDWP) method is utilised to carry out the dynamics at thermal conditions, whereas, the dynamics studies at ultracold condition are carried out by utilizing the 'ABC : a reactive scattering program' of Skouteris *et al.* [55], which is a time-independent formalism. The major findings of the present work are the followings:

1. The elastic process leading to LiH/LiH^+ retention dominates at ultracold conditions. The depletion processes increases with collision energy and at some higher collision energy, becomes the dominant path. In fact at thermal conditions, the LiH/LiH^+ depletion leading to the formation of H_2 dominates the other channel.

2. The vibrational excitation of the reagent (LiH) increases the reactivity of

LiH depletion channel at ultracold conditions but diminishes the same at thermal condition. At thermal conditions , the vibrational excitation of the reagents reduces the reactivity of the LiH depletion channel but enhances the reactivity of H-exchange channel.

3. Rotational excitation of reagents is found to reduce the reactivity for both H + LiH and H + LiH^+ collisions.

4. At very low collision energy, as low as $\sim 10^{-9}$ eV, the formation of product H_2 molecules through the depletion of LiH/ LiH^+, is found to have a distribution over a large range of vibrational and rotational levels.
   For $v = 0$ and $j = 0$ state of the reactant, vibrational and rotational excitation of the product H_2 as high as $v' = 9$ and $j' = 12$ are found for LiH depletion process whereas $v' = 12$ and $j' = 30$ are found for LiH^+ depletion process.
   The distribution of H_2 at relatively higher ro-vibrational levels for the LiH^+ depletion processes compared to LiH depletion process is attributed to the fact that the exothermicity of the H + $LiH^+ \rightarrow Li^+ + H_2$ processes is very high ($\triangle$ E $\sim$ 4.2 eV) compared to H + LiH $\rightarrow$ Li + H_2 processes ($\triangle$ E $\sim$ 2.8 eV).

5. Both LiH and LiH^+ depleted efficiently by the collision with abundant H.

6. The rates of the depletion channel is much larger than that of the exchange channel. The present reaction rates calculated employing the most accurate PES available on this system elegantly fit to a formula, $k(T) = a(T/300K)^b exp[-T/c]$, for the depletion channel. Considering the high accuracy of the present rate constant data, the above analytical equation is expected to be valuable for important astrophysical applications.

To this point we conclude by saying that the present study points to some interesting topic which may be investigated in the near future.

1. The qualitative idea of dynamical outcome from the nature of underlying PES may be revisited. A detail study is required to have a generalised qualitative prediction about the effect of reagent vibrational and rotational excitations on the dynamics of atom-diatom collisions.

2. Constructions of PES and necessary dynamics calculations may be attempted for a few excited PES of H + LiH and H + LiH^+ collisional systems to have a better and details understanding of the Li chemistry in early universe.

Bibliography

[1] P. J. E. Peebles, *Astrophys. J.* **146**, 542 (1966).

[2] R. V. Wagoner, W.A. Fowler and F. Hoyle, *Astrophys. J.* **148**, 3 (1967).

[3] A. Dalgarno, K. Kirby and P. C. Stancil, *Astrophys. J.* **458**, 397 (1996).

[4] P. C. Stancil and A. Dalgarno, *Astrophys. J.* **479**, 543 (1997).

[5] S. Lepp, P.C. Stancil and A. Dalgarno, *J. Phys. B: At. Mol. Opt. Phys.* **35**, R57 (2002).

[6] E. Bodo, F.A. Gianturco, and R. Martinazzo, *Physics Reports* **384**, 85 (2003).

[7] S. Lepp and J. M. Shull, *Astrophys. J.* **280**, 465 (1984).

[8] V. K. Dubrovich, *Astron. Lett* **19**, 53 (1993).

[9] A. Dalgarno and J. L. Fox, in *Unimolecular and Bimolecular Reaction Dynamics*, edited by C. Y. Ng, T. Baer, and I. Powis (Wiley, Chichester, 1994) p. 1.

[10] M. Signore, G. Vedrenne, P. De Bernardis, V. Dubrovich, P. Elmcrenaz, R. Maoli, S. Masi, and P.E. Tanzilli, *Astrophys. J. Suppl. Ser.* **92**, (1994) 535.

[11] R. Maoli, F. Melchiorri, and D. Tosti, *Astrophys. J.* **425**, 372 (1994).

[12] V. K. Dubrovich, Astron. Astrophys. Trans. **5**, 57 (1994).

[13] V. K. Dubrovich, Astron. Astrophys. **296**, 301 (1995).

[14] P. C. Stancil, S. Lepp, and A. Dalgarno, *Astrophys. J.* **458**, 401 (1996).

[15] E. Bougleux and D. Galli, *Mon. Not. R. Astron. Soc.* **288**, 638 (1997).

[16] S. Bovino, M. Wernli, and F.A. Gianturco, *Astrophys. J.* **699**, 383 (2009).

[17] S. Bovino, T. Stoecklin and F.A. Gianturco, *Astrophys. J.* **708**, 1560 (2010).

[18] S. Bovino, M.Tacconi, F.A. Gianturco, D. Galli, and F. Palla, *Astron. J.* **731**, (2011) 107.

[19] *'Theories of Molecular Reaction Dynamics: The Microscopic Foundation of Chemical Kinetics'* by N. E. Henriksen and F. Y. Hansen (Oxford University Press, 2008).

[20] *'Tutorials in molecular Reaction Dynamics'* Edited by M. Brouard and C. Vallance (Royal Society of Chemistry, 2010).

[21] M. Karplus, R. N. Porter and R. D. Sharma, *J. Chem. Phys.*, **43**, 3259 (1965).

[22] M. H. Anderson, J. R. Ensher, M. R. Matthews, C. E. Wieman, and E. A. Cornell, *Science* **269**, 198 (1995).

[23] K. B. Davis, M. Mewes, M. R. Andrews, N. J. van Druten, D. S. Durfee, D. M. Kurn, and W. Ketterle, *Phys. Rev. Lett.* **75**, 3969 (1995).

[24] C. C. Bradley, C. A. Sackett, J. J. Tollett, and R. G. Hulet, *Phys. Rev. Lett.* **75**, 1687 (1995).

[25] B. DeMarco and D. S. Jin, *Science* **285**, 1703 (1999).

[26] P. F. Weck, N. Balakrishnan, *Inter. Rev. Phys. Chem.* **25**, 283 (2006).

[27] M. Born and E. Oppenheimer, *Ann. Phys.*, 84, 457 (1927).

[28] N. J. Clarke, M. Sironi, M. Raimondi, S. Kumar, F.A. Gianturco, E. Buonomo, and D. L. Cooper, *Chem. Phys.* **233**, 9 (1998).

[29] E. Bodo, F.A. Gianturco, R. Martinazzo, and M. Raimondi, *Eur. Phys. J. D* **15**, 321 (2001).

[30] L. J. Dunne, J. N. Murrell, P. Jemmer, *Chem. Phys. Lett.* **336**, 1 (2001).

[31] F.V. Prudente, J.M.C. Marques, and A.M. Maniero, *Chem. Phys. Lett.* **474**, 18 (2009).

[32] K.H. Kim, Y.S. Lee, T. Ishida, and G. Jeung, *J. Chem. Phys.* **119**, 4689 (2003).

[33] H. Berriche and C. Tlili, *J. Mol. Struct.(THEOCHEM)* **678**, 11 (2004).

[34] H. Berriche, *J. Mol. Struct.(THEOCHEM)* **682**, 89 (2004).

[35] M. Wernli, D. Caruso, E. Bodo, and F.A. Gianturco, *J. Phys. Chem. A* **113**, 1121 (2009).

[36] H. S. Lee, Y. S. Lee, and G. H. Jeung, *J. Phys. Chem. A* **103**, 11080 (1999).

[37] J. J. Chen, Y. M. Hung, D. K. Liu, H. S. Fung, and K. C. Lin, *J. Chem. Phys.* **114**, 9395 (2001).

[38] J. J. Chen and K. C. Lin, *J. Chem. Phys.* **119**, 8785 (2003).

[39] Y. F. Liu, X. H. He, D. H. Shi, and F. J. Sun, *Eur. Phys. J. D* **61**, 349 (2011).

[40] D. J. Searles and E. I. von Nagy-Felsobuki *Phy. Rev. A* **43**, 3365 (1991).

[41] R. Martinazzo, G.F. Tantardini, E. Bodo and F.A. Gianturco, *J. Chem. Phys.* **119**, 11241 (2003).

[42] R. Martinazzo, E. Bodo, F.A. Gianturco and M. Raimondi, *Chem. Phys.* **287**, 335 (2003).

[43] W. P. Kraemer and V. Špikro, *Chem. Phys.* **330**, 190 (2006).

[44] A. J. Page and E. I. von Nagy-Felsobuki, *J. Phys. Chem. A* **111**, 4478 (2007).

[45] E. Bodo, F. A. Gianturco and R. Martinazzo, *Chem. Phys.* **271**, 309 (2001).

[46] E. Bodo, F. A. Gianturco, and R. Martinazzo, *J. Phys. Chem. A* **105**, 10986 (2001).

[47] E. Bodo, F.A. Gianturco, and R. Martinazzo, *J. Phys. Chem. A* **105**, 10994 (2001).

[48] R. Padmanaban and S. Mahapatra, *J. Chem. Phys.* **117**, 6469 (2002).

[49] R. Padmanaban and S. Mahapatra, *J. Chem. Phys.* **121**, 7681 (2004); ibid. **122**, 029902 (2005).

[50] R. Padmanaban and S. Mahapatra, *J. Chem. Phys.* **120**, 1746 (2004).

[51] R. Padmanaban and S. Mahapatra, *J. Phys. Chem. A* **110**, 6039 (2006).

[52] R. Padmanaban and S. Mahapatra, *J. Theor. Comput. Chem.* **5**, 871 (2006).

[53] P. Defazio, C. Petrongolo, P. Gamallo and M. González, *J. Chem. Phys.* **122**, 214303 (2005).

[54] I. Pino, R. Martinazzo and G.F. Tantardini, *Phys. Chem. Chem. Phys.* **10**, 5545 (2008).

[55] D. Skouteris, J.F. Castillo and D.E. Manolopoulos, *Comp. Phys. Com.* **133**, 128 (2000).

[56] L. M. Delves, *Nucl. Phys.* **9**, 391 (1959).

[57] L. M. Delves, *Nucl. Phys.* **20**, 275 (1960).

[58] R. T. Pack and G. A. Parker, *J. Chem. Phys.* **87**, 3888 (1987).

[59] R. T. Pack, *J. Chem. Phys.* **60**, 633 (1974).

[60] P. Mcgurie and D. J. Kouri, *J. Chem. Phys.* **60**, 2488 (1974).

[61] R. Kosloff, *J. Phys. Chem.* **92**, 2087 (1988).

[62] R. Kosloff, *Ann. Rev. Phys. Chem.* **45**, 145 (1994).

[63] G. G. Balint-Kurti, F. Göğtas, S. P. Mort, A. R. Offer, A. Laganá, and O. Garvasi, *J. Chem. Phys.* **99**, 9567 (1993).

[64] D.T. Colbert and W. H Miller, *J. Chem. Phys.* **96**, 1982 (1992).

[65] M. D. Feit, J. A. Fleck Jr., and A. Steiger, *J. Comput. Phys.* **47**, 412 (1982).

[66] M.D. Feit, J.A. Fleck Jr., *J. Chem. Phys.* **78**, 301 (1983).

[67] M.D. Feit, J.A. Fleck Jr., *J. Chem. Phys.* **80**, 2578 (1984).

[68] A. Askar and A. S. Cakmak, *J. Chem. Phys.* **68**, 2794 (1978).

[69] D. Kosloff and R. Kosloff, *Comput. Phys. Commun.* **30**, 333 (1983).

[70] H. Tal-Ezer and R. Kosloff, *J. Chem. Phys.* **81**, 3967 (1984).

[71] T. J. Park and J. C. Light, *J. Chem. Phys.* **85**, 5870 (1986).

[72] D. Kosloff and R. Kosloff, *J. Comput. Phys* **52**, 35 (1983).

[73] S. Mahapatra and N Sathyamurthy, *J. Chem. Soc. Faraday Trans.* **93**, 773 (1997).

[74] J.W. Cooley, J.W. Tuckey, *Math. Computation* 19 (1965) 297.

[75] Z. Bačić and J. C. Light, *Ann. Rev. Phys. Chem.* **40**, 469 (1989).

[76] G. C. Corey and D. Lemoine, *J. Chem. Phys.* **97**, 4115 (1992).

[77] *The Theory of Atomic Spectra* by E. U. Condon and G. H. Shortley (Cambridge University Press, Cambridge, 1935).

[78] D. Neuhauser, M. Baer, R. S. Judson, and D. J. Kouri, *Comput. Phys. Commun.* **63**, 460 (1991).

[79] W. H. Miller, *J. Chem. Phys.* **102**, 793 (1998).

[80] N. Balakrishnan, C. Kalyanaraman, and N. Sathyamurthy, *Phys. Rep.* **280**, 79 (1997).

[81] G.A. Parker and R.T. Pack, *J. Chem. Phys.* **98**, 6883 (1993).

[82] G. C. Schatz, *Chem. Phys. Lett.* **150**, 92 (1988).

[83] F. T. Smith, *J. Chem. Phys.* **31**, 1352 (1959).

[84] F. T. Smith, *Phys. Rev.* **120**, 1058 (1960).

[85] D. E. Manolopoulos, *J. Chem. Phys.* **85**, 6425 (1986).

[86] B. R. Johnson, *J. Comput. Phys.* **13**,445 (1973).

[87] F. Mrugala and D. Secrest, *J. Chern. Phys.* **78**, 5954 (1983).

[88] E.P.Wigner, *Phy. Rev.* **73**, 1002 (1948).

[89] N. Balakrishnan, V. Kharchenko, R. C. Forrey, A. Dalgarno, *Chem. Phys. Lett.* **280**, 5 (1997).

[90] J. Z. H. Zhang, *Theory and Application of Quantum Molecular Dynamics*, (World Scientifc, Singapore, 1999).

[91] J. Z. H. Zhang and W. H. Miller, *J. Chem. Phys.* **91**, 1528 (1989).

[92] F. J. Aoiz, L. Bañares, and J. F. Castillo, *J. Chem. Phys.* **111**, 4013 (1999).

[93] D. H. Zhang and J. Z. H. Zhang, *J. Chem. Phys.* **110**, 7622 (1999).

[94] P. Pechukas, J. C. Light, and C. Rankin, *J. Chem. Phys.* **44**, 794 (1966).

[95] N. Sathyamurthy, *Chem. Rev.* **83**, 601 (1983).

[96] J.C. Polanyi, *Acc. Chem. Res.* **5**, 161 (1972).

[97] J. Hirschfelder, H. Eyring, and B. Topley, *J. Chem. Phys.* **4**, 170 (1936).

[98] R.J. Li, K.L. Han, F.E. Li, R.C. Lu, G.Z. He, and N.Q. Lou, *Chem. Phys. Lett.* **220**, 281 (1994).

[99] R. V. Krems *Phys. Chem. Chem. Phys.* **10**, 4079 (2008).

[100] L. D. Carr, D. DeMille, R. V. Krems, J. Ye, *New. J. Phys.* **11**, 055049 (2009).

[101] *Cold Molecules: Theory, Experiment, Applications*, edited by R. Krems, W.C.Stwalley, B. Friedrich (CRC Press, Boca Raton, 2009).

[102] R. C. Forrey, N. Balakrishnan, A. Dalgarno, M. Haggerty and E. J. Heller, *Phys. Rev. Lett.* **82**, 2657 (1999).

[103] G. Quéméner, N. Balakrishnan, R. V. Krems, *Phys. Rev. A* **77**, 30704(R) (2008).

[104] G. Quéméner and N. Balakrishnan, *J. Chem. Phys.* **130**, 114303 (2009).

[105] N. Balakrishnan, G. Quéméner, R. C. Forrey, R. J. Hinde and P. C. Stancil, *J. Chem. Phys.* **134**, 014301 (2011).

[106] S. Fonseca dos Santos, N. Balakrishnan, S. Lepp, G. Quéméner, R. C. Forrey, R. J. Hinde and P. C. Stancil, *J. Chem. Phys.* **134**, 214303 (2011).

[107] N. Balakrishnan and A. Dalgarno, *Chem. Phys. Lett* **341**, 652 (2001).

[108] N. Balakrishnan, *J. Chem. Phys.* **121**, 5563 (2004).

[109] J.C.Juanes-Marcos, G. Quéméner, B.K. Kendrick, N. Balakrishnan *Phys. Chem. Chem. Phys.* **13**, 19067 (2011).

[110] R.A Sultanov, N. Balakrishnan, *J. Phys. Chem. A* **108**, 8759 (2004).

[111] P.F Weck, N. Balakrishnan, *J. Chem. Phys.* **122**, 154309 (2005).

[112] G. Quéméner, N. Balakrishnan, B. K. Kendrick, *J. Chem. Phys.* **129**, 224309 (2008).

[113] G. Quéméner, N. Balakrishnan, B. K. Kendrick, *Phy. Rev. A* **79**, 022703 (2009).

[114] B. Yang, R.C.Forrey, P.C. Stancil, N. Balakrishnan, *Phy. Rev. A.* **82**, 52711 (2010).

[115] W.H.al-Qady, R.C.Forrey, B.H.Yang, P.C.Stancil, N. Balakrishnan, *Phy. Rev. A* **84**, 054701 (2011).

[116] N. Balakrishnan, *J. Chem. Sci.* **124**, 311 (2011).

[117] G. B. Pradhan, N. Balakrishnan and B. K. Kendrick, *J. Chem. Phys.* **138**, 164310 (2013).

[118] E. Bodo, F. A. Gianturco, A. Dalgarno, *J. Chem. Phys.* **116**, 9222 (2002).

[119] E. Bodo, E. Scifoni, F. Sebastianelli, F. A. Gianturco, A. Dalgarno, *Phy. Rev. Lett.* **89**, 283201 (2002).

[120] R. V. Krems, *Int. Rev. Phys. Chem.*, **24**, 99 (2005).

[121] R. V. Krems, *Phys. Chem. Chem. Phys.* **10**, 4079 (2008).

[122] G. Quéméner, P. Honvault, J-M Launay, P. Soldán, D.E. Potter, J. M. Hutson, *Phy. Rev. A* **71**, 032722 (2005).

[123] M.T.Cvitaš, P. Soldán, J. M. Hutson, P. Honvault, J-M Launay, *J. Chem. Phys.* **127**, 074302 (2007).

[124] G. Quéméner, J-M Launay, P. Honvault, *Phy. Rev. A* **75**, 050701(R) (2007).

[125] M.T.Cvitaš, P. Soldán, J. M. Hutson, P. Honvault and J-M Launay, *Phys. Rev. Lett.* **94**, 200402 (2005).

[126] P. Soldán, M.T.Cvitaš, J. M. Hutson, P. Honvault and J-M Launay, *Phys. Rev. Lett.* **89**, 153201 (2002).

[127] M.T.Cvitaš, P. Soldán, J. M. Hutson, P. Honvault and J-M Launay, *Phys. Rev. Lett.* **94**, 033201 (2005).

[128] J. M. Hutson and P. Soldán, *Int. Rev. Phys. Chem.* **26**, 1 (2007).

Publications:

1. **Tanmoy Roy**, T. Rajagopala Rao and S. Mahapatra,"*Quantum dynamics of H + LiH^+ reaction on its electronic ground state*". *Chem. Phys. Lett.*, **501**, 252-256 (2011).

2. **Tanmoy Roy** and S. Mahapatra,"*Quantum dynamics of H + LiH reaction and its isotopic variants*". *J. Chem. Phys.*, **136**, 174313 (1-12) (2012).

3. **Tanmoy Roy** and S. Mahapatra, "*H + LiH^+ collision dynamics at ultracold temperature conditions*". *Chem. Phys.*, **448**, 34-42 (2015).

4. **Tanmoy Roy** and S. Mahapatra, "*Dynamics of H + LiH collision at ultracold temperature conditions*". (Manuscript under preparation).

Poster presented in Conferences and Symposia:

1. Presented Poster in "*Theoretical Chemistry Symposium- 2010 (TCS-2010)*", 9^{th} -12^{th} December, 2010, IIT Kanpur, Kanpur, India.

2. Presented Poster in "*International Conference On Applied Theory On Molecular Systems (ATOMS 2011)*", 2^{nd} -5^{th} November, 2011, Indian Institute of Chemical Technology (IICT), Hyderabad, India.

3. Presented Poster in "*International Symposium on Chemistry and Complexity*", 6^{th} -8^{th} December, 2011, Indian Association for the Cultivation of Science, Jadavpur, Kolkata, India.

4. Presented Poster in "*Theoretical Chemistry Symposium- 2012 (TCS-2012)*", 19^{th} -22^{nd} December, 2012, IIT Guwahati, Guwahati, India.

5. Presented Poster in "*An International Conference On Electronic Structure and Dynamics of Molecules and Clusters*", 17^{th} -20^{th} February, 2013, Indian Association for the Cultivation of Science, Jadavpur, Kolkata, India.

6. Poster presented in '*Chemfest- 2010*', '*Chemfest- 2011*' and '*Chemfest-2012*', an in-house symposium held at School of Chemistry, University of Hyderabad, India.

7. Given oral presentation in "*Chemfest 2014*", an in-house symposium held at School of Chemistry, University of Hyderabad, India.